

Copyright
By
Leah Salathe Worrel
2005

**The Dissertation Committee for Leah Salathe Worrel certifies that this is the
approved version of the following dissertation:**

**Modification of Track-etched Membrane Structure and Performance
via Uniaxial Stretching**

Committee:

Douglas R. Lloyd, Supervisor

Eric Becker

Benny Freeman

Desmond Lawler

Kenneth Liechti

**Modification of Track-etched Membrane Structure and Performance
via Uniaxial Stretching**

by

Leah Salathe Worrel, B.S.

Dissertation

Presented to the Faculty of the Graduate School of
The University of Texas at Austin

In Partial Fulfillment
of the Requirements
for the Degree of

Doctor of Philosophy

The University of Texas at Austin

December 2005

Dedication

To my family and friends, who have given love, support, and patience.

Acknowledgements

I would like to thank my advisor, Dr. Douglas Lloyd, and the members of the Membrane Group, Dr. Desmond Lawler and Dr. Benny Freeman, for their guidance throughout this project. I would also like to thank the other members of the committee, Dr. Eric Becker and Dr. Kenneth Liechti, for their help and encouragement. Thanks go as well to Leah Shimko for her experimental work in permeate characterization and assistance with permeation experiments. I also want to thank Jason Morehouse for his help with the stretching equipment as well as many discussions regarding this research. I am very grateful to all the sources of financial support that contributed to this research and my graduate education: National Water Research Institute, American Water Works Association Research Foundation, Office of Naval Research, and the UT College of Engineering. I would like to thank Dr. John O'Haver and Dr. Ellen Lackey, along with other faculty, at the University of Mississippi for their help and encouragement. Finally, I would like to thank my parents and my friends for their never ending support and faith in me.

Modification of Track-etched Membrane Structure and Performance via Uniaxial Stretching

Publication No. _____

Leah Salathe Worrel, Ph.D.

The University of Texas at Austin, 2005

Supervisor: Douglas R. Lloyd

The objective of this research is to demonstrate changes in performance characteristics of track-etched microfiltration (MF) membranes by uniaxial stretching, and to predict changes in the characteristics of pore entrances, such as major and minor axis, aspect ratio, and pore area, from known membrane properties and stretching conditions. Pore size characteristics (distribution of lengths of the major and minor axes and aspect ratio) impact membrane performance (flux, rejection, and permeate particle size distribution).

Polyester (PET) track-etched (TE) membranes (Whatman) with uniform pores sizes ranging from 0.2 to 10 μm have been stretched at $80\text{C} < T < 170\text{C}$ with total strains up to 40 %. Surface pore characteristics were measured using SEM photos and digital image analysis. For the PET 1 μm membrane, an 11 % stretch increased pore area 31 %, increased the major axis 55 %, decreased the minor axis 14 %, and thereby increased the aspect ratio 78 %. Aspect ratios (ratio of major axis length to minor axis length) increased up to 100 %.

Pure water flux was shown to improve upon stretching for some samples, but almost all samples exhibited improvement in flux with particle challenge. For the 1 μm membrane, resistance was shown to increase upon stretching through a Hermia analysis, and flux increased by 100 % after 1 m^3/m^2 of normalized cumulative volume throughout.

Particle rejection was shown to increase in some cases and stay the same or decrease in others.

The mathematical model relating final membrane structure (deformation) to initial membrane characteristics and stretching conditions uses a constitutive model for membrane material that accounts for non-linear behavior under stress. The material properties are described mathematically by the experimentally determined Prony series, used to predict effects of stretching on pore size and shape. Additionally, uniaxial stress-strain data are used to fit a hyperelastic model, like the Marlow or Arruda-Boyce. The model proved to be useful in predicting pore size and shape based on material properties and stretching conditions, especially for samples of mid-range porosity, or approximately 6 %. The model did not, however, predict the permanent nature of the deformation successfully, allowing the sample to rebound in the simulation significantly more than is observed experimentally.

TABLE OF CONTENTS

LIST OF TABLES.....	xi
LIST OF FIGURES.....	xii
CHAPTER 1: INTRODUCTION AND PREVIOUS WORK.....	1
1.1 HYPOTHESIS AND OBJECTIVE OF THIS RESEARCH.....	1
1.2 TRACK-ETCHED MEMBRANES: MANUFACTURE, PROPERTIES, USES....	4
1.3 PRIOR EXPERIMENTAL WORK ON MEMBRANE STRETCHING.....	7
1.4 PREVIOUS WORK ON MODELING OF MEMBRANE STRETCHING.....	9
1.5 SIGNIFICANCE OF THE RESEARCH REPORTED HERE.....	12
1.6 OUTLINE OF THIS DISSERTATION.....	13
CHAPTER 2: MATERIALS AND METHODS	14
2.1 MEMBRANES.....	14
2.2 MEMBRANE MATERIALS CHARACTERIZATION.....	14
2.2.1 Statistical Analysis of the Surface Pore Characteristics	16
2.3 STRETCHING EXPERIMENTS.....	17
2.3.1 Stretching Equipment.....	17
2.3.2 Sample Preparation	19
2.3.3 Experimental Procedure.....	19
2.4 PERMEATION STUDIES.....	20
2.4.1 Permeation Equipment.....	20
2.4.2 Membrane Sample Preparation.....	21
2.4.3 Particulate Challenge Sample Preparation.....	21
2.4.4 Pure Water and Particulate Challenge Experiments	23
2.5 SUSPENSION AND SOLUTION CHARACTERIZATION.....	24
2.5.1 Turbidimeter	24
2.5.2 Coulter Counter.....	24
2.6 MODEL SIMULATIONS.....	26
2.6.1 Choice of Constitutive Model.....	26
2.6.2 Viscoelasticity.....	27
2.6.3 Relaxation Experiments	31
2.6.4 Master Curve Construction	32

2.6.5 Prony Series Construction.....	33
2.6.6 Hyperelasticity	34
2.6.7 ABAQUS Representations.....	36
2.6.8 Constant Strain Rate Experiments	37
2.6.9 Model Simulation.....	37
CHAPTER 3: RESULTS and DISCUSSION.....	40
3.1 PRE-STRETCHED MEMBRANE MATERIALS CHARACTERISTICS.....	40
3.2 STRETCHED MEMBRANE MATERIALS CHARACTERISTICS.....	41
3.2.1 Stretching Experimental Results.....	41
3.2.2 Rebound Study	59
CHAPTER 4: PERMEATION EXPERIMENTAL RESULTS	62
4.1 PERMEATION FLUX RESULTS.....	62
4.1.1 T-E Membranes: Pure Water Results	63
4.1.2 Min-u-sil Particle Challenge Studies	68
4.1.3 Spherical Beads Challenge Studies.....	73
4.2 PERMEATE ANALYSIS AND REJECTION RESULTS.....	75
4.2.1 Min-u-sil Particle Challenge Studies	75
4.2.2 Spherical Particle Challenge Permeate analysis	84
CHAPTER 5: MODELING RESULTS.....	87
5.1 GEOMETRY STUDY.....	87
5.2 MESH REFINEMENT AND ONE-HOLE STUDIES.....	88
5.3 TWO-HOLE STUDIES.....	91
5.4 SINGLE PORE EXPERIMENTAL RESULTS.....	96
5.5 SENSITIVITY OF SIMULATION TO ARBITRARY MATERIAL PROPERTIES.....	98
5.6 OBTAINING MATERIAL PROPERTIES.....	100
5.6.1 Prony Series	100
5.6.2 Hyperelasticity	102
5.7 TWO-DIMENSIONAL SIMULATIONS WITH ACTUAL PROPERTIES.....	104
5.7.1 Sensitivity of Simulation to Hyperelastic Models with Actual Properties	104
5.7.2 Multiple Pore Study	106

5.7.2.1 <i>Determination of number of pores and number of overlapping pores for simulation</i>	106
5.7.2.2 <i>Multiple Hole Simulation Results</i>	107
5.8 REBOUND STUDY.....	113
5.9 THREE-DIMENSIONAL SIMULATIONS WITH ACTUAL PROPERTIES....	117
CHAPTER 6: CONCLUSIONS AND RECCOMENDATIONS.....	118
6.1 CCONCLUSIONS.....	118
6.2 RECOMMENDATIONS.....	118
6.2.1 Stretching Membranes	118
6.2.2 Performance Characterization.....	119
6.2.3 Modeling.....	119
APPENDIX A PRELIMINARY TEMPERATURE EXPERIMENTS.....	122
APPENDIX B DETERMINATION OF ANNEALING TIME.....	123
APPENDIX C SUPPLEMENTAL RELAXATION EXPERIMENTS.....	124
GLOSSARY.....	125
REFERENCES.....	127
VITA.....	133

LIST OF TABLES

Table 3.1: Pore characteristics for non-stretched track-etched membrane.....	41
Table 3.2: Experimental design	42
Table 3.3: Change in pore characteristics.....	54
Table 3.4: Experimental design and results for rebound study.....	60
Table 4.1: Pure water flux calculation.....	67
Table 4.2: Change in number concentration of Min-u-sil 5 particles	81
Table 4.3: Change in number concentration of 2.02 μm spherical particles	86
Table 5.1: Geometry study results for the constant perimeter assumption.....	87
Table 5.2: Mesh refinement results, comparing change in pore characteristics.....	91
Table 5.3: Results of two-hole user defined meshes stretched 40 %.....	94
Table 5.4: Results of CAE generated two-hole meshes stretched 40 %.....	95
Table 5.5: Single pore experimental results.....	97
Table 5.6: Results for hyperelastic sensitivity study	98
Table 5.7: Results for Prony sensitivity study with 200 element user defined mesh.....	99
Table 5.8: Prony series coefficients.....	104
Table 5.9: Results of sensitivity study for hyperelastic model	105
Table 5.10: Multiple hole meshes defined in CAE	106
Table 5.11: Results of stretching the 5-hole mesh.....	107
Table 5.12: Results of stretching the 8-hole mesh	108
Table 5.13: Results of stretching the 19-hole mesh	112
Table 5.14: Rebound results for stretching one-hole meshes 40 %.....	114
Table 5.15: Results for stretching 3-dimensional meshes with actual properties.....	116

LIST OF FIGURES

Figure 1.1: Particle approaching two pores of the same area.....	2
Figure 2.1: Digital image analysis procedure for TE membranes.	16
Figure 2.2: Biaxial stretcher.....	17
Figure 2.3: Clamp assembly for attaching sample to load cell.....	18
Figure 2.4: Permeation module.....	21
Figure 2.5: SEM of Min-u-sil 5.....	22
Figure 2.6: Min-u-sil particle number distribution.....	22
Figure 2.7: Beckman Coulter Counter, with aperture tube shown on right.....	25
Figure 2.8: Mechanical drawing of A) Spring, B) Dashpot, and C) Maxwell element.....	27
Figure 2.9: Voigt-Kelvin element.....	19
Figure 2.10: Generalized Maxwell model.....	30
Figure 2.11: Qualitative master curve.....	31
Figure 2.12: Von Mises stress distribution from ABAQUS.....	39
Figure 3.1: 2 μ m PET membrane shown non-stretched (A) and at 40 % strain (B).....	43
Figure 3.2: Major axis and minor axis versus strain for 2 μ m PET membrane.....	44
Figure 3.3: Stress-strain curve comparison	45
Figure 3.4: Aspect ratio versus strain for 2 μ m PET membrane.....	46
Figure 3.5: Area versus strain for 2 μ m PET membrane.....	47
Figure 3.6: SEM of 10 μ m PET stretched 18 % demonstrating non-elliptical pores.....	47
Figure 3.7: Porosity versus strain for 2 μ m PET membrane.....	48
Figure 3.83: SEM of a cross section of a PET track-etched membrane.....	50
Figure 3.94: Results of thickness study for stretching 2 μ m PET membranes.....	50
Figure 3.10: Maximum attainable strain	52
Figure 3.11: SEM of 0.6 μ m PET membrane shown non-stretched (A) and 29 % stretched (B).....	53
Figure 3.12: Area and aspect ratio shown as a function of strain for PET 0.6 μ m membrane.....	53
Figure 3.13: SEM of 1 μ m PET membrane shown non-stretched (A) and 22 %	

stretched(B).....	55
Figure 3.14: Area and aspect ratio shown as a function of strain for 1 μm PET membrane.	56
Figure 3.15: Area and aspect ratio shown as a function of strain for 3 μm PET membrane.....	57
Figure 3.16: Aspect ratio shown as a function of strain for all membranes	58
Figure 4.1: Effect of strain on permeability: pure water on 0.6 μm PET membrane.....	62
Figure 4.2: Effect of strain on permeability: pure water on 1 μm PET membrane.....	63
Figure 4.3: Effect of strain on permeability: pure water on 2 μm PET membrane.....	64
Figure 4.4: Effect of strain on permeability: pure water on 3 μm PET membrane.....	64
Figure 4.5: Effect of strain on permeability: pure water on 10 μm PET membrane.....	65
Figure 4.6: Effect of strain on permeability: Min-u-sil 5 on 1 μm PET membrane.....	68
Figure 4.7: Hermia analysis for 1 μm PET: Min-u-sil 5 fed at 10 mg/L.....	70
Figure 4.8: Effect of strain on permeability: A) Min-u-sil 5 on 2 μm PET membrane. B) Min-u-sil 5 on 3 μm PET membrane.....	71
Figure 4.9: Effect of strain on permeability: Min-u-sil 30 on 10 μm PET membrane.....	72
Figure 4.10: Effect of strain on permeability: A) 0.652 μm microspheres on 0.6 μm PET membrane. B) 2.02 μm microspheres on 2 μm PET membrane.....	74
Figure 4.11: Surface area distribution of particles in the permeate	76
Figure 4.12: Surface area distribution of particles in the permeate non-stretched 3 μm PET.....	76
Figure 4.13: Surface area distribution of particles in the permeate for stretched and non- stretched 1 μm PET membrane.....	78
Figure 4.14: Turbidity results for 1 μm PET non-stretched and at 12 % strain.....	78
Figure 4.15: Surface area distribution of particles in the permeate for stretched and non- stretched 2 μm PET membrane.....	80
Figure 4.16: Surface area distribution of Min-u-sil 5 particles in the permeate for 3 μm PET membranes non-stretched and at 18 % strain.....	80
Figure 4.17: Turbidity results 3 μm PET membrane, non-stretched and at 18 % strain...	82

Figure 4.18: Turbidity results for 10 μm PET membrane, non-stretched and at 14 and 18 % strain.....	83
Figure 4.19: Turbidity results for 0.6 μm PET membrane.....	85
Figure 5.1: 4, 8, and 16 element user-created meshes with a single pore	89
Figure 5.2: 48, 200, and 720 element user-created meshes	89
Figure 5.3: User-defined 200-element mesh and CAE generate single pore mesh	89
Figure 5.4: Stress distribution from a 40 % simulated stretch	91
Figure 5.5: Two-hole user defined mesh	92
Figure 5.6: Two-hole user defined mesh	92
Figure 5.7: Two-hole CAE defined mesh	93
Figure 5.8: Results of two-hole studies for user-defined meshes stretched 40 %.....	94
Figure 5.9: Two-hole results for CAE generated meshed stretched 40 %.....	96
Figure 5.10: Results for hyperelastic sensitivity study	99
Figure 5.11: Results for Prony sensitivity study	100
Figure 5.12: Relaxation experiments plotted as the master curve.....	101
Figure 5.13: Stress-strain curves for PET dense film at 100 and 160°C.....	103
Figure 5.14: Stress-strain experimental data and the hyperelastic fit	104
Figure 5.15: Sensitivity of pore characteristics to hyperelastic model chosen.....	105
Figure 5.16: Results of stretching the 5-hole mesh with hyperelastic models.....	107
Figure 5.17: Results of stretching the 8-hole mesh with hyperelastic models.....	108
Figure 5.18: Results of stretching the 9-hole mesh with the Marlow hyperelastic model.....	109
Figure 5.19: Area versus strain for the 9-hole simulation and experimental data from the 2 μm PET membrane.....	110
Figure 5.20: Major Axis versus strain for the 9-hole simulation and experimental data from the PET 2 μm membrane.....	110
Figure 5.21: Minor axis versus strain for the 9-hole simulation and experimental data from the PET 2 μm membrane.	111
Figure 5.22: Aspect ratio versus strain for the 9-hole simulation and experimental data from the PET 2 μm membrane.	111

Figure 5.23: Results of stretching the 19-hole mesh with hyperelastic models.....	112
Figure 5.24: Rebound as a function of temperature	114
Figure 5.25: 8 element 3D mesh.....	115
Figure 5.56: 3-dimensional meshes	116
Figure 5.27: Results of stretching 3-dimensional meshes with actual properties.....	117
Figure A1: Temperature for heating plates and membrane as sample heats up inside the stretching apparatus.....	123
Figure C.1: Relaxation of PET Mylar film using various apparatus.....	124

CHAPTER 1: INTRODUCTION AND PREVIOUS WORK

1.1 HYPOTHESIS AND OBJECTIVE OF THIS RESEARCH

Microfiltration (MF) and ultrafiltration (UF) are widely used in water treatment facilities to remove macromolecules, particles, and colloids from water (Ho and Sirkar 1992). A major concern in these applications is the fouling of the membrane (that is, the irreversible blocking of pores by colloidal/particulate matter and by the macromolecules of natural organic matter). Numerous reports have been published on the deleterious effects fouling has on membrane performance (that is, flux and rejection) and the resulting additional cost of system operations (Flemming, Schaule et al. 1993; Flemming, Schaule et al. 1994; Leslie, Schneider et al. 1993; Wiesner and Aptel 1996). The vast majority of these studies have focused on how the chemical and physical attributes of the foulant impact the extent of fouling. Only recently have publications appeared that begin to describe how fouling is impacted by the physical nature of the membrane (Flemming and Schaule 1988; Ridgway and Safarik 1991; Ridgway and Flemming 1996; Hong and Elimelech 1997). Studies concerned with the physical attributes of the membrane correlated surface roughness (Vrijenhoek, Hong et al. 2001) or pore connectivity (Ho and Zydney 1999) to fouling; in the latter, track-etched membranes were compared to other types of membranes. Significant among the recent publications is a paper by Knoell *et al.* (Knoell 1999) for which the following results are relevant to the research presented herein:

1. increased pore *aspect ratio* results in decreased surface attachment of both hydrophilic and hydrophobic bacterial strains, and
2. increased pore *aspect ratio* results in increased membrane flux,

where *aspect ratio* is defined as the ratio *major axis / minor axis*. The nine commercial membranes used in the previous study (Knoell 1999) had *average* aspect ratios ranging from 2 to 3, and each membrane had a spectrum of pores with different sizes and aspect ratios. Most subsequent studies building on the findings of this publication deal with the improvement in biofouling due to factors such as surface chemistry studied in that publication. The authors of one publication sought to improve fouling by changing the

pore size, among other thing (Espinoza-Gomez and Wai 2001), but no one has studied the effect of aspect ratio.

The findings by Knoell *et al.* (Knoell 1999) were serendipitous in that the modest pore aspect ratio of the membranes studied resulted unintentionally from membrane formation procedures. The aspect ratio was not systematically controlled from membrane to membrane and showed a broad distribution within any given membrane. The findings resulted from thorough surface characterization of the membranes and multi-variable statistical analysis. The research reported here expands upon the earlier studies and provides fundamental knowledge that can serve as the basis for the design of microporous membranes of reduced particulate fouling and greater water flux.

To illustrate the impact of aspect ratio on fouling, consider the following argument. The onset of fouling occurs when a feed solution containing particles is introduced to an initially clean microporous membrane. A simplified picture of this event can be described in terms of a membrane with circular pores of diameter d and cross section $\pi d^2/4$. Flux of pure water through the membrane depends on d and the fraction of the membrane surface area comprised of pores. Figure 1 shows a pore of diameter d and the same pore after elongation. If a spherical particle of diameter D approaches a pore in

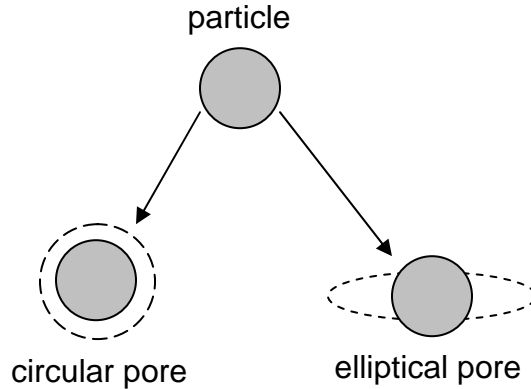


Figure 1.1 Particle approaching two pores of the same area

such a way that the particle center of mass hits the membrane outside the perimeter of the pore, that particle does not influence subsequent transport through the pore. If the center of mass of the particle falls within the perimeter of the circular pore, it can either pass through the pore (if $D < d$) or be rejected by the pore (if $D > d$). If it is rejected, the particle will completely block the entrance to the pore and prevent subsequent liquid transport through that pore. While a particle of diameter $D < d$ passes through the circular pore, it is rejected by the elliptical pore. For the case of D slightly larger than d , the particle that completely blocks the circular pore only partially blocks the elliptical pore, thereby allowing water to continue permeation through a portion of the pore. This simple schematic diagram provides a starting point for further investigation of the second observation by Knoell *et al.* (Knoell 1999).

The *hypothesis* of this research, demonstrated by the above schematic, is that by stretching membranes, and thereby stretching pores, or changing their aspect ratios, membrane performance could be improved. The objective of this research was to study the effects of uniaxial stretching of microporous membranes (and thereby change the aspect ratio) on their performance (measured in terms of flux and particle rejection). This objective was achieved by performing the following tasks:

1. Mathematically simulating the stretching of microporous membranes.
2. Experimentally stretching membranes, measuring initial and final surface pore size characteristics.
3. Comparing the experimental results to the simulation results and adjust/refine simulation procedure accordingly.
4. Developing experimental procedures for characterizing the performance of membranes.
5. Experimentally determining the flux and rejection properties of the un-stretched and stretched membranes.
6. Relating experimentally determined flux and rejection data to pore size characteristics.

1.2 TRACK-ETCHED MEMBRANES: MANUFACTURE, PROPERTIES, USES

The hypothesis presented above and illustrated in Figure 1 is perhaps best demonstrated using track-etched (T-E) membranes because they have pores that traverse the membrane as a cylindrical channel, rather than a tortuous path. As such, T-E membranes perform separations through a surface filtration process (Ho and Zydney 2000). Some of the first T-E membranes were made from muscovite mica, and were created by bombarding the mica with fission fragments from a radioactive substance which damages the sheet, after which channels could be etched out using an acid solution. In these membranes, all channels were rhomboidal in shape, pore size was highly uniform, and all channels were perpendicular to the membrane surface (Quinn 1972). Future work brought about the manufacture of T-E polymer membranes. Two methods have been utilized, one similar to the fission bombardment described above, and the utilizing ion beam accelerators. Both processes include etching with an appropriate acid or base solution, and each has advantages. PET and polycarbonate (PC) membranes are currently produced in this way, but there is still study being done to try to make T-E membranes from other polymers, such as PVDF and polyimides (Apel 2001). To convert the Mylar film to a microporous membrane, the film is irradiated with Xe ion beams, which cut through the film by cleaving polymer chains and creating carboxylic end groups. The pore density of the resulting membrane increases with increasing irradiation dosage (Apel 2001). After irradiation, the film is submerged in an etching bath in which an alkali solution reacts with the broken polymer chains to create cylindrical channels (Apel 2001). The longer the film spends in the etching bath, the larger the pores and the thinner the final membrane (Tsou 2003). In a patented process for PET membrane production, the film is bombarded with Argon or Xenon ions and then treated with dimethyl formamide (DMF) at 70°C for 5 minutes to increase the speed of etching. The film is freed of DMF and treated with sodium hydroxide at a concentration of 5 N at 50°C for an amount of time proportional to the size or pores desired (Lueck 1982).

The T-E membranes used in this study are produced from Mylar films made by Dupont. These films are made from poly(ethylene terephthalate) (PET) and stretched at

an elevated temperature first in the machine direction, then in the transverse direction, and finally cooled in the stretched state. The resulting films are transparent, 23 μm thick, and 25–30 vol-% crystalline as determined by the supplier using differential scanning calorimetry (<http://www.dupontteijinfilms.com>). The Mylar films are then converted to microporous membranes by employing ion beams from accelerators. The resulting membranes are advertised as having circular pore entrances and straight-through cylindrical pores with a rather narrow or uniform pore size distribution (Kesting 1985; Apel 2001); however, as illustrated in Table 1 of the Materials Results chapter, these claims are only approximately true.

One of the unique characteristics of T-E membranes is that both pore size and surface porosity can be closely controlled and are independent of each other; pore size is a function of the length of time in the etching bath and surface porosity is a function of ion or fission fragment bombardment; that is, the number of particles that bombard the film during the irradiation process (Apel 2001). Surface porosity is defined here as the total surface area of the membrane that is porous. The longer the film spends in the etching bath, the larger the pores and the thinner the final membrane. The greater the number of particles used to irradiate the film, the greater the surface porosity.

All of the membranes used in this study were made from PET films, but other types of T-E membranes exist. Others have studied the surface characteristics of polycarbonate (PC) membranes and found that pore density and pore size differ from reported values by 20–40 and 25 to 70 % respectively, but did not comment on any deviation in pore shape from circular (Kim and Stevens 1997). Another study noted the existence of overlapping pores on the surface of PC track-etched membrane, but again did not comment on the aspect ratio of single pores, and did not study membranes with pores that were not perpendicular to the membrane surface (Kim, Stevens et al. 1994). The manufacture of T-E membranes is complex, so it has proven difficult to tailor pore sizes to anything other than the sizes currently available in commercial membranes. To our knowledge, there is no literature related to the stretching of T-E membranes and the impact on membrane performance.

Because of the unique structure of T-E membranes and the manner in which they perform separations, they are widely used for separations in which one needs a clear

distinction between what size of particle passes through the membrane and what is rejected by the membrane (Apel 2001). T-E membranes have been found useful in laboratory filtration applications in which particles are collected on the surface of the membrane and harvested for further analysis (Nash 1990); they are also used for cell culturing (van Hinsbergh, Scheffer et al. 1990). In addition to the applications listed above, T-E membranes are useful for fundamental studies of transport through membranes (Beck and Schultz 1972; Deen 1987; Meares and Page 1972). They have been termed model membranes for biological separations (Pasternak, Adler et al. 1995). T-E membranes can be used in larger scale process filtration, but they have much competition from other types of membranes due to their relatively low surface porosity, low flux, and high cost. Early work was done on T-E membranes with rhomboidal pores made from muscovite mica, showing that estimating these pores by their circular equivalents underestimates their partition coefficient, proving that the presence of rounded corners improves a membrane's ability to partition a solution (Glandt 1981). Glandt also studied the distribution of hard spherical particles inside hard walled pores in the form of flat slits, infinite cylinders, and spherical cavities, showing that even in the cylindrical pore, the particle distribution across the cross sectional area is not even (Glandt 1980).

Much study has been dedicated to understanding the mechanism that causes flux decline (Hermia 1982). To further the understanding of flux decline, and recognizing that generally more than one method is needed to describe flux decline over the course of the experiment, Ho and Zydney created a hybrid of the above mentioned models in order to describe flux decline over the entire experiment without switching models. Their experimental results showed excellent agreement with their new model (Ho and Zydney 2000). These same authors studied the effect of membrane morphology on flux decline, including in their study T-E membranes. They found that for T-E low surface porosity membranes, fouling is an inverse function of surface porosity. At higher porosities, however, fouling becomes independent of surface porosity. This is attributed to the fact that, for higher surface porosity membranes, a single aggregate can block multiple pores (Ho and Zydney 1999). Pore shape was not a factor in this study.

The manufacture of T-E membranes is complex, so it has proven difficult to tailor pore sizes to anything other than the sizes currently available in commercial membranes. This study presents a possible method for tailoring the pore size of T-E membranes, using currently available membranes as a precursor. To our knowledge, there is no extant literature related to the stretching of T-E membranes and the impact on membrane structure and performance

T-E membranes were chosen for their applicability to fundamental studies, but also for their simple surface geometry, which aids in the modeling of the stretching process.

1.3 PRIOR EXPERIMENTAL WORK ON MEMBRANE STRETCHING

As stated above, there is no prior work relating to the stretching of T-E membranes. However, it is important to put this research in proper perspective by reviewing the existing literature on making microporous membranes by stretching dense films as well as the existing literature on stretching microporous membranes.

When one thinks of stretching films in association with membrane formation, one typically thinks of the Celgard® process in which pure polyolefin, such as high-density polyethylene (HDPE), is extruded under high stress to form a *dense film* referred to as a *precursor* (Sarada and Sawyer 1983),(Hoeve and O'Brien 1963; Bierenbaum, Isaacson et al. 1974). This precursor is uniaxially stretched at room temperature, stretched again at an elevated temperature, and finally annealed. These thermal–mechanical steps are used to create pores, increase pore size, raise polymer crystallinity, and improve mechanical strength (Druin, T. et al. 1972; Fisher, Leone et al. 1989). Microporous membranes have also been created by a stretching process from dense films containing polymer blends (Chandavas, Xanthos et al. 2001). In contrast to the Celgard® process done by Celanese, that starts with a dense film, this research focused on the orientation of films that already contain distinct pores.

Most commercially available microporous membranes are made via phase inversion or phase separation processes (PI/PS). PI/PS membranes can either be anisotropic or isotropic in structure (where anisotropic indicates a pore size gradation in

the direction of transport, and isotropic indicates no pore size gradation). PI/PS membranes typically have a cellular structure, thereby presenting a tortuous path through the membrane. They also have a pore size distribution somewhat larger than that found in T-E membranes. The process for making these membranes is well documented in the literature (Lloyd, Kinzer et al. 1990; Lloyd, Kim et al. 1991; Kim and Lloyd 1991; Lim, Kim et al. 1991; Kim, Lim et al. 1991; Alwattari and Lloyd 1991); consequently, no discussion of their formation is presented here other than to say that intentional orientation of the membrane is not typically a part of the membrane formation process. Membrane pore openings tend to be slightly elliptical, with aspect ratios ranging from 1.2 – 1.6 due to the manufacturing process. Our studies characterizing commercial MF and UF membranes indicate that aspect ratios are typically in the range 1 to 2 (Morehouse 2006). For track-etched membranes, aspect ratios are generally around 1.2, as seen in Table 1 of the “Materials Results” chapter.

As the following paragraphs illustrate, some recent work on the intentional stretching of microporous phase separation membranes has been reported in the patent literature.

Researchers at 3M have done considerable work on stretching microporous films. For example, Shipman formed films from polyethylene (PE) in a low molecular weight *diluent* (60 wt- % PE) (Shipman 1985). The films were then oriented in at least one direction after phase separation but prior to diluent extraction and subsequently annealed. Kinzer (Kinzer 1993, 1989) extrapolated Shipman’s work by biaxially orienting cellular PE films. In this case, the films were stretched and heat set after diluent extraction. Diluent extraction and extractant evaporation processes were carried out on restrained films. Mrozinski (Mrozinski 1988, 1989; Mrozinski 1993) added the use of a nucleating agent to the Shipman process. The nucleating agent was used to reduce the size of the polymer particles, increase their number, and promote rapid crystallization of the polymer. The resulting films were uniaxially or bi-axially oriented before or after diluent extraction. Recently, Clinnton (Clinnton 1997) patented the formation of poly(ethylene-*co*-vinyl alcohol) membranes via a process that included film orientation. Clinnton’s work was to the stretching of EVAL hollow fiber membranes by Ebara Corporation (McCray, Friesen et al. 2001). The hollow fiber membranes were made using the TIPS

process and then cold stretched in order to increase the pure water flux through the membrane.

Takita *et al.* (Takita, Kono et al. 1991, 1991) at Tonen Corp. formed films from polyethylene in paraffin oil (20 wt- % PE) and bi-axially stretched and annealed films. Takita *et al.* showed that extraction before stretching (as opposed to after stretching) resulted in films of lower mechanical strength and larger pores. However, they did not offer any explanations for these observations. Jacoby *et al.* (Jacoby, Bauer et al. 1992) at Amoco Corp. formed oriented polymeric films from ethylene-propylene block copolymers. Orientation was achieved by stretching diluent-containing films either uniaxially or bi-axially. None of the patents cited in the preceding two paragraphs report in any detail how the pore size and pore size distribution changed as the result of stretching or how these changes influenced membrane flux and rejection. The patents do suggest that starting with a given precursor film the final porous structure of the membrane is influenced by the conditions of the stretching (wet vs dry; extent of stretching; rate of stretching; stretching temperature; annealing temperature).

There is no existing literature describing the modification of membrane pore dimensions in flat sheet membranes via uniaxial stretching, a process that may significantly alter membrane performance characteristics. Although some studies have noted the existence of aspect ratios greater than one in microfiltration membranes and the benefits of that physical characteristic, no one to date has set out to purposefully alter and measure this physical characteristic in track-etched flat-sheet membranes.

1.4 PREVIOUS WORK ON MODELING OF MEMBRANE STRETCHING

Recent research (Knoell 1999) has shown that there are advantages to changing the aspect ratio of pores. This project is the first step of an in-depth investigation of membrane stretching as a performance enhancer and includes the development of an appropriate simulation model to enable prediction of performance characteristics from known membrane properties and stretching conditions.

Several mathematical models exist for predicting the change in shape of a void in elastic, plastic, elastic-plastic, and linear viscoelastic materials (Eshelby 1957;

Needleman 1972; Gurson 1977; McClintock 1968; Mohan and Brust 2000; Budiansky 1982; Andersson 1977; Wang 1993). Eshelby (Eshelby 1957) determined the elastic field surrounding an inclusion in a perfectly elastic solid, noting the special case of an ellipsoid. The predicted stress fields were valid for points close to or far from the void, but not at intermediate distances. McClintock (McClintock 1968) proposed a criterion for fracture in plastic materials with cylindrical voids in an infinite medium, but he ignored interaction effects between voids. Others (Rice 1969; Tracey 1971) built on his work by extending it to spherical pores and finite mediums. Gurson (Gurson 1977) proposed a model to predict yield during the stretching of a porous ductile material. The model assumes a rigid, perfectly plastic material and considers the spherically symmetric deformations around a single spherical void and a single cylindrical void. Starting with Gurson's constitutive equation and employing a plastic flow law, Tvegaard (Tvegaard 1981) proposed a stress analysis model that allows for the merging of neighboring pores as a result of stretching and the breaking of thin regions between pores. Tvegaard applied his model to plastic materials containing periodically distributed cylindrical (Tvegaard 1981) and spherical pores (Tvegaard 1982). Needleman (Needleman 1972) modeled the two-dimensional uniaxial deformation of an elastic-plastic medium containing a double periodic square array of cylindrical voids under plane-strain conditions. Both the effects of geometrical non-linearities resulting from large deformation and physical non-linearities arising from plastic material behavior were included in formulating the problem. Needleman predicted stress distribution, but did not show the configurational change of pores during the stretching process. He also admitted that his model failed well before coalescence of pores.

All of the above studies apply to elastic, plastic, or elastic-plastic materials. Polymers such as those that comprise membranes do not behave according to any of these models because they exhibit temperature and rate dependence; thus, further work is needed. Hashin (Hashin 1965) studied the behavior of linearly viscoelastic heterogeneous material, employing the correspondence principle. Although his study is not specific to voids, it can be extended to that case, as he mentions. Budiansky *et al.* (Budiansky 1982) studied void growth in viscous solids. Mohan and Brust (Mohan and Brust 2000) extended this study to determine the effects of elasticity on void evolution in

viscous solids, specifically metals that exhibit creep at high temperatures. Polymers exhibit creep behavior, which will be significant in modeling the stretching process, but they exhibit viscoelasticity, which metals do not. Li and Weng (Li 1995) studied the void growth of aligned spheroidal voids in linear viscoelastic materials in 1995. Their model of viscoelasticity is arrived at by LaPlace transform of the Eshelby-Moru-Tanank concept of elasticity. Li and Weng extended their study (Li 1998) to include composite materials in which inclusions are elastic but the matrix is viscoelastic or viscoplastic, but the case of voids is not discussed. Similarly, Wang and Weng (Wang 1993) modeled self-similar void growth in linear viscoelastic material at moderate strains. They showed that the condition of self-similar growth depends on the viscoelastic model used. Clements (Clements 1999) built on the work of Eshelby and Weng by finding an accurate analytical theory for viscoelastic deformation of soft polymers (above the glass transition temperature), which is an improvement on Weng's numerical solution. Clements' work shows that uniaxial deformation of aligned ellipsoidal voids rapidly increases aspect ratio, and more slowly increases void concentration. His work acknowledges the importance of non-linearity at high strains, but does not account for these non-linearities, and does not predict deformation for strains above 80 %. Steenbrink, *et al.* (Steenbrink 1998) studied void growth in a finite element unit cell model for a single sphere or cylinder in a visco-plastic material. Most recently, Smit *et al.* (Smit 2000) sought to stabilize the post yield response of polymers by studying the effects of both voids and inclusions. They found that the presence of both voids and inclusions caused the stress to spread out over the material and was successful in stabilizing the post-yield response. These models demonstrate that under uniaxial tension, circular pores change shape to elliptical; however they do not predict coalescence of pores and can only account for pore interactions in a very simple, approximate way.

The materials to be studied here are polymeric and are therefore viscoelastic in their behavior (McCrum 1997). In order to modify their pore characteristics they will be stretched beyond the linear viscoelasticity region. Linear viscoelasticity is valid for small deformations, usually when the strain is less than 0.5 % (McCrum 1997), and assumes that the shape of the material before deformation can be regained once the material has relaxed. The material behavior can be described by a time-temperature shift curve, or

master curve, constructed by relaxation experiments and the Williams-Landel-Ferry (WLF) equation. Beyond this linear region, material behavior deviates from this master curve. In addition, it is the goal of this project to create both large and small permanent deformations. Therefore, this project will investigate a way to predict nonlinear material response to strain, where strain is defined in Equation 1.1 where L_F is the final sample length and L_O is the initial sample length, and the WLF will still be employed to give the material time dependence, employing a nonlinear elasticity model to account for nonlinear behavior.

$$Strain = \frac{L_F - L_O}{L_O} \quad (1.1)$$

A constitutive viscoplastic model for PET was proposed by Vigny, *et al.* (Vigny 1999) to describe plane-strain stretching of PET films for large strains. This model employs a viscoplastic term, which contains several experimentally determined constants. Finite strain models for elastomers have had success predicting the behavior of rubbers at large deformations (Bergstrom 1998). This result is relevant because polymers behave like viscous elastomers above the glass transition temperature. Wu and Liechti (Wu 2000) studied the results from two different models, a pseudo stress model and a pseudo strain model, and were successful in predicting the stress-strain behavior using the pseudo stress models, including the finite viscoelastic model in the finite element program ABAQUS.

Although several or all of the models discussed above may be appropriate for modeling the behavior of PC and PET membranes, the model this project will employ is the finite strain viscoelastic model, which has already been integrated into the ABAQUS software. The finite strain viscoelastic model in ABAQUS is essentially a pseudo stress model and was shown to be objective¹ (Wu 2000), which is an essential quality for modeling material behavior. ABAQUS has been used in research to model viscoelastic deformations. Sweeney, *et al.* (Sweeney 2001) employed ABAQUS to solve their constitutive model for the large deformation of polyethylene. ABAQUS has proven to be a successful tool for modeling the behavior of rubbers and polymers.

¹ “Objective” is used to identify a constitutive model as being independent on the frame of reference, meaning the answer to the problem does not depend on direction or approach.

Although much had been done in terms of modeling void growth in many types of materials, stretching membranes is a novel process, and no one to date has tried to apply these methods for the purpose of modeling that process, or tried to model the effects of void interaction for the purpose of predicting membrane performance.

1.5 SIGNIFICANCE OF THE RESEARCH REPORTED HERE

This research will provide the water industry and other separations industries, and the membrane manufacturers that supply these industries, with new options for membranes. Stretched membranes should improve substantially the tradeoffs among flux, permeate quality, fouling, and pressure that characterize membrane performance. This research will lead to substantial reductions in capital costs for separations processes by reducing the required membrane area required for a given process. By modeling the stretching process, membrane performance characteristics can be tailored to a specific application without excessive experimentation necessary. Membrane characteristics, and therefore membrane performance, can be predicted based on material properties and stretching parameters, through the model.

1.6 OUTLINE OF THIS DISSERTATION

Chapter 2 of this dissertation outlines the materials and procedures used in stretching and permeation experiments and characterization, as well as a description of the model used for simulations. The subsequent three chapters present results. Chapter three presents results of membrane stretching and characterization by digital image analysis. Chapter 4 presents the results of permeation experiments, pure water flux and particulate challenge, and the characterization of the permeate. Chapter 5 presents the simulation studies, which are compared to experimental results. Finally in Chapter 6, conclusions and recommendations are made.

CHAPTER 2: MATERIALS AND METHODS

2.1 MEMBRANES

Track-Etched (T-E) membranes made from poly(ethylene terephthalate) (PET) were kindly donated by Whatman Corporation in the form of 21.6 cm by 27.9 cm sheets. These membranes were produced from Mylar films made by Dupont. These films are made from PET polymer that is biaxially stretched on rollers in a proprietary process. PET is stretched first in the machine direction, and subsequently in the transverse direction, both at an elevated temperature, and then cooled in their stretched form. The result is a film 23 μm thick that is approximately 25-30% crystalline by volume and transparent (<http://www.dupontteijinfilms.com/datasheets/mylar/overview/h67160.pdf>). Membranes are made from these films in the method described in the previous chapter, resulting in thicknesses varying from 13 μm to 23 μm depending on the pore size. Membrane with pore sizes of 0.2, 0.4, 0.6, 0.8, 1, 2, 3, and 10 μm were obtained. These PET membranes are reported by the manufacturer to be relatively hydrophilic and were found in this research to be usable without any need for pre-wetting. Dense films, Mylar from Dupont, were obtained from Whatman Corporation as 21.6 cm by 27.9 cm sheets 23 μm thick. These films were used to obtain physical material properties needed for modeling.

2.2 MEMBRANE MATERIALS CHARACTERIZATION

Membrane surface characteristics, such as pore area, pore major axis, pore minor axis, and porosity, were studied using a Hitachi S-4500 field emission scanning electron microscope (SEM) and digital image analysis. Two small samples were cut with a razor blade and placed on a stage. The samples were coated with a gold-palladium mixture, and then inserted into the vacuum chamber. A voltage acceleration of 15 kV was used. Five micrographs were taken of the membrane surface at various locations on each sample for a total of ten pictures. All micrographs of a given membrane were taken at the same magnification, which varies depending on membrane pore size and porosity in

order to get approximately 20 pores per micrograph. These micrographs, which were saved as digital files, were then analyzed using digital image analysis. Quantities measured were major axis length, minor axis length, and individual pore area. These values were used to calculate aspect ratio, average pore area, surface porosity (fraction of the surface that is occupied by pores), and pore density (number of pores per unit membrane area). Figure 2.1 shows a micrograph of a typical membrane section. The scale of the picture was input to the program so that it could accurately measure pore size and shape characteristics. The image then underwent thresholding, which caused everything but the pore to disappear from the image. The computer could then count the number of pores and measure the major axis, minor axis, and individual pore area, which are determined by counting the number of pixels that make up a pore. This method is depicted in Figure 2.1. Thickness of each membrane was also measured using the SEM and digital image analysis software.

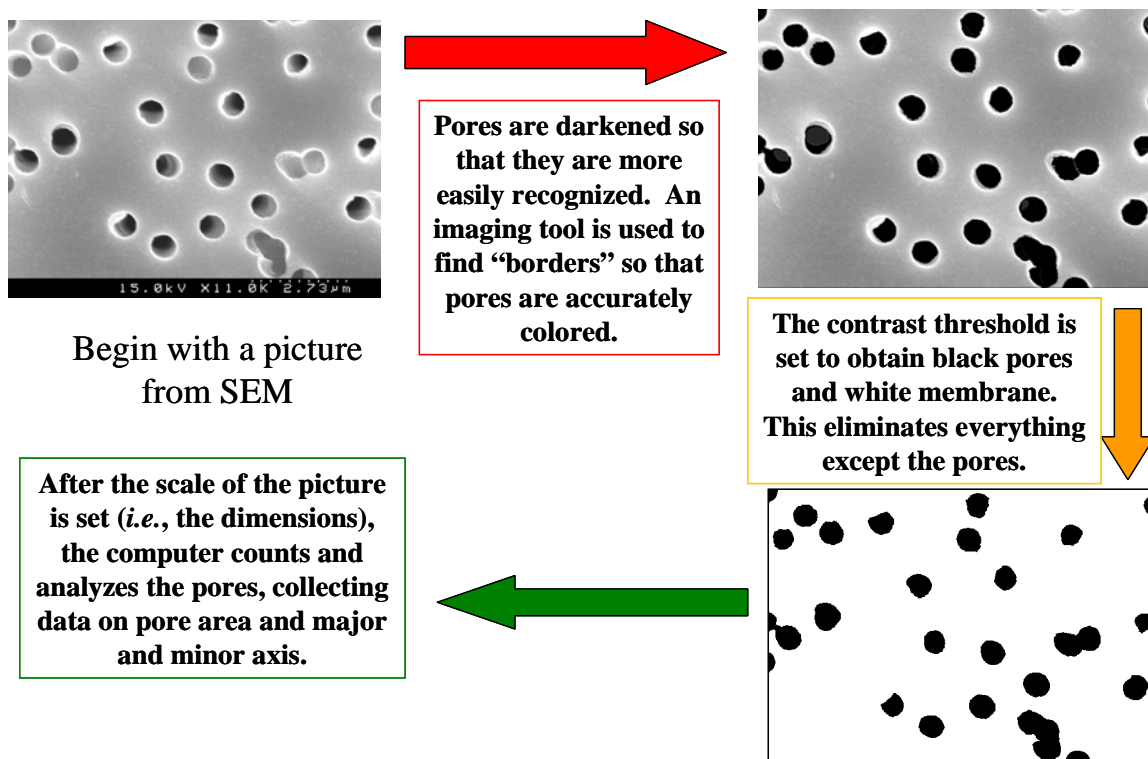


Figure 2.1 Digital image analysis procedure for TE membranes

There was an option to include or ignore pores touching the edge of each picture. These pores, only partially shown, would skew the results for aspect ratio and area, but needed to be taken into account for calculating the porosity of the membrane. Therefore, each picture was evaluated twice, once taking the edge pores into account to calculate the porosity, and once ignoring edge pores to evaluate more accurately area and aspect ratio.

2.2.1 Statistical Analysis of the Surface Pore Characteristics

A statistics program, JMP (<http://www.jmp.com/>), was utilized to determine the error in calculating pore area, major and minor axis, aspect ratio, and porosity. As described above, many pictures were taken of each sample and analyzed using the digital image analysis procedures described above, which results in the reporting of the major

and minor axis and area of every pore. These numbers, along with aspect ratio calculated from the major and minor axis, were entered into the JMP program in groups according to the picture from which each set of data came. JMP compared the data by picture and eliminated any sets that were significantly different from the rest of the group according to a student's t-test (Sall et al. 2001). Once these outliers were eliminated, JMP calculated the mean values of area, major and minor axis, aspect ratio, and porosity, and also reported a 95% confidence interval, which are shown as error bars on results.

2.3 STRETCHING EXPERIMENTS

2.3.1 Stretching Equipment

A biaxial stretcher (www.inventurelabs.com) was donated by 3M Company. A picture of this equipment is shown in Figure 2.2. Upon instillation of the device, some of its controls and components were not fully operational or not up to the desired standard of accuracy. Therefore, the equipment was modified to make it suitable for use on this project. The pneumatic gripping system is original to the machine, as is the pantograph mechanism.



Figure 2.2 Bi-axial stretcher

New heating plates and controls were the first improvements to be installed. The heating plates were custom made by Inventure Labs (www.inventurelabs.com) to fit the existing machine. A computer was obtained, along with a data acquisition card (DAQ

card) and connector block from National Instruments (www.ni.com). Thermocouples, signal conditioners, and solid state relays were obtained from Omgea (www.omega.com), and the required circuitry was completed to connect the heating plates to the computer through the DAQ card. Labview software was used to create a control loop. In this way, controlling the temperature in the box became easier for the user and more accurate. Thermocouples were calibrated using ice water.

A new electric stepper motor was installed to replace the existing hydraulic motor, along with a potentiometer to measure strain and strain rate. (www.inventurelabs.com, www.unimeasure.com) The motor and actuation system was custom made to fit the machine for one axis of motion, and using ASCII code and Labview, this application was also controlled on the computer. The potentiometer required a power source, which was obtained from Omega, and the circuitry was completed so that data from the potentiometer could be read by the computer and displayed by Labview. The potentiometer was calibrated with a ruler accurate to 0.254 cm.



Figure 2.3 Clamp assembly for attaching sample to load cell

Finally, two load cells were obtained, one with a maximum load of 3 kg and one with a maximum load of 30 kg, both from Load Cell Central (www.800loadcel.com). These load cells were calibrated using known weights. A signal conditioner, model OM 10, was also purchased to amplify the signal from the load cell so that it could be read by the DAQ card. Calibration of the load cells was performed on a regular basis. In order to read the force of stretching a sample, a new clamping system had to be devised so that the load cell could remain outside of the heated box, but still detect the force of stretching without interference. A new sample clamp that bypasses the pneumatic gripping system

was made. This clamp holds the sample and a tab extends from the back of this clamp directly to the load cell through a hole in the heated box, as shown in Figure 2.3.

2.3.2 Sample Preparation

A membrane sample to be stretched was cut using a razor blade. The sample length was cut to be approximately 10 cm in width and approximately 11 cm or more in length. Each end of the sample was wrapped around a metal bar to help assure proper alignment and to distribute gripping force evenly over the width of the membrane. The sample was taped to the bar in order to secure its alignment. For experiments requiring force data, one bar was placed in a clamp that could then bypass the machine's gripping system and be connected to the load cell for accurate force measurements. For all other experiments, the sample was placed in the machine with the two bars secured in the gripping mechanisms. The two sides not wrapped around the bars were left unconstrained. Nitrogen gas was used to apply pressure and grip the two ends of the membrane sample. The sample was then pre-tensioned, meaning that the gripping mechanism attached to one end of the sample was moved out just enough to make the sample taut. Movement of the grip was via a motor drive.

2.3.3 Experimental Procedure

The sample was placed in the stretching machine with the two bars secured in the gripping mechanisms. The two sides not wrapped around the bars were left unconstrained. Nitrogen gas was used to apply pressure to the pneumatic grips and the two ends of the membrane sample were secured. The sample was then pre-tensioned by moving the gripping mechanism attached to one end of the sample out just enough to make the sample taut. The top of the box was then closed and the heating plate turned on. After the plates reach the desired temperature, the sample was left in the box for 30 minutes to ensure that the sample has also reached the desired temperature. Preliminary experiments, explained in Appendix A, were performed to determine that 30 minutes was sufficient time to allow the membrane to reach the desired temperature. The appropriate strain rate was chosen, and the distance required to reach the desired strain was calculated. This strain was then applied to the sample. Once the sample reached the desired strain, it was annealed (held at the same degree of strain) at either the same or

higher temperature for 10 to 15 minutes. Preliminary experiments showed that annealing for 10 to 15 minutes at the same or higher temperature was sufficient to maintain a permanent deformation with little rebound (Yoshida et al. 1999; Yukio and Fumiyuki 2001; Jolliffe 1995). The box was then opened and the sample allowed to cool. The sample was then removed and measured with a ruler accurate to 0.125 cm in order to determine the actual strain obtained. All samples were stretched in the machine direction, meaning that all samples were stretched in the direction that the membrane was made. Temperature was varied from 80°C to 170°C, and strain rate was varied from 0.1 to 1 cm/s. Annealing time and temperature were not varied in this study.

The procedure for conducting experiments to study the rebound of membranes was similar to that described above for the stretching process. The temperature, strain rate, and strain were varied, but in this case, annealing temperature was also varied. The annealing temperature was varied between room temperature, 25°C, and the temperature at which stretching was performed, such that there was no cooling before releasing the sample from the clamps in some cases. The length of the sample was measured after being released from the clamps and compared with the amount of strain applied to the sample to determine the amount of rebound.

2.4 PERMEATION STUDIES

2.4.1 Permeation Equipment

One dead-end permeation module was used for permeation experiments, and it is shown in Figure 2.4. The module was an Amicon model supplied by Millipore Corporation. It was a 15 mL cell with a 25 mm membrane diameter, and the cell could not be stirred. The cell was fed from a reservoir with a capacity of 5 L. The reservoir was sealed and pressurized with nitrogen gas. The pressure was controlled by a digital controller (Praxair, Model GC12) with a digital pressure gauge in line.

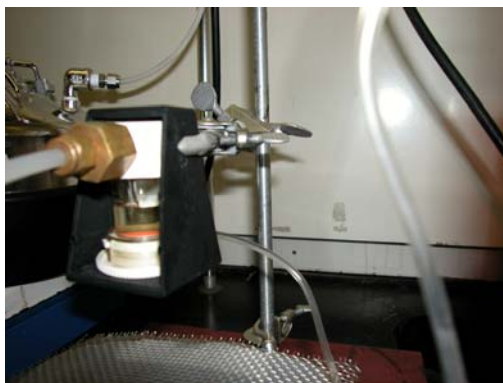


Figure 2.4 Permeation module

2.4.2 Membrane Sample Preparation

PET membrane samples were cut using a circular pattern of the appropriate size, 25 mm diameter, and a razor. The pattern was marked on the membrane with a pen, and then the sample was cut just inside the marking with a razor blade. The membrane sample was placed on the support in the permeation module, and used without the need for pre-wetting.

2.4.3 Particulate Challenge Sample Preparation

Particulate challenge experiments were performed with two types of particles: Min-u-sil and cross-linked polystyrene spheres. The Min-u-sil was obtained from U.S. Silica Company (Berkeley Springs, W.V.; www.u-s-silica.com/mus.htm). Min-u-sil 5 consists of irregularly shaped particles, shown in Figure 2.5, that are 99.2% silicon dioxide. Min-u-sil 5 has a broad particle size distribution with 88% of the measured particles having a diameter between 0.8 and 2.5 μm with a median size of 1.7 μm , as shown in the number distribution in Figure 2.6; the measurements were made using a Coulter Counter, described below. When plotted in this way, the area under the curve between any two values of the log diameter is the total number concentration in that size range. Also shown in the figure is the surface area distribution, obtained by multiplying the number distribution value of each size by the surface area of a sphere (πd_p^2) of that size; the area under this curve is the total surface area concentration. Because the surface area is closely related to the projected area of a particle, the surface area distribution is useful in this research with the circular pore openings on the PET membranes. These

particles were used to test membranes with pore sizes of 1, 2, and 3 μm , as this size distribution presented an appropriate challenge for those membranes. Similarly, Min-u-sil 30 was used to test the 10 μm pore size. Min-u-sil 30 has a particle size distribution with a shape similar to the Min-u-sil 5 described above, but the scale of particle sizes is larger; the manufacturer states that 98% by weight of Min-u-sil 5 and 30 are smaller than 5 and 30 μm in diameter, respectively.

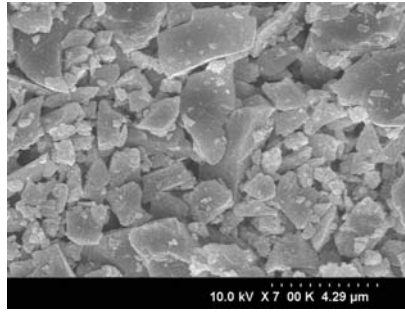


Figure 2.5 SEM of Min-u-sil 5 particles demonstrating size distribution and irregular shape

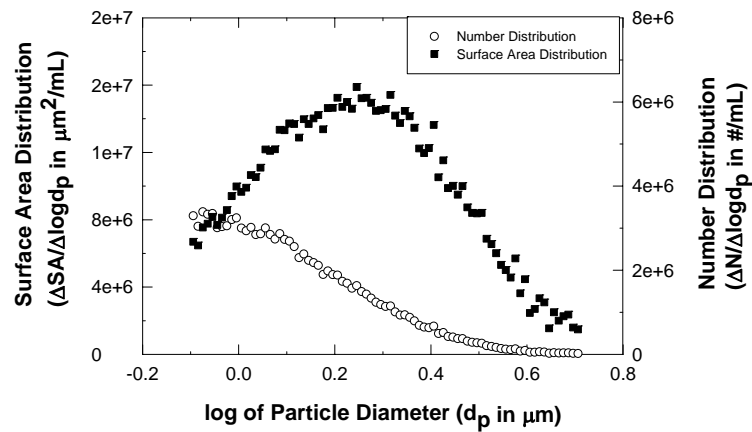


Figure 2.6 Min-u-sil particle surface area and number distributions

Cross-linked polystyrene beads (Duke Scientific Corporation; www.dukescientific.com) of size 2.02 μm were used to test the 2 μm pore size membranes, while beads of 0.65 μm were used for 0.6 μm membranes. All beads come as aqueous suspensions in 15 mL bottles that are 10% solids by weight. A volumetric flask is filled with the desired amount of pure (Milli-Q) water. The bottle of suspended beads is sonicated, and the appropriate volume of particle suspension is removed from the bottle and transferred to the volumetric flask using a Rainin electronic digital pipette accurate to 0.01 mL. This new suspension was inverted several times to ensure good mixing of the suspension.

2.4.4 Pure Water and Particulate Challenge Experiments

Pure water flux studies were conducted at room temperature with water cleaned by the Milli-Q system. Pure water experiments were done in tandem with particle challenge experiments, but the results are discussed separately. Pressure was adjusted for each membrane to allow for a reasonable length of experiment and then taken into account by reporting permeance rather than flux. Min-u-sil 5 was used in particle challenge experiments for PET membranes with pore sizes of 1, 2, and 3 μm . All studies were conducted at room temperature and at a particle concentration of 10 mg/L. The reservoir was stirred to keep the suspension concentration uniform throughout the experiment. Spherical polystyrene beads (nominal diameter 0.652 μm) from Duke Scientific Corporation were used for particle challenge studies for the 0.6 μm PET membranes and beads of nominal diameter 2.02 μm were used for the 2 μm PET membranes.

A suspension of the appropriate particle concentration was mixed to a total volume of 1 to 1.5 L. After the membrane was placed in the cell and sealed with the o-ring, 1 L of pure water, from a Milli-Q system, was added to the reservoir and the reservoir was sealed. An appropriate pressure, between 41 and 138 kPa, was chosen, and the pure water was forced through the membrane. The permeate was collected in a series of volumetric flasks and time was recorded at regular volume intervals to determine the flux through the membrane. While the membrane was still wet, the remaining pure water

was removed from the reservoir and replaced with the particulate suspension. The pressure was increased again and the suspension was forced through the membrane. Permeate samples were collected at regular volume intervals, every 25 mL for the first 150 mL of the experiment and then every 50 mL, and time was recorded at each interval. These samples were kept for analysis of particle size distribution in the permeate to determine membrane rejection. The pressure flow system took at least 45 seconds to stabilize, with the result that data for permeance was scattered for the first few samples.

2.5 SUSPENSION AND SOLUTION CHARACTERIZATION

2.5.1 Turbidimeter

One method used to characterize the particle content in the feed and permeate is to measure the turbidity. A model Hach Ratio/XR Turbidimeter (Hach Company, Loveland, CO) was used in this study. This instrument shines a light through the solution or suspension and then measures the amount of light deflected at a 90° angle to determine the turbidity or cloudiness of the suspension and reports this measurement in nephelometer turbidity units (NTU). Samples are measured by pouring 25 mL of the suspension into a clear glass tube, making sure the outside of the glass tube is clean, and inserting the tube into the turbidimeter and closing the top. Turbidity readings were taken from samples that were saved at regular intervals over the course of the permeation experiment. These samples were mixed gently before measurement to assure uniformity of particle concentration while avoiding the formation of bubbles. This method is standard (Lawler and Kweon 2003).

2.5.2 Coulter Counter

Another way to characterize permeate concentration is to measure the particle size distribution. In this research, a model Beckman-Coulter Multisizer 3 (www.beckmancoulter.com) was used, and it is shown in Figure 2.7. This instrument counts and measures the number and size of particles in the permeate, so that particle size distribution in the permeate can be known.

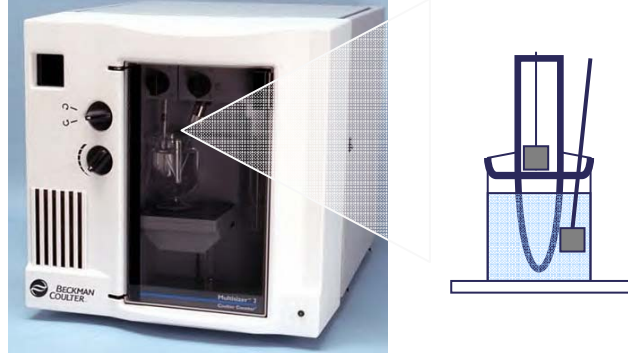


Figure 2.7 Beckman Coulter Counter, with aperture tube shown on right

A Coulter Counter draws a sample in a salt solution through an aperture across which a constant current exists. As the sample flows through the aperture, each particle causes an increase in the electrical resistance which leads, with the constant current, to a voltage pulse, given in Equation 2.1 (Chowdhury et al. 2000), that is proportional to the particle volume.

$$\Delta U = \Delta R_2 \times i \quad (2.1)$$

In Equation 2.1, ΔU is the voltage pulse height, ΔR_2 is the change in resistance caused by the particle, and i is the constant current across the aperture. A pulse height analyzer then counts and sorts the voltage pulses into size bins. The particle volume is proportional to the voltage pulse according to Equation 2.2 (Chowdhury et al. 2000):

$$\Delta V = \frac{2}{3} \left(\frac{\left(\frac{\pi}{4} D^2 \right)^2}{\rho_2} \right) \frac{\Delta U}{i} \quad (2.2)$$

in which ΔV represents the particle volume, D is the aperture used, and ρ_2 is the specific resistivity of the electrolyte without particles. A 30 μm aperture tube is calibrated to measure particles with a diameter or equivalent spherical diameter between 0.6 μm and 12 μm . A 100 μm aperture tube can measure particles in the range of 2 μm to 40 μm . The pulse height distribution information is translated via the calibration curve into a number, volume, or surface area distribution. The number distribution is given by Equation 2.3 (Chowdhury et al. 2000):

$$\frac{\Delta N_i}{\Delta \log(d_{pi})} \quad (2.3)$$

in which ΔN_i is the number of particles per milliliter in a given size range, and $\Delta \log(d_{pi})$ is the difference in the logs of those particle diameters which make up the limits of the size range being evaluated. This is plotted versus the log of particle diameter, and can be converted to a volume distribution by multiplying each number group by the volume of a spherical particle of that group's size, as shown in Equation 2.4 (Chowdhury et al. 2000).

$$\Delta N_i \times \frac{\pi}{6} d_p^3 \quad (2.4)$$

Similarly, the surface area distribution can be obtained by multiplying each number group by the surface area of a spherical particle of that group's size. Samples of both influent and from each aliquot of permeate were analyzed for their particle size distribution. Data from these samples were used to determine the effects of time, pore size, and membrane stretching on particle rejection over a range of particle sizes (Van Gelder et al. 1999).

2.6 MODEL SIMULATIONS

2.6.1 Choice of Constitutive Model

In choosing a constitutive model, the observed material behavior of PET must be considered. The PET T-E membranes demonstrate both time and temperature dependence under stress, and can be deformed, for all practical purposes, permanently (Vigny 1999). Data for the relaxation of PET at 48% by weight crystallinity was obtained by Murayama, et al which demonstrated the time and temperature dependence of PET, and gives a basis of comparison for relaxation data obtained in this study (Murayama et al. 1968). A study by Allison and Ward demonstrated that crystallinity affects the mechanical properties of PET, suggesting that testing for these properties as part of this study is in fact necessary (Allison and Ward 1967). A viscoelastic constitutive model can take into account both time and temperature dependence, but applying strains up to 40% is well beyond the linear regime of this model (Christensen 1982). Linear viscoelasticity is not capable of predicting permanent deformations.

Geometric non-linearities of stretching can be taken into account using a hyperelastic model, coupled with viscoelastic behavior (Liechti and Adamjee 1992). This model, available in the finite element simulation program ABAQUS, has been chosen to perform simulations.

2.6.2 Viscoelasticity

The following derivation follows the text of *The Theory of Viscoelasticity*, and more discussion can be found there (Liechti and Adamjee 1992). The concept of a rate dependent material, one which exhibits both elastic and viscous properties, can be most simply described with a combination of a spring, which stores energy, and a dashpot, which dissipates energy, such as those shown in Figure 2.8. The series combination of these two elements, shown as C) in Figure 2.8, is called a Maxwell element.

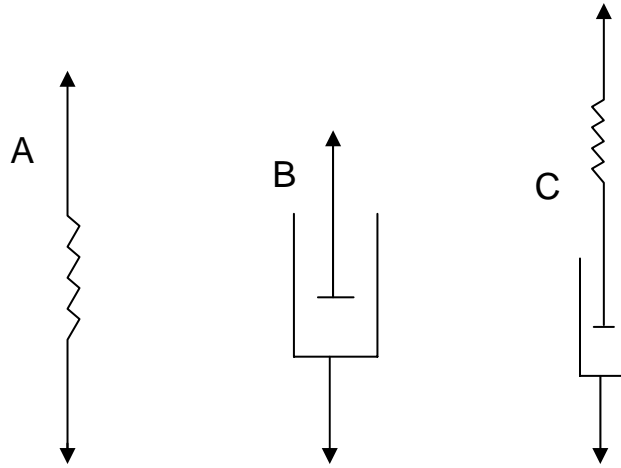


Figure 2.8 Mechanical drawing of A) Spring, B) Dashpot, and C) Maxwell element

The energy stored by a spring, or stress, is given by Equation 2.5:

$$\sigma = E\varepsilon \quad (2.5)$$

where σ is the stress in units of energy per area, E is modulus or a measure of the stiffness of the spring in the same units as the stress, and ε is the strain, which has no units. The energy dissipated by the dashpot is given by the Equation 2.6:

$$\sigma = \eta \frac{d}{dt} \varepsilon \quad (2.6)$$

where η is similar to E . For these elements in series, the stresses in each element must be equal, and the strains additive. Solving the above equations for strain, or more specifically the first time derivative of strain and adding them gives Equation 2.7:

$$\frac{d}{dt}\varepsilon = \frac{1}{E} \frac{d}{dt}\sigma + \frac{\sigma}{\eta} \quad (2.7)$$

where σ is the stress in either element, since they are necessarily equal. To measure the relaxation of this assembly, a strain is applied and held constant such that stress declines over time due to the dissipation of energy. If this strain is called ε_0 , then substituting this value in to the above equation results in the following differential equation.

$$0 = \frac{1}{E} \frac{d}{dt}\sigma + \frac{\sigma}{\eta} \quad (2.8)$$

Equation 4 can be solved for stress to give Equation 2.9:

$$\sigma = E\varepsilon_0 e^{-\frac{t}{\tau}} \quad (2.9)$$

where τ is η/E . From this expression, the relaxation modulus can be written as

$$E(t) = \frac{\sigma(t)}{\varepsilon_0} \quad (2.10)$$

Another representation of viscoelastic behavior is the Voigt-Kelvin element, which is also made up of a spring and dashpot, but arranged in parallel as shown in Figure 2.9 (Christensen 1982).

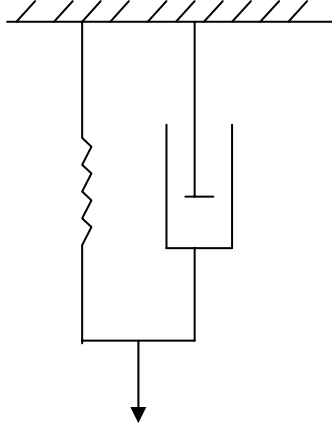


Figure 2.9 Voigt-Kelvin element

In this case, stresses are additive and strains are equal. Using the same procedure as above, the differential equation describing this element, Equation 2.11, can be derived as

$$\sigma = E\varepsilon + \eta \frac{d}{dt} \varepsilon \quad (2.11)$$

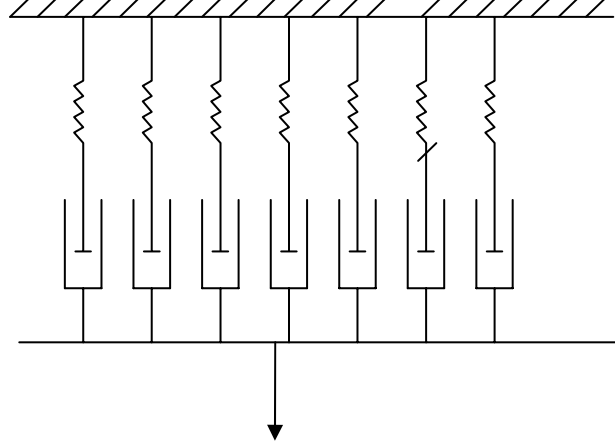


Figure 2.10 Generalized Maxwell model

The generalized Maxwell model is a combination of Maxwell elements in parallel with each other, as shown in Figure 2.10. Equation 2.11 can be written for each individual Maxwell element in the generalized Maxwell model. Because the elements are in parallel, the stresses of each Maxwell element are additive. Summing these stresses gives Equation 2.12:

$$\sigma(t) = \sum_{i=1}^N E_i \left[e^{\frac{-t}{\tau_i}} \varepsilon(0) + \int_0^t e^{\frac{-(t-\zeta)}{\tau_i}} \frac{d}{d\zeta} \varepsilon d\zeta \right] \quad (2.12)$$

where E_i is the modulus of element i , and N is the total number of Maxwell elements. Note that as time (t) approaches infinity, the stress goes to 0, demonstrating that Maxwell elements can relax completely. Because this behavior is not what is observed, a combination of Maxwell, Voigt-Kelvin, and individual springs and dashpots can be used to create a model that more accurately described the desired material behavior. Examples of such combinations are the standard linear solids.

In a relaxation experiment, the strain can be applied and written as a Heaviside step function as expressed in Equation 2.13.

$$\varepsilon = \varepsilon_0 H(t) \quad (2.13)$$

where $H(t)$ is the Heaviside step function. Substituting this into the above equation gives the relaxation modulus as a series of exponentials as shown in Equation 2.14.

$$E(t) = \sum_i E_i e^{\frac{-t}{\tau_i}} \quad (2.14)$$

For a model that has a spring in parallel with a series of Maxwell elements, the relaxation modulus takes on the form of Equation 2.15:

$$E(t) = E_1 + \sum_i E_i e^{\frac{-t}{\tau_i}} \quad (2.15)$$

where E_1 is the modulus of the individual spring. This form is a convenient way of expressing the relaxation modulus known as the Prony series (Hibbitt 1998), which can be written generally as Equation 2.16:

$$E(t) = E_e + \sum_i E_i e^{\frac{-t}{\tau_i}} \quad (2.16)$$

where E_e is the equilibrium relaxation modulus. This series of exponentials represents a modulus that takes the form shown in Figure 2.11. This is called the *master curve*, and can be constructed experimentally through a series of relaxation experiments as described in the next section.

2.6.3 Relaxation Experiments

Relaxation experiments, similar to the stretching experiments described above, must be performed using dense films in order to create the master curve, from which the Prony series can be constructed. The sample preparation is the same as described above in section 2.3.2, except that samples are between 0.2 and 0.4 cm wide. The samples are loaded into the machine so that force data can be recorded, they are pre-tensioned, and then they are heated to the desired temperature and left there for 30 minutes to ensure equilibrium. Another pre-tensioning takes place after the sample has reached the desired temperature, and then the chosen strain, between 0.3 and 2%, is applied while force data are recorded. The sample is allowed to relax over a period of 30 to 45 minutes while remaining constrained at the applied strain. This method is standard, and follows that found in the literature (Brostow et al. 1999). These experiments were done at temperatures ranging from room temperature to 180°C.

2.6.4 Master Curve Construction

Once relaxation experiments have been done, the data can be transformed into the master curve. Force is translated to stress by dividing by sample thickness, h , and width, w , as shown in Equation 2.17.

$$\sigma(t) = \frac{F(t)}{wh} \quad (2.17)$$

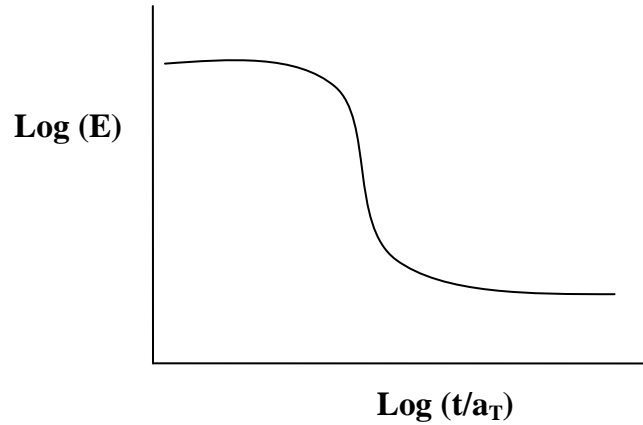


Figure 2.11 Qualitative master curve

This stress is translated to relaxation function by dividing by the constant strain applied to the sample, as shown in Equation 2.18.

$$E(t) = \frac{\sigma(t)}{\gamma} \quad (2.18)$$

Using the Williams-Landel-Ferry (WLF) equation, Equation 2.19 (Williams et al. 1955)], the individual experiments are shifted to form a master curve, qualitatively shown in Figure 2.11. The *shift factor*, a_T , is calculated by Equation 2.19 where the reference temperature, T_r , is taken to be 50°C above the glass transition of the polymer being studied and T is the temperature at which the relaxation experiment took place.

$$\log(a_T) = \frac{86.6(T - T_r)}{101.6 + (T - T_r)} \quad (2.19)$$

Reduced time, t' , is given by Equation 2.20.

$$t' = \frac{t}{a_T} \quad (2.20)$$

The log of the relaxation function, E , is plotted against the log of reduced time for experiments at various temperatures, and the master curve, shown qualitatively in Figure 2.13, is obtained.

2.6.5 Prony Series Construction

The curve shown in Figure 2.11 can be described mathematically as the sum of a series of exponential terms, called the Prony series, which is shown in Equation 2.21. The coefficients of these terms, μ_K , are required by ABAQUS to describe the material behavior.

$$\mu(t) = \mu_e + \sum_{k=1}^n \mu_k e^{\frac{-t}{\tau_k}} \quad (2.21)$$

There are two well-known methods for obtaining these coefficients. The first is a collocation procedure. A number, N , of decades of time are chosen over the transition region. A time, τ_K , is chosen in each decade, and the value of the relaxation modulus, shown above as $\mu(t)$, is known at each τ_K . A set of N equations can be written, an example of which is Equation (2.22).

$$\mu_1 e^{\frac{-t_1}{\tau_1}} + \mu_2 e^{\frac{-t_1}{\tau_2}} + \mu_3 e^{\frac{-t_1}{\tau_3}} + \dots + \mu_N e^{\frac{-t_1}{\tau_N}} = \mu(t_1) - \mu_e \quad (2.22)$$

These equations can then be represented as a matrix, such as Equation (2.23), and the values for μ_K can be obtained by solving the matrix.

$$\begin{bmatrix} e^{\frac{-t_1}{\tau_1}} & e^{\frac{-t_1}{\tau_2}} & e^{\frac{-t_1}{\tau_3}} & e^{\frac{-t_1}{\tau_4}} & e^{\frac{-t_1}{\tau_5}} & e^{\frac{-t_1}{\tau_6}} \\ 0 & e^{\frac{-t_2}{\tau_2}} & e^{\frac{-t_2}{\tau_3}} & e^{\frac{-t_2}{\tau_4}} & e^{\frac{-t_2}{\tau_5}} & e^{\frac{-t_2}{\tau_6}} \\ 0 & 0 & e^{\frac{-t_3}{\tau_3}} & e^{\frac{-t_3}{\tau_4}} & e^{\frac{-t_3}{\tau_5}} & e^{\frac{-t_3}{\tau_6}} \\ 0 & 0 & 0 & e^{\frac{-t_4}{\tau_4}} & e^{\frac{-t_4}{\tau_5}} & e^{\frac{-t_4}{\tau_6}} \\ 0 & 0 & 0 & 0 & e^{\frac{-t_5}{\tau_5}} & e^{\frac{-t_5}{\tau_6}} \\ 0 & 0 & 0 & 0 & 0 & e^{\frac{-t_6}{\tau_6}} \end{bmatrix} \begin{bmatrix} \mu_1 \\ \mu_2 \\ \mu_3 \\ \mu_4 \\ \mu_5 \\ \mu_6 \end{bmatrix} = \begin{bmatrix} \mu(t_1) - \mu_e \\ \mu(t_2) - \mu_e \\ \mu(t_3) - \mu_e \\ \mu(t_4) - \mu_e \\ \mu(t_5) - \mu_e \\ \mu(t_6) - \mu_e \end{bmatrix} \quad (2.23)$$

The other well-known method for obtaining these coefficients is the least squares method, in which a value for μ_K is guessed, and the error between the calculated value for $\mu(t)$ and the actual one is minimized. The total squared error is given by Equation 2.24.

$$E^2 = \int_0^\infty (\mu(t) - \mu(t_1))^2 dt \quad (2.24)$$

To minimize the error in μ_K , the derivative of this function is taken with respect to μ_K , and this is given in Equation 2.25.

$$\frac{d}{d\mu_K} E^2 = -2 \int_0^\infty (\mu(t) - \mu(t_1)) e^{\frac{-t}{\tau_K}} dt = 0 \quad (2.25)$$

This is done N times to solve for all of the μ_K .

The least squares method was used to fit the Prony series here. The collocation method, after much manipulation, resulted in negative coefficients, and therefore the results of that method could not be used.

2.6.6 Hyperelasticity

The behavior of a hyperelastic material is a total stress–strain relationship. In employing finite elements to solve hyperelastic models, the principle of virtual work is used, meaning equilibrium equations are not solved. Instead, the strain energy is used to solve for stress or strains in the material. The strain energy is defined as the energy stored in a body due to deformation caused by external loads. The strain energy density U_0 is the strain energy per unit of volume, and is defined mathematically (Cook 1998)

$$U_0 = \int_0^\epsilon \sigma d\epsilon \quad (2.26)$$

The strain energy can be found by taking the integral over the volume of the body as in Equation 2.27 (Cook 1998).

$$U = \int U_0(x, y, z) dV \quad (2.27)$$

Several models have been developed for representing the strain energy function. If the deformation gradient is defined as

$$F = \frac{dx}{dX} \quad (2.28)$$

where X is the location of a point on the material in the pre-deformed state and x is the location of that same point in the deformed state, then the deformation tensor B is given by (Cook 1998)

$$B = FF^T \quad (2.29)$$

For an isotropic hyperelastic material, B must be able to be written as a function of the three principle invariants, given by (Hibbitt 1998)

$$\begin{aligned} I_1 &= tr(B) \\ I_2 &= \frac{1}{2}(tr(B))^2 - tr(B^2) \\ I_3 &= \det(B) \end{aligned} \quad (2.30)$$

The strain energy can be written as a polynomial combination of these invariants in many forms, such as the neo-Hookean, Mooney-Rivlin, and Ogden. The general polynomial form is given by (Hibbitt 1998)

$$U = \sum_{i+j=1}^N C_{ij} (I_1 - 3)^i (I_2 - 3)^j + \sum_{i=1}^N \frac{1}{D_i} (J_{el} - 1)^{2i} \quad (2.31)$$

where J_{el} is the elastic volumetric strain and C and D are temperature-dependent parameters that differ from material to material. The value of D represents the compressibility of the material, a value of 0 meaning the material is fully incompressible. If $N = 1$ in Equation 26, the Mooney-Rivlin form results, as shown in Equation 2.32 (Hibbitt 1998).

$$U = C_{10}(I_1 - 3) + C_{01}(I_2 - 3) + \frac{1}{D}(J_{el} - 1)^2 \quad (2.32)$$

Other forms of the strain energy function can be obtained by setting some of the coefficients equal to 0 or defining N . If the coefficients C_{01} are set to 0, as in the reduced polynomial form, and N is set to 1, the neo-Hookean form is obtained, as in Equation 2.33 (Hibbitt 1998).

$$U = C_{10}(I_1 - 3) + \frac{1}{D_1}(J_{el} - 1)^2 \quad (2.33)$$

The Arruda-Boyce form of the hyperelastic potential takes the form of Equation 2.34, where C_1 through C_5 are defined constants and μ and λ are material dependent parameters (Hibbitt 1998).

$$U = \mu \sum_{i=1}^5 \left[\frac{C_i}{\lambda_m^{2i-2}} (I_1^i - 3^i) \right] + \frac{1}{D} \left[\frac{J_{el}^2 - 1}{2} - \ln(J_{el}) \right] \quad (2.34)$$

The Marlow model takes the form of Equation 2.35:

$$U = U_D(I_1) + U_V(J_{el}) \quad (2.35)$$

where U is the strain energy per unit of reference volume, divided into deviatoric, U_D , and volumetric, U_V , components (Hibbitt 1998). The neo-Hookean, Arruda-Boyce, and Marlow models depend only on the first invariant. Dependence on the second invariant, as in the Mooney-Rivlin, is likely to lead to error or a bad fit because in this case only uniaxial test data is available. The Arruda-Boyce and Marlow models were used in this study because they depend only on the first invariant and were able to fit the data.

2.6.7 ABAQUS Representations

Another representation of the stress-strain history for the viscoelastic model is the integral representation. It is supposed that any stress or strain history can be considered as the summation of many small step functions. As the size of the steps approaches 0, the following expression is obtained:

$$\sigma(t) = E(t)\varepsilon_0 + \int_0^t E(t-\zeta) \frac{d\varepsilon(\zeta)}{d\zeta} d\zeta \quad (2.36)$$

ABAQUS begins with a similar representation, given in Equation 2.37 (Hibbitt 1998):

$$\sigma(t) = \int_0^t 2G(\tau - \tau') \frac{de}{dt} dt' + \int_0^t K(\tau - \tau') \frac{d\phi}{dt} dt' \quad (2.37)$$

where e and ϕ are the mechanical deviatoric and volumetric strains, K is the bulk modulus, and G is the shear modulus. These moduli are expressed in ABAQUS in terms of the Prony series, as shown in Equation 2.38 (Hibbitt 1998).

$$K(\tau) = K_e + \sum_{i=1}^{n_K} K_i e^{\frac{-\tau}{\tau_i^K}} \quad (2.38)$$

$$G(\tau) = G_e + \sum_{i=1}^{n_G} G_i e^{\frac{-\tau}{\tau_i^G}}$$

where K_i , G_i , τ_i^K , and τ_i^G are input by the user. In ABAQUS, the WLF shift equation takes the form of Equation 2.39:

$$\log(A_\theta) = C_1 \frac{(\theta - \theta_0)}{C_2 + (\theta - \theta_0)} \quad (2.39)$$

where θ_0 is the chosen reference temperature, and the constants C_1 and C_2 are related to the universal constants by Equation 2.40:

$$C_1 = \frac{C_1^g}{1 + \frac{(\theta_0 - \theta_g)}{C_2^g}} \quad (2.40)$$

$$C_2 = C_2^g + \theta_0 - \theta_g$$

where C_1^g and C_2^g are the universal constants and θ_g is the glass transition temperature (Hibbitt 1998).

2.6.8 Constant Strain Rate Experiments

In order to obtain material data describing the nonlinearity of elasticity in terms of a hyperelastic model, constant rate stretching experiments were performed. These experiments were similar to the stretching experiments described in section 2.3.3. Samples were cut, aligned, and heated as described above. Stretching was conducted at a constant rate, either 1 or 3 cm/s, at temperatures ranging from 100 to 160°C. The samples were stretched until they broke, and force data was recorded as a function of time. Strain was calculated from the strain rate and time data, and stress was plotted as a function of strain. This data was used to fit hyperelastic models in ABAQUS.

2.6.9 Model Simulation

An input file must be written for ABAQUS in order to construct the mesh. Nodes are assigned to locations, and the appropriate elements are chosen to connect the nodes and create the mesh. Elements of type CPS4, which are 4 node continuum elements for plane stress analyses were used for the two-dimensional simulations. There are also shell, beam, rigid, infinite, and truss type elements, among others. Next, elements are assigned material properties, such as elastic or viscoelastic, and the appropriate parameters are entered to describe the material behavior. For example, the case of a viscoelastic material, described above, will require the coefficients of the Prony series. Other initial

conditions can also be set, such as temperature. A node set is created out of existing nodes along one side of the mesh, and a displacement is assigned to this node set, effectively applying strain to the sample. The output from ABAQUS is specified in the input file, so that values of displacement and stress can be read at different nodes or for different elements. ABAQUS also outputs a picture of the deformed membrane, which can then undergo digital image analysis like an SEM picture to determine the change in pore size and shape. A film with one pore can be stretched, and the results can be compared directly to an experimentally stretched pore that is not interacting with other pores. Membrane stretches were simulated at 80, 120, and 160°C and at rates of 0.1, 0.55, and 1 cm/s to various strains. Membranes were annealed and cooled in the simulation as well in order to determine rebound and compare that with the experimental rebound of the membrane that is observed.

The next step is to simulate the stretching of a film with two pores in it. The distance between pores, as well as their orientation relative to the stretch direction, was being varied to determine the extent of their interaction. These simulations followed the form on the one-hole simulations. Results of these simulations are more difficult to compare directly to experimental results since it is difficult to determine from an SEM of a stretched membrane the orientation and distance between pores before stretching, but these simulations will give information about interaction effects between pores.

Another way to form meshes is to use a drawing program called ABAQUS CAE. This program writes the .inp file by following the same basic procedure in a user-friendly program. Membrane are drawn, properties assigned, and boundary conditions are given. The size of the mesh can be chosen, and the membrane is meshed automatically by the program. Steps are chosen, and the program can be run and results can be viewed. This program allows multiple hole studies to be drawn and simulated. Single pore and two-pore meshes were drawn in CAE and the results compared to the input file results to determine if either simulation was in error due to the mesh. Multiple pore meshes were also drawn and stretched in CAE corresponding to the porosity of membrane samples stretched experimentally, including overlapping pores, and compared to experimental results.

One of the outputs from ABAQUS that is useful for this study is the von Mises stress distribution. This picture can be used for digital image analysis, but it can also give information about the shape of the stress distribution and where the areas of concentrated stress are occurring. An example of this output is given in Figure 2.12. The red areas represent the highest stress, and the blue the lowest.

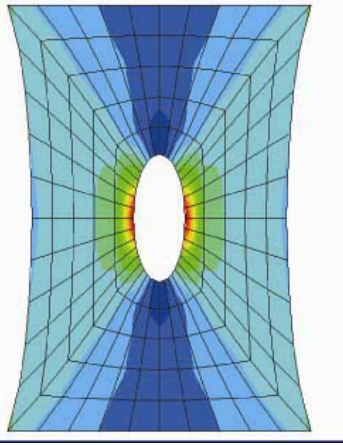


Figure 2.12 Von Mises stress distribution from ABAQUS showing areas of highest stress in red

CHAPTER 3: RESULTS and DISCUSSION

3.1 PRE-STRETCHED MEMBRANE MATERIALS CHARACTERISTICS

Pore characteristics were analyzed for all PET membranes before stretching. Pore area, pore major axis, and pore minor axis were measured per the procedure described in the previous section. Although the method of manufacturing T-E membranes produces circular pore entrances, the aspect ratio of the non-stretched samples is greater than one due to the overlapping of pores as shown in Figure 1, as well as the fact that some pores are not perpendicular to the membrane surface. Table 3.1 gives a summary of these results for all the PET membranes used in this project, including 95% confidence limits, which are reported for all membrane surface measurements. Reported area is defined as the average area of an individual pore. The area of approximately 200 pores per membrane was determined by the Scion software and the average is reported. *Porosity* is defined as the total area of membrane that is porous divided by the total membrane area. *Pore density* was measured by counting the number of pores on the surface of the membrane and reporting it as *count/total area*. The digital image analysis software counts pores, but it counts overlapping pores, such as a group of 2 pores, as one pore. These overlapping pores had to be counted by hand and added to the total number of pores, which was then divided by the surface area of the membrane to get pore density. These results were used to compare stretched samples with their non-stretched state and determine the change in pore characteristics. Because the digital image analysis software accounts for these groups as one pore, membranes with higher pore densities are more likely to have higher values and broader ranges for major axis and pore area.

Table 3.1
Pore characteristics for non-stretched track-etched membranes

Nominal Pore Size (μm)	Area (μm^2)	Major Axis (μm)	Minor Axis (μm)	Aspect Ratio (--)	Porosity (--)	Pore Density (# pores/ cm^2)	Thickness (μm)
0.2	0.03 ± 0.01	0.21 ± 0.01	0.16 ± 0.01	1.24 ± 0.03	0.134 ± 0.010	$5.25\text{E}+08$	23
0.4	0.14 ± 0.02	0.48 ± 0.04	0.37 ± 0.01	1.30 ± 0.09	0.175 ± 0.010	$1.30\text{E}+08$	23
0.6	0.26 ± 0.02	0.66 ± 0.03	0.53 ± 0.01	1.23 ± 0.05	0.095 ± 0.009	$3.91\text{E}+07$	22
0.8	0.44 ± 0.03	0.81 ± 0.04	0.67 ± 0.02	1.24 ± 0.07	0.151 ± 0.016	$4.00\text{E}+07$	22
1.0	0.71 ± 0.03	1.02 ± 0.04	0.89 ± 0.01	1.18 ± 0.06	0.010 ± 0.001	$1.49\text{E}+06$	22
2.0	2.22 ± 0.12	1.87 ± 0.08	1.48 ± 0.04	1.26 ± 0.04	0.062 ± 0.006	$2.67\text{E}+06$	21
3.0	6.02 ± 0.67	3.16 ± 0.29	2.39 ± 0.04	1.31 ± 0.11	0.150 ± 0.018	$3.30\text{E}+06$	20
10.0	65.4 ± 3.98	10.1 ± 0.58	8.20 ± 0.12	1.24 ± 0.07	0.080 ± 0.013	$1.37\text{E}+05$	13

3.2 STRETCHED MEMBRANE MATERIALS CHARACTERISTICS

3.2.1 Stretching Experimental Results

The first membrane to be characterized was the 2 μm PET membrane. A 2nd order surface response experimental design, generated using JMP software, was utilized to determine the experiments needed to quantify fully the effects of strain, strain rate, and temperature, including any interaction effect, on the pore size and shape characteristics. This design was chosen because it was capable of taking into account nonlinear response. Temperatures of 80, 120, and 160°C; strain rates of 0.1, 0.55, and 1 cm/s; and total strains of 5, 22.5, and 40% were used for this design. The software suggested experiments that were not physically possible due to membrane breakage; for example, it was not possible to stretch the 2 μm PET membrane 40% at 80°C. In these cases, the matrix was redefined so that these experiments were excluded and executable experiments were added to the matrix. The set of experiments performed is shown in Table 3.2. Strain is shown as the actual strain measured after stretching, annealing, and cooling the sample.

Table 3.2:
**Experimental design for studying pore area, major
and minor axes, aspect ratio, and porosity**

Applied Strain (%)	Strain Obtained (%)	Temperature (°C)	Strain Rate (cm/s)
5.0	3.9	80	1.0
5.0	3.9	120	0.55
5.0	4.5	120	0.55
5.0	5.0	160	0.1
10.0	8.7	160	1.0
22.5	17.1	100	0.1
22.5	17.3	80	0.55
22.5	17.8	100	1.0
22.5	19.8	160	0.55
22.5	20.0	120	0.55
22.5	20.0	120	0.55
22.5	20.1	120	0.55
22.5	20.4	120	0.1
25.0	23.5	120	0.55
25.0	23.5	120	0.55
25.0	24.1	120	0.55
30.0	27.0	120	1.0
30.0	27.4	120	0.55
40.0	37.1	160	0.1
40.0	38.9	160	1.0

Experiments were performed using the refined experimental design, SEM micrographs were taken of all samples, and these micrographs were analyzed using the digital image analysis technique discussed in the previous section. Statistical analysis of the data for the experiments showed that pore area and geometry were not significantly dependent on temperature and strain rate for the range of these parameters studied here.

Consequently, the experimental results reported here for the 0.2 μm PET membrane all represent membranes stretched at the conditions described in the paragraph above.

Figure 3.1 shows the effect of stretching on pores, giving an SEM of both a non-stretched and stretched samples of the 2 μm PET membrane. Major axis is visibly increasing significantly, as is pore area, but the change to minor axis is less noticeable. This trend is apparent for all stretched samples shown in this study.

Major and minor axes were measured for each pore, and these results are given in Figure 3.2. Major axis increases linearly with strain, almost doubling in length at 40% total strain. The minor axis undergoes a relatively small linear decrease with increasing strain. At the highest strains, the change in the minor axis is no more than 15%, much less than the 100+% change in major axis. At low strain, the stress causes the pore to deform without significant stretching of the actual material, causing the initial increase in major axis. Evidence supporting the statement that the deformation of the pores dominates the overall change in the film is given in Figure 3.3, where the stress–strain curves for the porous and dense films stretched at 160°C and 0.1 cm/s are compared. The initial slope of the curve for the membrane is lower, showing that less force is required to stretch the membrane than the dense film. This is also supported by the results of the modeling study, which are discussed in the “Modeling Results” chapter. As strain is increased beyond the initial few percent, the stress in the material begins to increase as the major axis continues to increase and the material stretches.

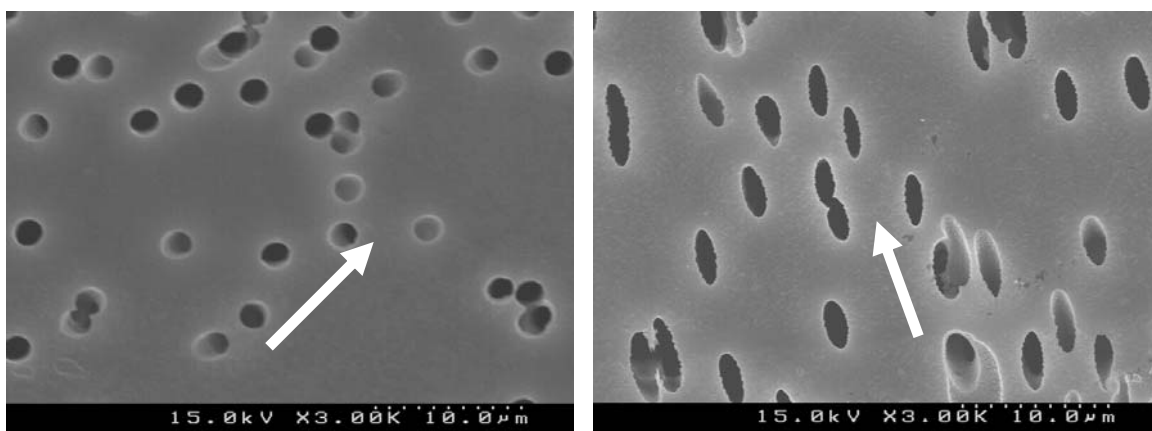


Figure 3.1 PET membrane of nominal pore size 2 μm , shown non-stretched (left) and stretched (right). The arrow in both micrographs indicates the machine direction, which also corresponds to the stretch direction. This membrane was stretched at 160°C and 1 cm/s to a total strain of 0.40

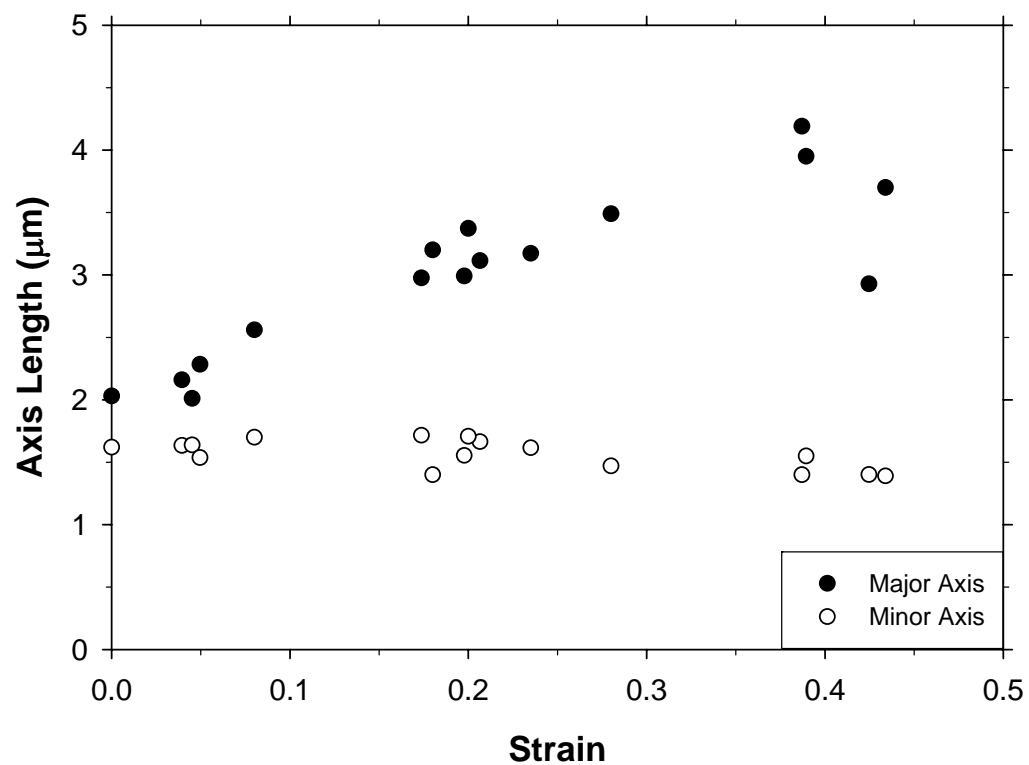


Figure 3.2 Effect of strain on major and minor axis dimensions in a 2 μm pore size T-E membrane

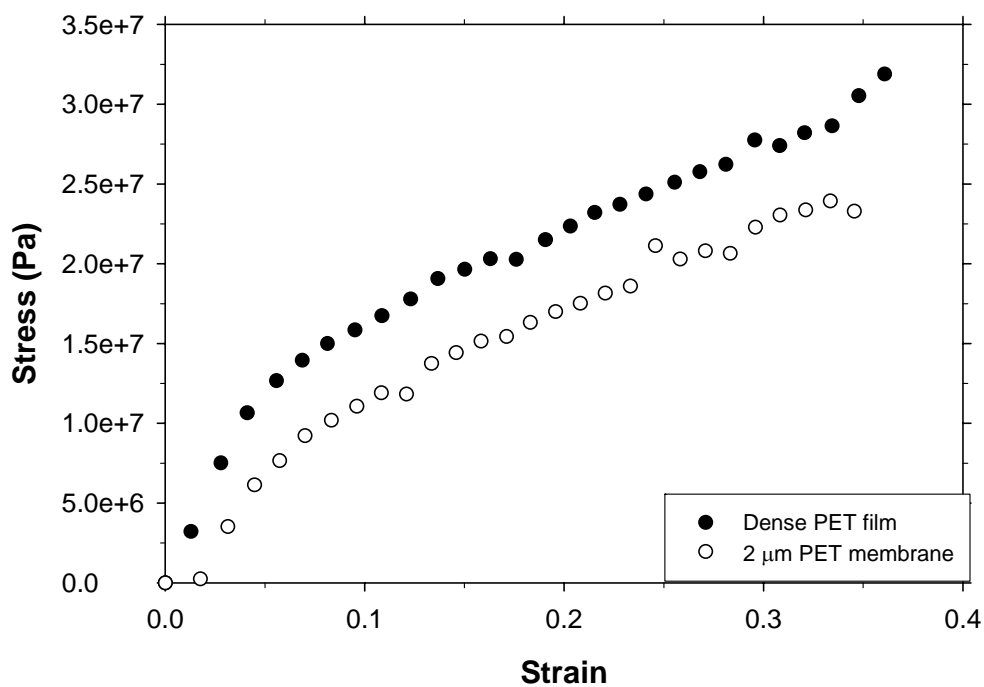


Figure 3.3 Stress-strain curve comparison between dense film and 2 μm PET membrane at 160°C and 0.1 cm/s

As shown in Figure 3.4, aspect ratio increases linearly with increasing strain. This increase is a consequence of the fact that the major axis increases to a greater extent than the minor axis decreases. For a strain of 40%, the increase in major axis is 97% and the decrease in minor axis is 11.5%. The aspect ratio is measured to increase by 158%, which corresponds to the ratio of these two parameters.

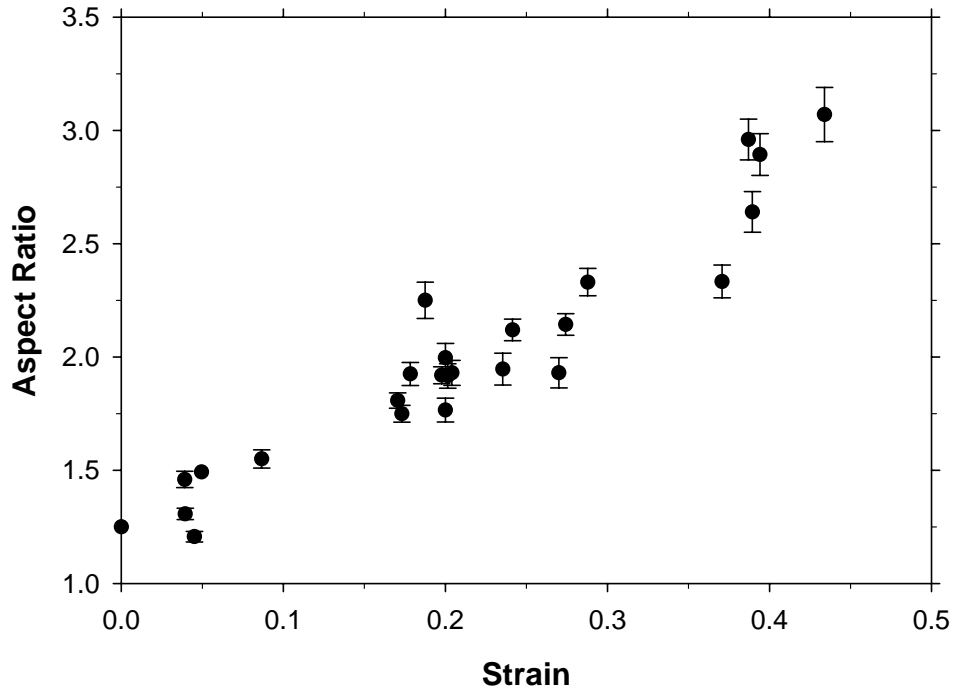


Figure 3.4 Effect of strain on aspect ratio in a 2 μm pore size T-E membrane

Average pore area also increases linearly with increasing strain, as shown in Figure 3.5. If the elongated pores are assumed to be elliptical (as Figure 3.1 indicates), the pore area can be calculated as follows:

$$\text{Area} = a \cdot b \cdot \pi \quad (3.1)$$

where a represents one half the major axis and b is one half the minor axis. Because area is a linear function of major and minor axis, and both axes change linearly with strain, it then follows that pore area should change linearly with strain for low strains. When the 0.2 μm PET sample is subjected to a strain of 0.40, the major axis increases by $97 \pm 6\%$ and the minor axis decreases by $12 \pm 5\%$. Using the above values for major and minor axis and the equation given above, the area of an elliptical pore would increase by $74 \pm 6\%$. The fact that the measured increase in area is $79 \pm 15\%$ indicates that representing the elongated pores as elliptical is a reasonable first approximation. However, it should be noted that when pores are in close proximity with each other, orientation to high strains such as 0.40 causes the pores to distort to non-elliptical shapes, as shown in Figure

3.6. These interaction effects can be predicted by modeling the stretching process, as discussed in the “Modeling Results” chapter.

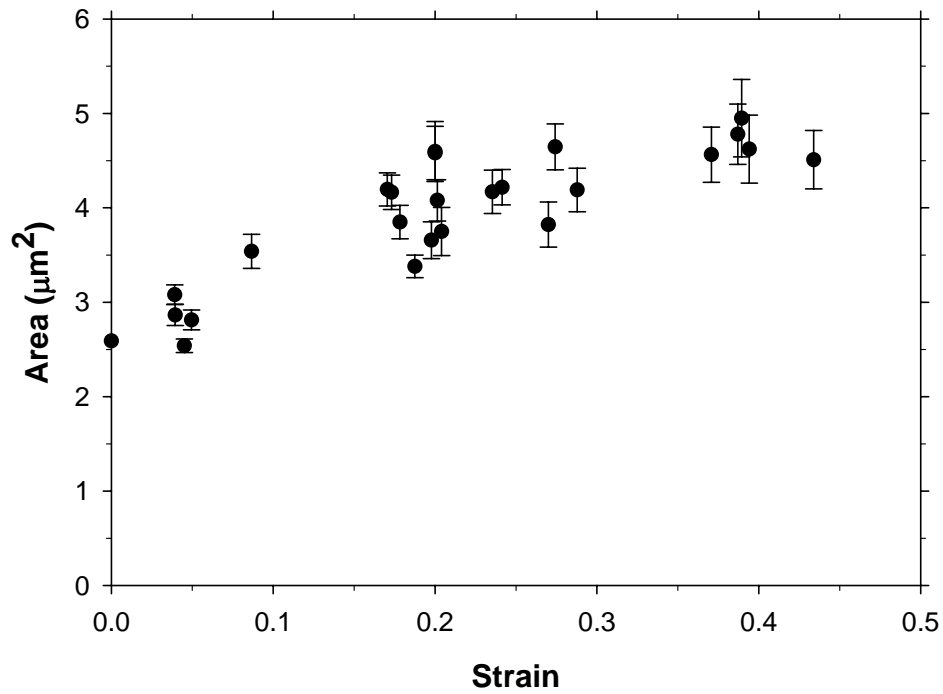


Figure 3.5 Effect of strain on area for a 2 μm pore size T-E membrane

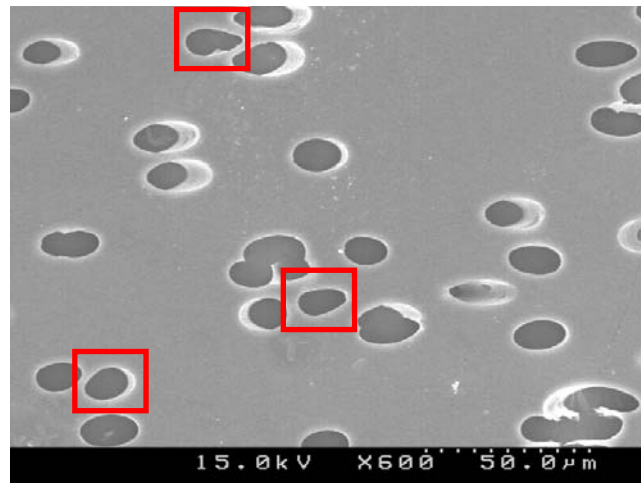


Figure 3.6 SEM of 10 μm PET stretched 18% demonstrating non-elliptical pores resulting from pore interactions during stretching

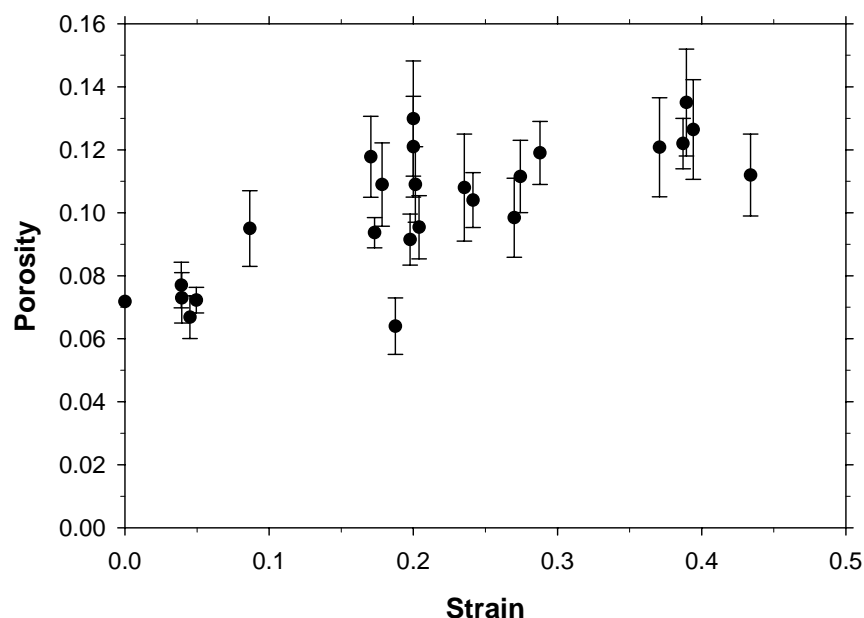


Figure 3.7 Effect of strain on porosity for a 2 μm pore size T-E membrane

The increase in the area of individual pores directly impacts the change in surface porosity. This effect is apparent in Figure 3.7, in which surface porosity increases linearly with increasing strain. The scatter in the data and the size of the confidence limits in Figure 3.7 are greater for the porosity than for the pore area or the measured dimensions in the previous figures because fewer porosity measurements can be made. Only one porosity measurement can be taken per image, giving only ten total measurements compared to approximately 200 values going into the determination of the other measures.

The data shown above in Figures 3.2, 3.4, 3.5 and 3.7 were for experiments performed at the range of temperatures and strain rates chosen for the experimental design. They are shown as functions of strain only, and are linear in that parameter,

suggesting little or no dependence on the other parameters tested, temperature and strain rate. Statistical analysis using JMP software showed that within the range of variables studied here, pore size and shape characteristics were independent of temperature and strain rate, and depended only on total strain. Although temperature and rate had a large effect on how much strain could be applied to the membrane before breaking, strain alone dictated the pore characteristics.

Thickness was also studied as a parameter. Samples were placed on the edge of the SEM stage, and pictures were taken of the cross section of each membrane, stretched and non-stretched samples, so that thickness could be measured. An example of such a picture is shown in Figure 3.8. Between 2 and 4 pictures were taken of each sample, and 2 to 3 measurements were taken for each picture. Measurements vary by one or two microns, giving this method an average error of 5 to 10%. These results were entered into JMP so that the mean and 95% confidence interval could be determined for each set of data. The results are summarized in Figure 3.9. Thickness measurements have more error than those of pore area or aspect ratio, but it is evident that little or no change in thickness occurs upon stretching. The fact that the thickness does not change measurably can be attributed to the fact that the strain is changing the pore area. For example, if the membrane with nominal pore size 2 μm is subject to a 0.21 strain, the total membrane area increases by 17%, while the pore area increases by 67%. Because the membrane has a porosity of 7% before stretching and 12% after stretching, the change in pore area accounts for 6% of the change in total membrane area. This shows that strain is being applied to the polymer, not just to the pores, and that thickness should change. This change in thickness follows Equation 3.2

$$\varepsilon' = \nu \cdot \varepsilon \quad \text{-(3.2)}$$

in which ε is the total strain, and ε' is the strain in the direction of thickness [32]. The Poisson ratio can be assumed to be approximately 0.5 for a rubbery material [33], which means for the sample above, thickness should decrease by 1.2 μm . This amount is within the error of this measurement, so it is not surprising that no change in thickness is measured.

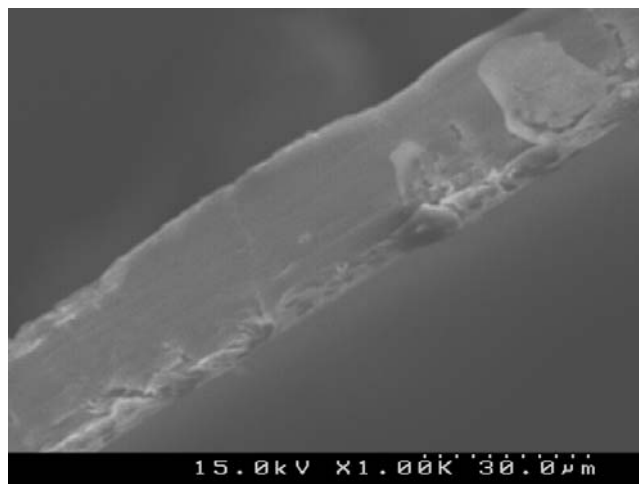


Figure 3.8 SEM of a cross section of a PET track-etched membrane

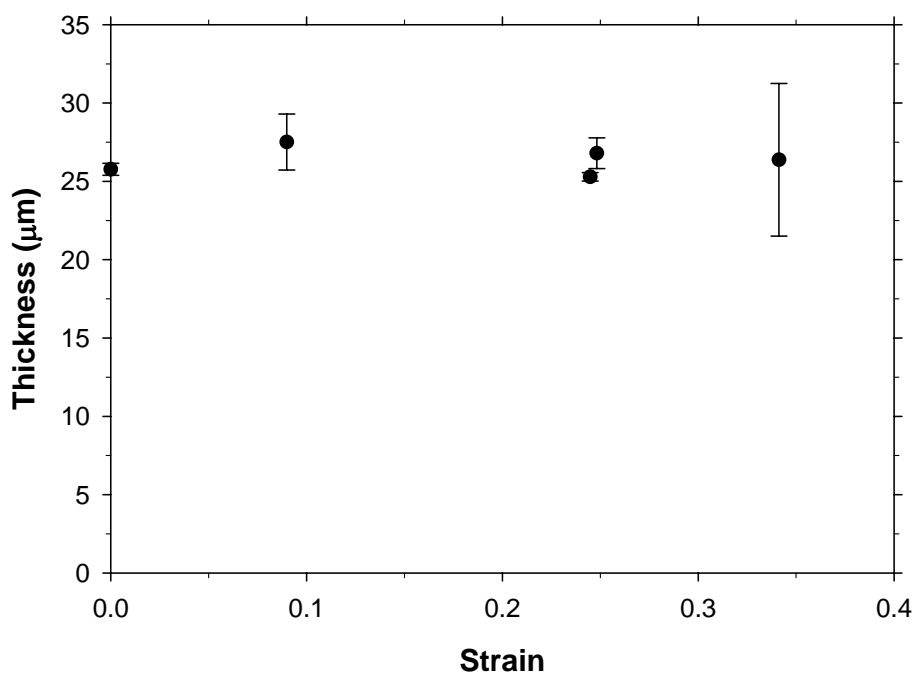


Figure 3.9 Results of thickness study for stretching 2 μm PET membranes at various temperatures and rates

In addition to the detailed study of the 2 μm PET membranes discussed above, PET membranes with pore sizes ranging from 0.2 to 10 μm were stretched at various combinations of temperature, strain rate, and overall strain. Recall that the preliminary studies using the 2 μm PET indicated the change in pore size characteristics was

independent of temperature and strain rate in the range of these parameters studied here. Consequently, the results reported below are for a variety of temperature – rate combinations. As indicated in Table 4.1, the pre-stretched membranes varied widely in surface porosity, pore density, and membrane thickness, all of which influence the maximum strain attainable prior to breaking of the membrane. As discussed below, some membranes were only successfully stretched to small strains, such as 5 or 10%, and others were stretched up to 32% before breaking.

For a given set of stretching conditions, the point at which a membrane catastrophically fails, or breaks, depends on the porosity, pore size, pore density, and membrane thickness. The largest stretch attained for each membrane was plotted against each of these parameters individually, as well as thickness divided by porosity. Because the thickness of the membrane was shown to stay constant with stretching, the value of thickness used is the same for both stretched and non-stretched. Porosity increases upon stretching linearly with strain, so the initial value, or the value of the non-stretched membrane, was also used here. The graph of strain versus thickness and porosity, shown in Figure 3.10, gave the least scatter in the data and showed that in general, a membrane with higher porosity and lower thickness is more likely to break than its counterpart with low porosity and higher thickness. The strain at which a membrane breaks loosely correlates to thickness divided by porosity.

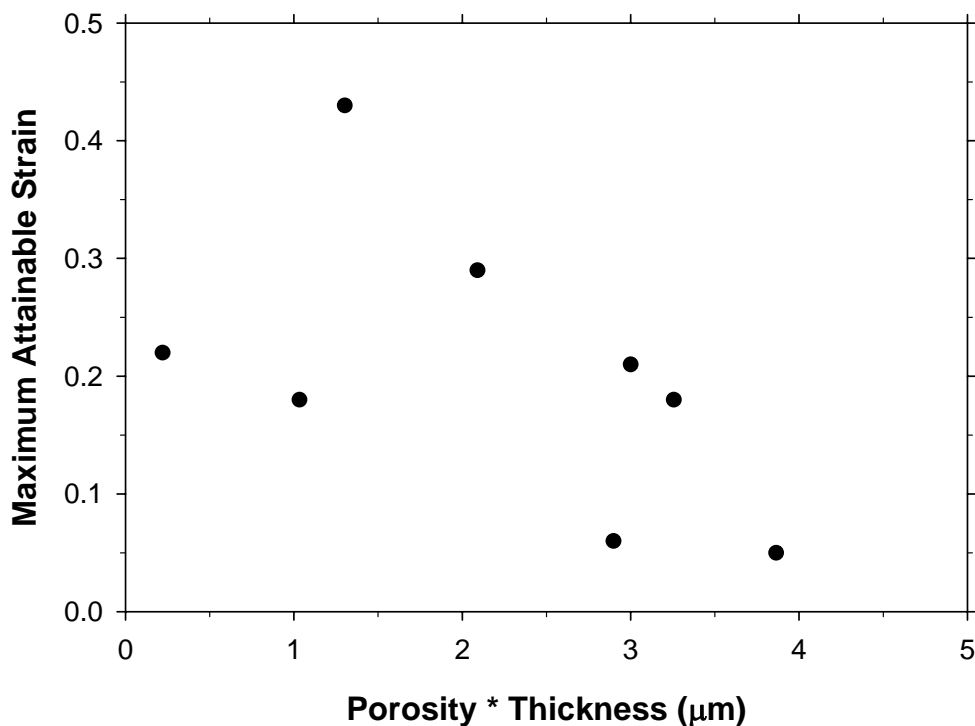


Figure 3.10 Maximum attainable strain shown as a function of thickness divided by porosity for each membrane

SEM micrographs were taken of all samples, and these micrographs were analyzed using the digital image analysis technique discussed in the previous section.

0.2 μm PET membranes were stretched to a total strain of 6% at 160°C and 0.025 cm/s, causing a 3.6% increase in pore area. This was within the experimental error, so no significant change to surface characteristics was observed. The PET membranes with pore size 0.4 μm were stretched to a maximum strain of 5% at 160°C and a strain rate of 0.025 cm/s. The results of this stretch were that area decreased by 6% and aspect ratio increased by 5%, but once again these values were within experimental error, so no significant change to pore characteristics was observed. PET membranes with 0.8 μm pore sizes were stretched 15% at 160°C and 0.025 cm/s before breaking, corresponding to a 43% increase in area and aspect ratio.

PET membranes with pore sizes of 0.6 μm were stretched to a maximum strain of 29% at 160°C and 0.25 cm/s, which corresponds to a 102% increase in aspect ratio and a

39% increase in area. Figure 3.11 shows a picture of (a) a non-stretched membrane, and (b) a 29% stretched sample. Intermediate stretches of 14 and 26% were also obtained and analyzed. Table 3.3 shows the resulting change (relative to the non-stretched membrane) in pore area, major axis, minor axis, and aspect ratio for these membranes. Shown in Figure 3.12 are the aspect ratio–strain and area–strain relationships for the 0.6 μm PET membranes. Aspect ratio is proportional to strain up to the point of breaking, as is major axis. Minor axis data was scattered, but showed a decreases of small magnitude.

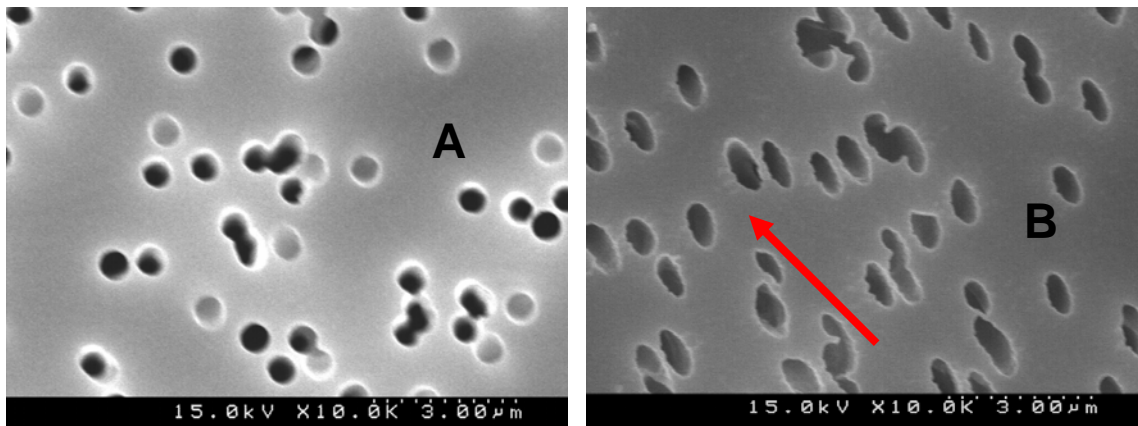


Figure 3.11 SEM of 0.6 μm PET membrane shown non-stretched (A) and 29% stretched (B) at 160°C and 0.25 cm/s. Arrow indicates direction of stretching

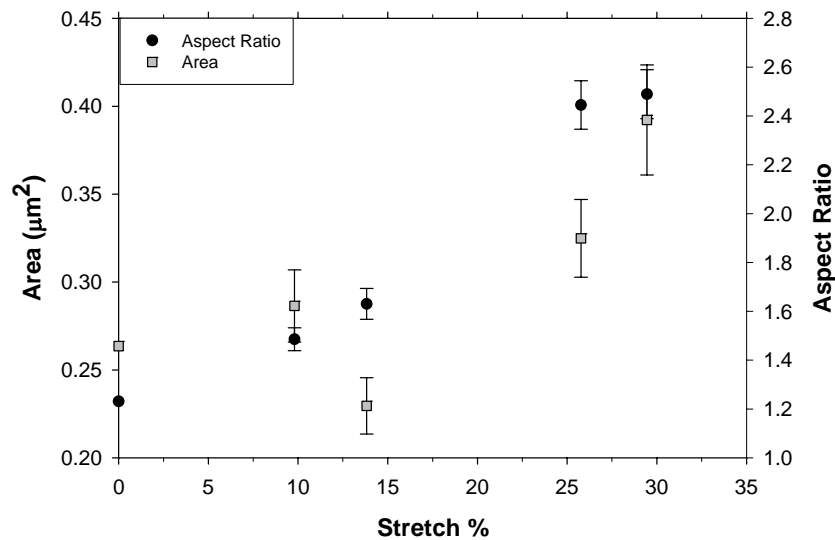


Figure 3.12: Area and aspect ratio shown as a function of strain for PET 0.6 μm membrane

Table 3.3
Change in pore characteristics upon stretching for various membrane pore sizes at various strains

Strain	Area	Major Axis	Minor Axis	Aspect Ratio	Porosity
% Change					
0.6 μm PET					
14%	13% \pm 7%	12% \pm 4%	-17% \pm 3%	32% \pm 4%	7% \pm 28%
29%	49% \pm 8%	66% \pm 4%	-15% \pm 4%	102% \pm 4%	56% \pm 17%
0.8 μm PET					
15%	9% \pm 18%	24% \pm 4%	-10% \pm 3%	43% \pm 4%	10% \pm 7%
1 μm PET					
11%	31% \pm 5%	55% \pm 4%	-14% \pm 1%	78% \pm 2%	50% \pm 9%
21%	56% \pm 4%	49% \pm 1%	-4% \pm 2%	44% \pm 3%	100% \pm 14%
2 μm PET					
12%	43% \pm 8%	37% \pm 3%	1% \pm 3%	32% \pm 3%	40% \pm 20%
24%	34% \pm 6%	49% \pm 3%	-11% \pm 3%	71% \pm 3%	16% \pm 11%
32%	77% \pm 10%	89% \pm 4%	-3% \pm 3%	100% \pm 4%	60% \pm 37%
3 μm PET					
13%	13% \pm 8%	18% \pm 5%	-7% \pm 3%	29% \pm 4%	11% \pm 16%
21%	23% \pm 9%	32% \pm 4%	-5% \pm 4%	44% \pm 4%	19% \pm 17%

PET membranes with pore size 1 μm were stretched up to a maximum of 22% at 140°C at a strain rate of 0.25 cm/s before breaking. Table 3.3 shows the resulting pore characteristics of some of the stretches obtained for this sample. Figure 3.13 shows a picture of (a) a non-stretched and (b) 22% stretched membrane. The relationships between aspect ratio and strain and area and strain are shown in Figure 3.14. Aspect ratio and area data are scattered, but both increase with strain. Major and minor axis data were also scattered, as was the porosity data, but in general, the same trends are evident for the 1 μm PET membrane as for the 0.6 μm PET membrane or the 2 μm membrane discussed above.

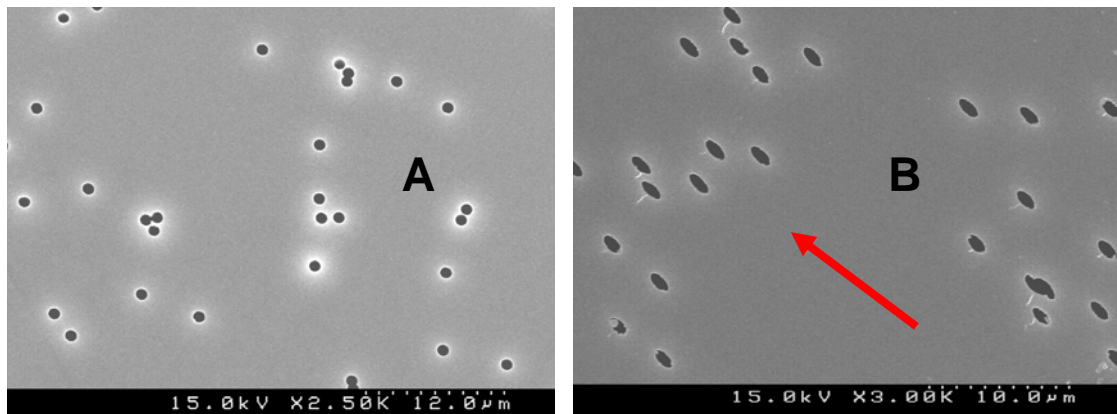


Figure 3.13 SEM of 1 μm PET membrane shown non-stretched (A) and 22% stretch (B) at 160°C and 0.25 cm/s. Arrow indicates direction of stretching

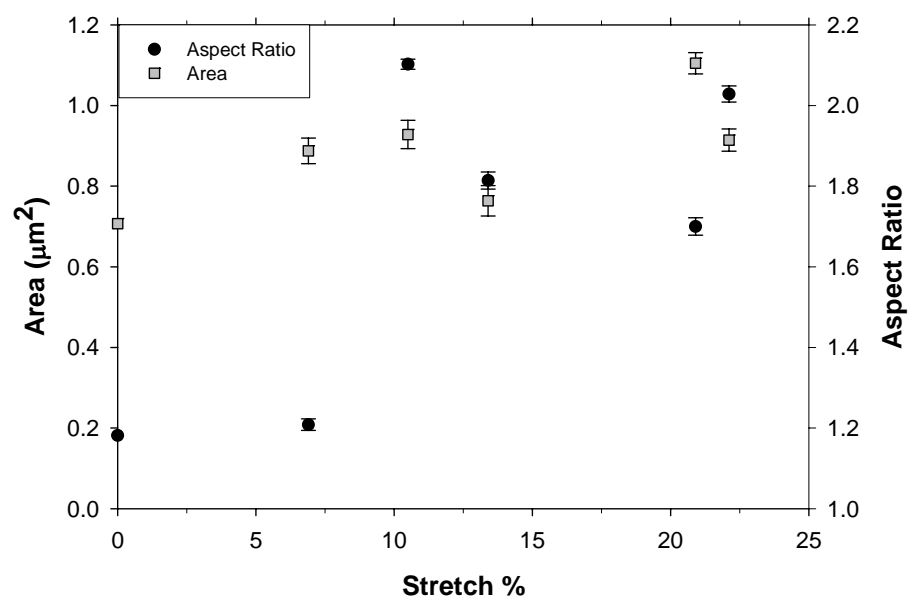


Figure 3.14: Area and aspect ratio shown as a function of strain for 1 μm PET membrane

The 3 μm PET samples were stretched up to 21% at 160°C and 0.25 cm/s before breaking. Table 3.3 gives a summary of the results of this stretch and other intermediate stretches for this sample. Figure 3.15 gives the relationship between strain and both aspect ratio and area. As for the membranes above, aspect ratio and area are shown to increase with strain. The same is true for major axis and porosity.

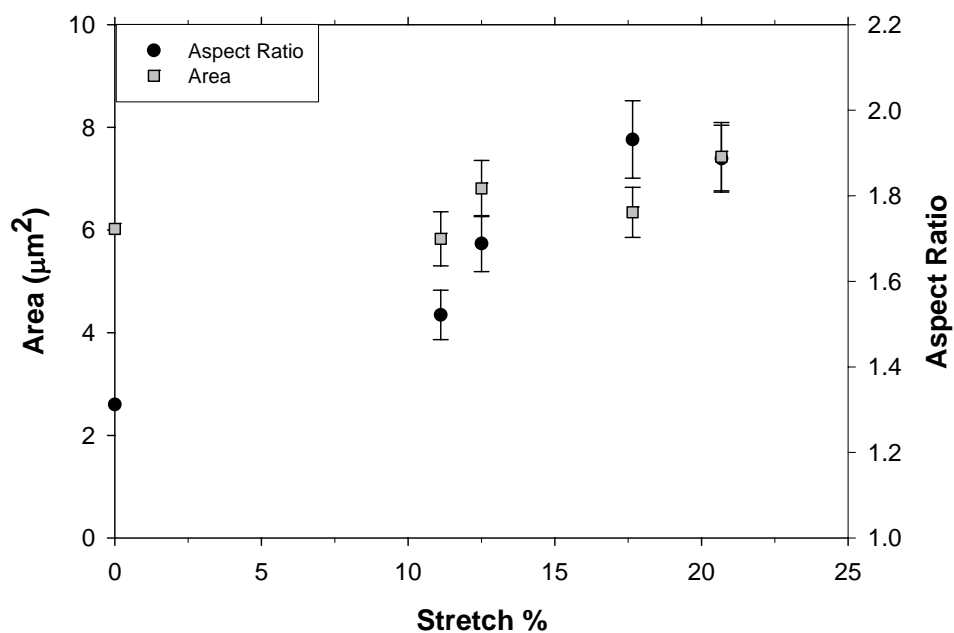


Figure 3.15: Area and aspect ratio shown as a function of strain for 3 μm PET membrane

The 10 μm PET samples were stretched up to 18% at 100°C and 0.025 cm/s, which resulted in a 69% increase in area and a 53% increase in aspect ratio.

The results presented in Table 3.3 and Figures 3.11 to 3.15 indicate that in general stretching PET membranes decreases the minor axis, increases the major axis, increases the aspect ratio, and increases the area and porosity. Figure 3.16 demonstrates that when all of the available data for all of the T-E membranes is combined, the aspect ratio is proportional to overall strain, albeit with some scatter. Thickness was also measured for all of the above samples, but similar to the 2 μm PET discussed in detail, no apparent change in thickness was evident upon stretching. Stretching has been shown to change surface characteristically, significantly in most cases. The change in permeation characteristics due to these changes is characterized in the next chapter.

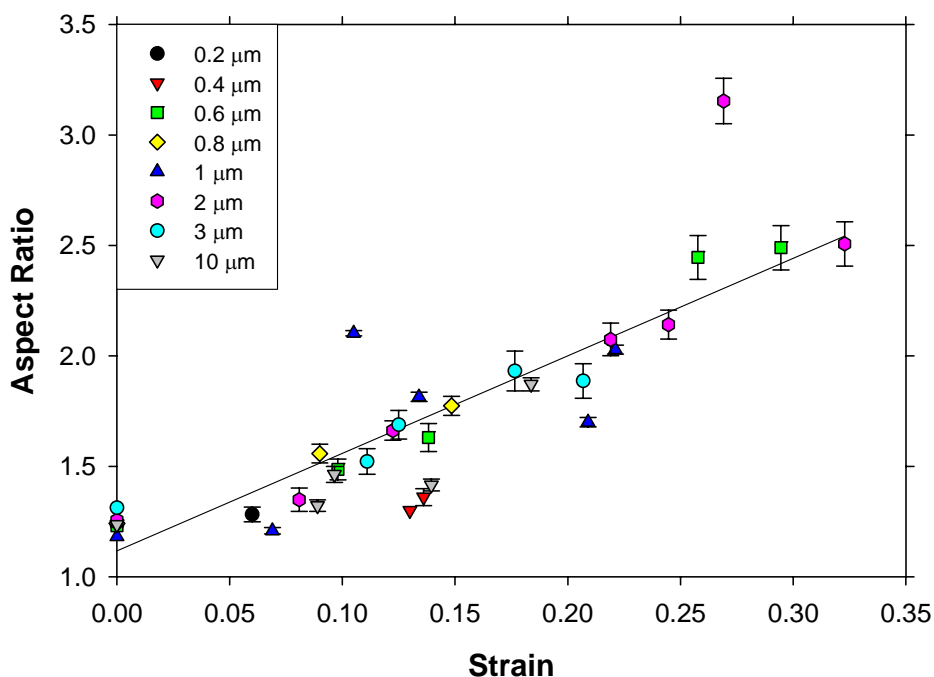


Figure 3.16 Effect of strain on aspect ratio for T-E membranes of all pore sizes at various conditions

3.2.2 Rebound Study

Another parameter measured was the rebound of the membrane, or the amount by which the membrane returned to its original state after stretching. All samples exhibited some rebound, but there are several factors that are expected to affect this parameter, such as temperature, strain, strain rate, and the temperature to which the sample was cooled. Annealing time was not varied in this study, as discussed in the “Materials and Methods” chapter. It was evident from studying the relaxation behavior of the polymer, which is discussed in detail in the “Modeling Results” chapter, that most of the relaxation happens in the first few minutes after stretching. One experiment was performed in which the sample was not annealed at all, and significant rebound was observed. Because the goal was to minimize the rebound in the sample, a standard protocol was defined for the above experiments.

In order to study the rebound effect and the affect of annealing, a 2nd order surface response design was employed, similar to that of the 2 μ m PET membranes studied above, in which temperatures of 80, 100, 120, and 160°C, rates of 0.1, 0.55, and 1 cm/s, and strains of 10, 25, and 40% were used. Additionally, cooling was allowed to vary from no cooling at all, cooling to the glass transition of approximately 75°C, and cooling to room temperature. The same batch of 2 μ m PET membranes was used for this study as for the study described previously. Once again, some of the experiments suggested by JMP were not physically possible, so some experiments were omitted and others were adjusted to make the matrix reasonable. The set of experiments performed, as well as the results, are shown in Table 3.4.

Table 3.4:
Experimental design and results for rebound study

Strain (%)	Temperature (°C)	Strain Rate cm/s	Cooling Temperature (°C)	Rebound (%)
7.57	120	0.55	75	26.55
9.60	80	0.1	25	22.50
9.96	160	1.0	no cooling	27.70
10.01	160	0.1	no cooling	10.49
10.03	80	1.0	no cooling	8.08
10.03	120	0.55	75	1.69
14.97	80	0.1	25	14.30
15.01	100	1.0	no cooling	10.66
15.04	80	0.55	75	7.45
24.99	120	0.55	no cooling	41.90
24.99	120	0.55	25	2.04
25.01	160	0.55	75	5.92
25.05	120	0.55	75	5.75
34.96	120	0.55	no cooling	33.90
35.02	160	0.1	25	2.57
40.03	160	1.0	no cooling	44.14
40.03	160	1.0	25	3.70
40.41	160	0.1	no cooling	32.24

The results of these experiments showed that, unlike the pore characteristics measured above, strain has little or no effect on rebound. Temperature and rate had a more noticeable effect. Stretches done at cooler temperatures exhibited more rebound than those done at higher temperatures, and stretches performed at higher rates exhibited more rebound than those done at lower rates. Cooler temperature and higher strain rates hinder the ability of the polymer to rearrange and relax, which explains why the samples stretched at cooler temperatures and higher rates exhibited more rebound. The most noticeable effect was from the cooling of the membranes. Membranes allowed to cool to room temperature exhibited the least rebound, usually just a few percent, whereas those samples not cooled at all exhibited rebounds up to 44%. Samples allowed to cool to 75°C exhibited slightly more rebound than those allowed to cool to room temperature, but still much less rebound than those not allowed to cool at all. Once the membrane reaches its glass transition temperature, it is not going to rearrange significantly enough to cause more measurable rebound as it cools further. Otherwise stated, the time-scale of rearrangement has been shifted significantly enough once the membrane has reached its glass transition that relaxation occurs slowly, and little measurable rebound was observed. Membranes that are released at high temperature, however, can relax quickly because of their relative location on the time-temperature shift scale and will do so. To further study this effect, an experiment was done with a dense film at 120°C and 0.55 cm/s in which the film was stretched 40.4% and not allowed to cool while still in the clamps. This sample rebounded 23.5%, which is less than the rebound of the same experiment with the membrane, which rebounded 33.9%.

CHAPTER 4: PERMEATION EXPERIMENTAL RESULTS

4.1 PERMEATION FLUX RESULTS

4.1.1 T-E Membranes: Pure Water Results

Pure water flux studies were performed on the 0.6 μm pore size PET sample with 0 and 26% strain. Results from these studies are given in Figure 4.1, where the two sets of data at 26% strain represent two samples cut from the same stretched membrane sheet. These results show excellent repeatability between samples, and they also show that stretching significantly increases permeability. Pure water flux increased by an average of 70%.

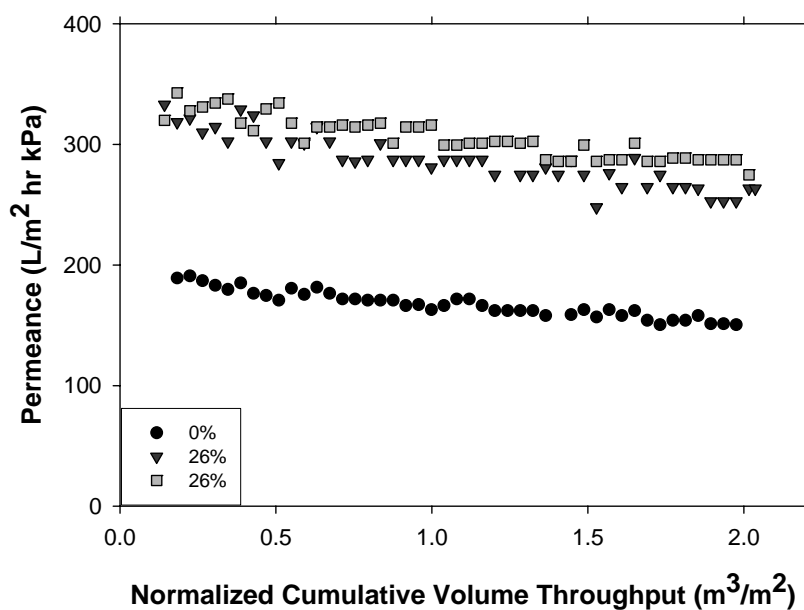


Figure 4.1 Effect of strain on permeance: Pure Water through 0.6 μm PET membranes

Pure water flux studies were also performed on membranes of pore size 1, 2, 3, and 10 μm . Results for the 1 μm membrane showed less noticeable improvement than the 0.6 μm membrane shown in Figure 4.2, and significantly less repeatability. The 2 μm membrane also showed some improvement in pure water flux upon stretching, shown in Figure 4.3, but the improvement was difficult to quantify because the data was somewhat scattered, although repeatability was evident. Results from the 3 and 10 μm membranes, shown in Figures 4.4 and 4.5 respectively, showed no measurable improvement upon stretching, giving similar flux values for both stretched and non-stretched samples.

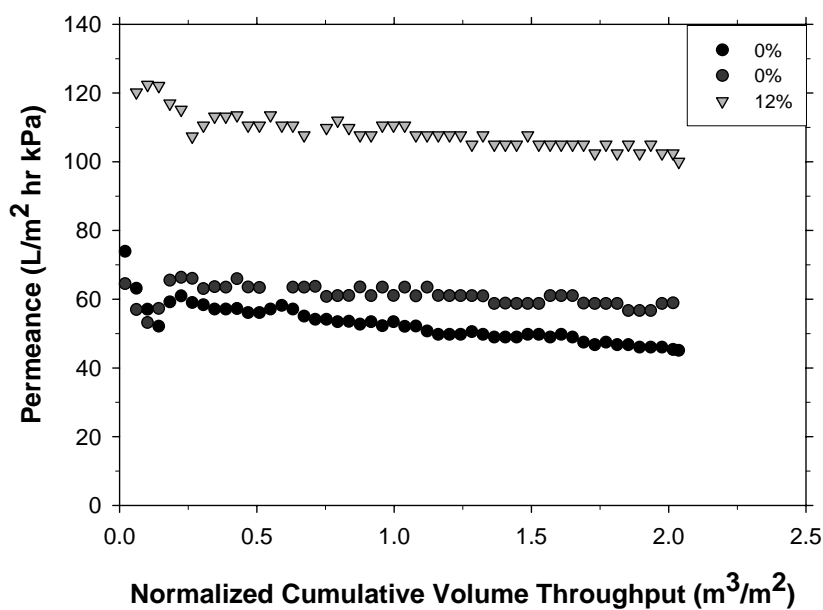


Figure 4.2 Effect of strain on permeance: pure water on 1 μm PET membrane

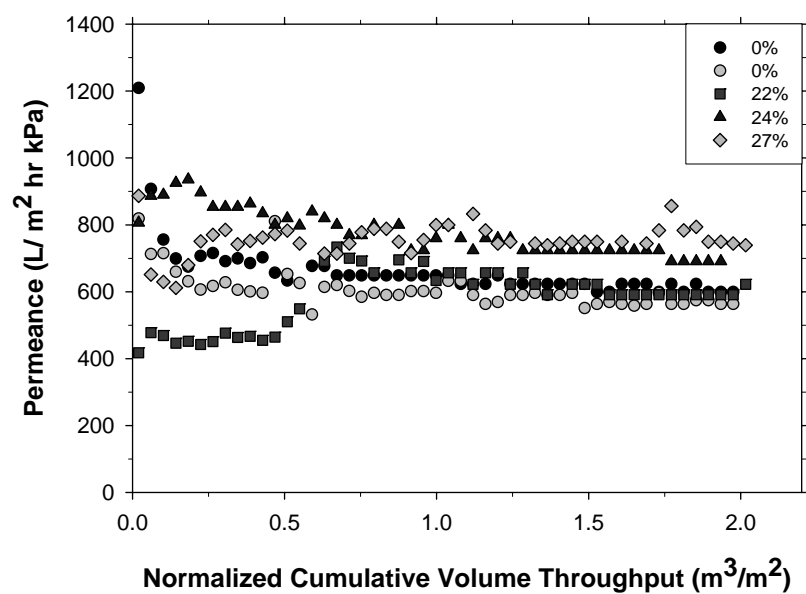


Figure 4.3 Effect of strain on permeance: pure water on 2 µm PET membrane

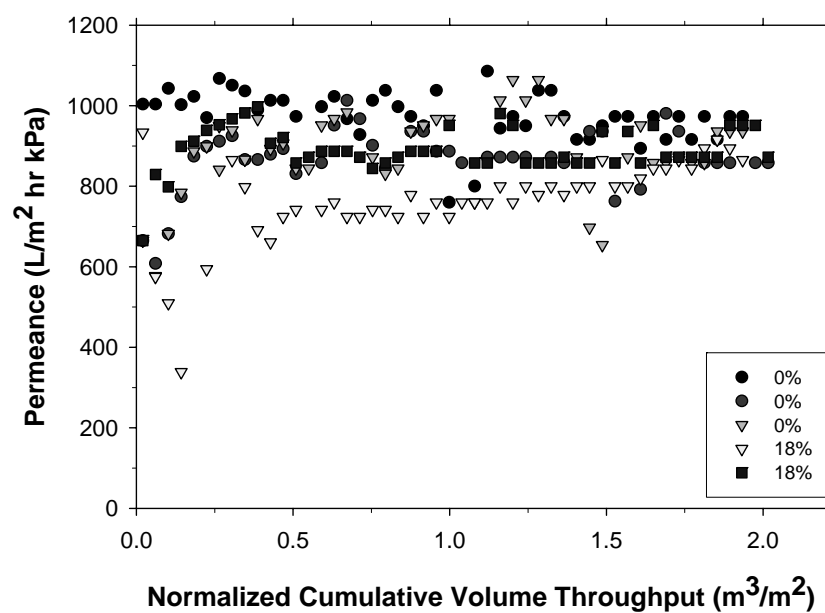


Figure 4.4 Effect of strain on permeance: pure water on 3 µm PET membrane

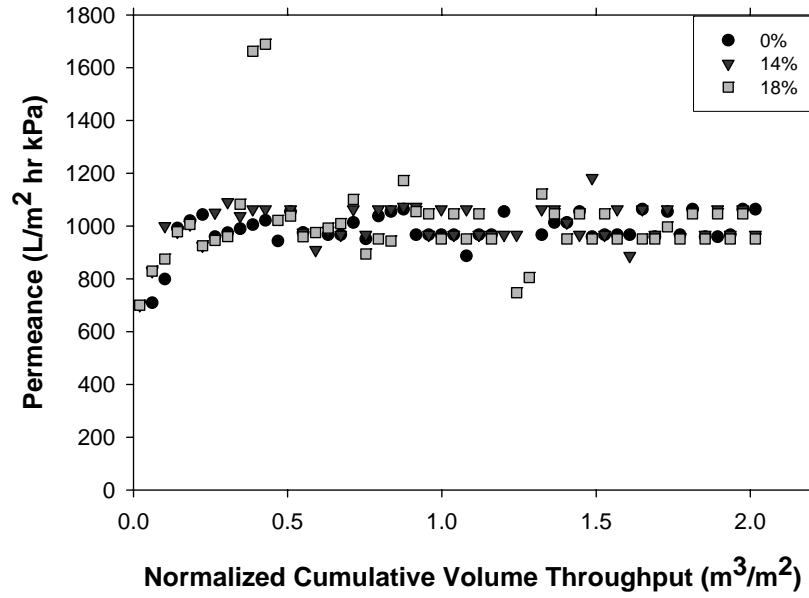


Figure 4.5 Effect of strain on permeance: pure water on 10 µm PET membrane

The ability to change the flux by stretching the membrane lessens as the pore size increases. According to Equation 4.1, the flux, J , should be proportional to the change in pressure across the membrane, ΔP , and the intrinsic permeability, k , and it should be inversely proportional to membrane thickness, δ_m , and permeated viscosity, μ .

$$J = k \cdot \frac{\Delta P}{\delta_m \cdot \mu} \quad (4.1)$$

The intrinsic permeability is defined in Equation 4.2 as

$$k = \frac{A_{\text{pore}} \cdot r_{\text{pore}}^2}{8 \cdot A_m \cdot \xi} \quad (4.2)$$

Where A_{pore} is the surface area of the membrane that is porous, A_m is the total membrane area, r_{pore} is the radius of the pore, and ξ is the tortuosity of the membrane. The viscosity is not expected to change from experiment to experiment. Presumably with the track-etched membrane, tortuosity is not an issue, so equations 1 and 2 can be combined and rewritten as Equation 4.3

$$\frac{J \cdot \delta_m}{k \cdot \Delta P} = \frac{1}{8 \cdot \xi \cdot \mu} \quad (4.3)$$

such that the known information can be used to determine the constant on the right hand side, which is expected to be the same for all the membranes tested. Table 4.1 shows this information for both stretched and non-stretched membranes. The 0.6, 1 and 2 μm PET membranes are in good agreement with this theory, both stretched and non-stretched, but the 3 and 10 μm membranes deviate. The 10 μm membrane has a significantly higher pore size with a smaller thickness. Equation 4.4 gives the entrance length for a cylinder, which is the length of pore required to achieve fully developed flow.

$$\frac{L_v}{D} = 1.18 + 0.112 \cdot N_{Re} \quad (4.4)$$

In Equation 4.4, L_v is the entrance length, D is the pore diameter, and N_{Re} is the Reynolds number. For the 10 μm membrane, the entrance length is 13.5 μm , which is just greater than the membrane thickness, 13 μm . Fully developed flow is not achieved in this membrane, which indicates that the model for intrinsic permeability is not applicable in this case. For all other membranes, the entrance length is much shorter than the membrane thickness, so fully developed flow is achieved and the model above can be applied. It is also interesting to note that, even with the smaller membrane sizes that result in a similar constant, the constant decreases as the pore size gets larger. This deviation from the theory is the reason that change in pure water flux is not evident upon stretching for the larger pore sizes. For these sizes, flux is not solely a function of membrane thickness, change in pressure, and k .

Table 4.1
Pure water flux calculations to test agreement between membranes of intrinsic permeability

Membrane	Permeance $J/\Delta P$ ($L/m^2 \text{ hr kPa}$)	Porosity (A_{pore}/A_m)	Equivalent r_{pore} $2r_{\text{hyd}}$	Thickness σ_m (μm)	Reynolds number	L_v (μm)	Ratio $J/\Delta P * \sigma_m / k$
Part A: Non-stretched							
0.6	180	0.095	0.29	22	0.03	0.71	4.9×10^5
1	60	0.010	0.47	22	0.22	1.21	5.9×10^5
2	600	0.062	0.82	21	0.18	2.40	3.0×10^5
3	900	0.015	1.35	20	0.18	3.60	6.6×10^4
10	1000	0.080	4.52	13	1.29	13.5	8.0×10^3
Part B: Stretched							
0.6	300	0.133	0.28	22	0.04	0.71	6.2×10^5
1	100	0.015	0.49	22	0.25	1.20	6.0×10^5
2	700	0.072	0.87	21	0.19	2.40	2.7×10^5
3	900	0.175	1.37	20	0.16	3.59	5.5×10^4
10	1000	0.086	5.46	13	1.45	13.42	5.1×10^3

Pores were assumed to be perpendicular to membrane surface in this analysis, such that pore length is equal to membrane thickness. However, as evidenced by the SEM in Figure 3.1, a large fraction of pores are not perpendicular but lie at an angle to the membrane surface. Pores were also assumed to be circular and of uniform size, but this is also not true. An adjustment was made to the above analysis to account for overlapping pores in the 3 μm sample, since this sample had the greatest number of overlapping pores due to its high pore density, to determine the effect of these larger pores on the value of the ratio reported in Table 4.1. Another adjustment was made to account for angled pores. The value of the reported ratio did not change significantly in either case, decreasing about 10% from the overlapping pore adjustment and decreasing less than 3% for the angled pore study. The assumptions made in this analysis of circular and uniform pores and uniform pore length were not valid, but did not affect the results.

4.1.2 Min-u-sil Particle Challenge Studies

Figure 4.6 shows the results from particle challenge experiments performed on 0 and 12% stretched 1 μm PET membranes. Approximately 10% of the particles in Min-u-sil 5 are smaller than 1 μm in diameter, as can be determined from Figure 2.6. Figure 4.6 again demonstrates the high repeatability obtained between samples and experiments. The results show that stretching increases permeance and decreases flux decline for feed suspensions containing Min-u-sil particles. The shape of the curve for the stretched samples is less steep than that of the non-stretched sample, demonstrating a decrease in flux decline. Flux for the stretched sample is 35% higher after 200 mL of throughput, and 87% higher after 600 mL of throughput. This increase is due to the increase in membrane porosity caused by stretching [75].

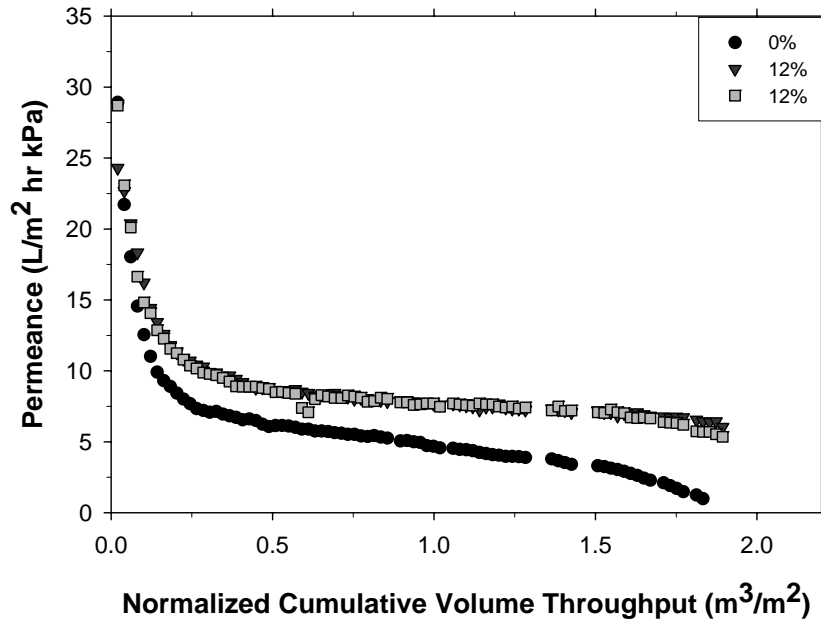


Figure 4.6: Effect of strain on permeance: Min-u-sil 5 on 1 μm PET membrane

The data were further analyzed using a Hermia analysis, which characterizes fouling for pressure driven flow through a membrane. The Hermia analysis is completed by using Equation 4.6 to linearize flux data.

$$\frac{d^2t}{dV} = k \left(\frac{dt}{dV} \right)^n \quad (4.6)$$

In Equation 4.6, V represents volume, t represents time, and k is a constant. If flux data is linearized by setting n equal to zero and plotting time/volume versus volume then the filtration is controlled by a cake building up on the surface according to Hermia analysis. For n equal to 0, Equation 4.6 becomes Equation 4.7.

$$\frac{d^2t}{dV_{cum}^2} = K \quad (4.7)$$

Integrating this expression twice gives Equation 4.8:

$$\frac{t}{V_{cum}} = C_1 KV + C_2 \quad (4.8)$$

in which C_1 and C_2 are constants. If a plot of $\frac{t}{V_{cum}}$ versus V yields a straight line, then the assumption that n is zero is valid and the filtration is cake controlled. The slope of that line is proportional to the resistance.

$$\frac{t}{V_{cum}} = \frac{\mu R_{cake}}{A_m \Delta P} + \frac{\mu R_{cake} \phi_b}{2 A_m \Delta P \phi_{cake}} V_{cum} \quad (4.9)$$

Equation 4.9 shows the values of the constants C_1 and C_2 from Equation 4.8. The slope of the line is proportional to R_{cake} , which is the resistance of the cake layer. The slope is also proportional to ϕ_b and ϕ_{cake} , which are the volume fraction of particles, and μ is the solution viscosity. Figure 4.7 shows this plot for the 1 μ m PET with 10 mg/L Min-u-sil 5 suspension feed. The stretched membrane shows lower resistance to flux (that is, lower slope). The Hermia analysis was only applied to the linear portion of the plots, which correspond to constant pressure operation; the fact that the pressure in these experiments varied at the beginning of the experiments caused the curvature in Figure 4.7. The experiments for the other PET membranes required constant adjustment of the pressure; thus, no Hermia analysis is presented for the other PET Membranes.

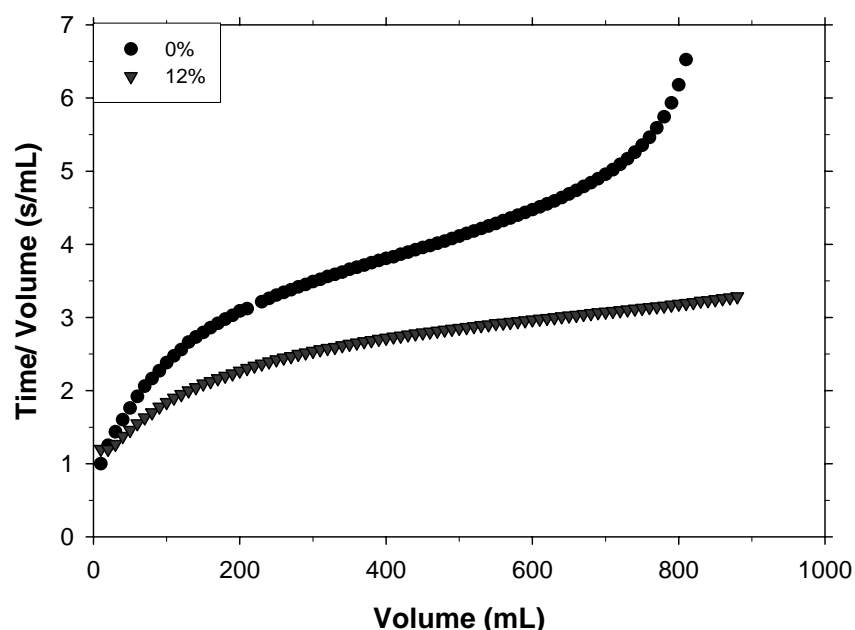


Figure 4.7 Hermia analysis for 1 μm PET: Min-u-sil 5 fed at 10 mg/L

Results from the experiments with 2 and 3 μm PET membranes are shown in Figure 4.8. In all cases, results for the first 0.1 m^3/m^2 of volume throughput were rather scattered, but the overall trend was for a rapid flux decline over approximately the first 0.3 m^3/m^2 of volume throughput and a more gradual decline thereafter. For the 2 μm membranes, shown in Figure 4.8 (A), stretching increased the flux by up to 35% and reduced the flux decline. Approximately 57% by surface area distribution of the particles in Min-u-sil 5 are smaller than 2 μm . For the 3 μm membranes, stretching led (at best) to only a marginal improvement in the permeability.

The 3 μm PET samples did not show a significant increase in permeability with stretching, as shown in Figure 4.8 (B). Approximately 88% by surface area distribution of the particles in Min-u-sil 5 are smaller than 3 μm . Comparing Figure 4.8 (A) and (B), the fluxes are similar, with the 3 μm PET membrane flux starting out higher than that of the 2 μm PET membrane, and both are significantly higher than that of the 1 μm membrane shown in Figure 6, which has a porosity of about 1%. The 2 μm membrane has a porosity of about 6%, and the 3 μm membrane has a porosity of about 15%. The 3

μm membrane exhibits significantly less flux decline than the 2 μm membrane due to its higher porosity.

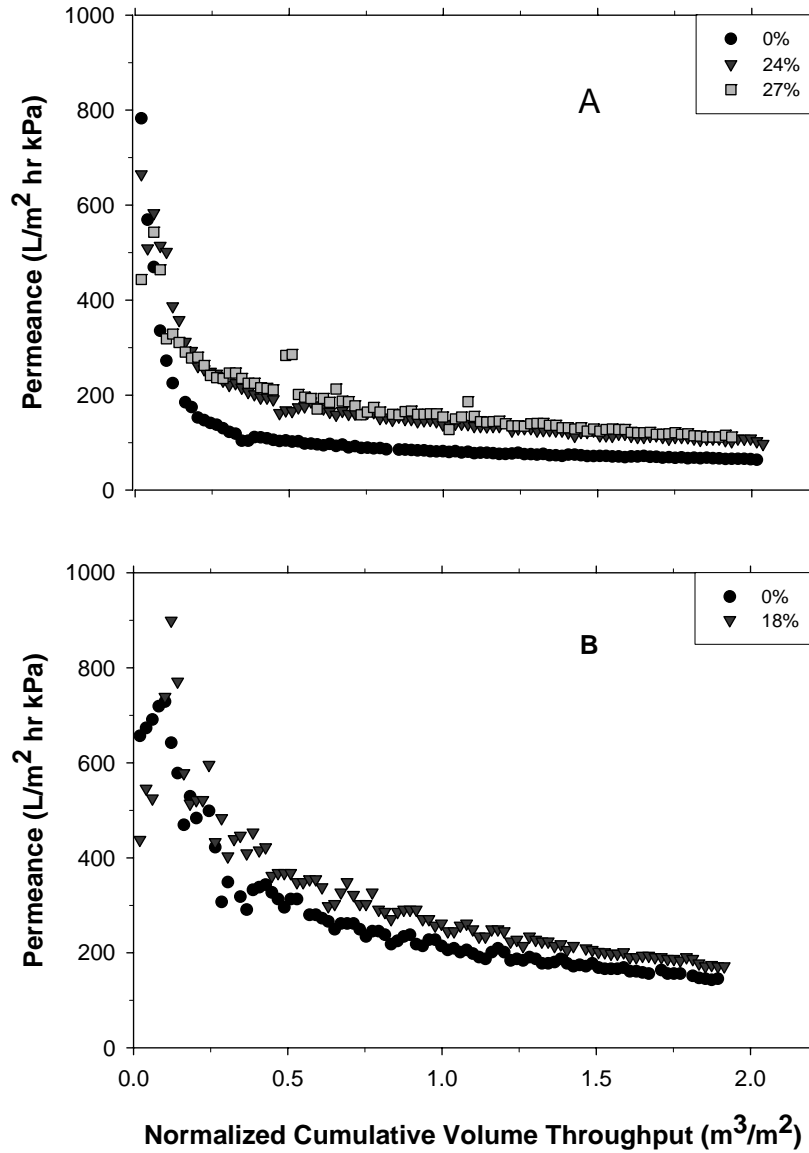


Figure 4.8 Effect of strain on permeance: A) Min-u-sil 5 on 2 μm PET membrane. B) Min-u-sil 5 on 3 μm PET membrane

Min-u-sil 30 was used for the 10 μm PET samples. The suspension concentration was 10 mg/L, and experiments were performed in the same way as the previously described Min-u-sil 5 experiments. There was some increase in permeability for samples stretched 14 and 18%. These samples had a very high flux, making volume readings difficult, which caused some scatter for the first 0.41 m^3/m^2 of the experiment, as shown in Figure 4.9.

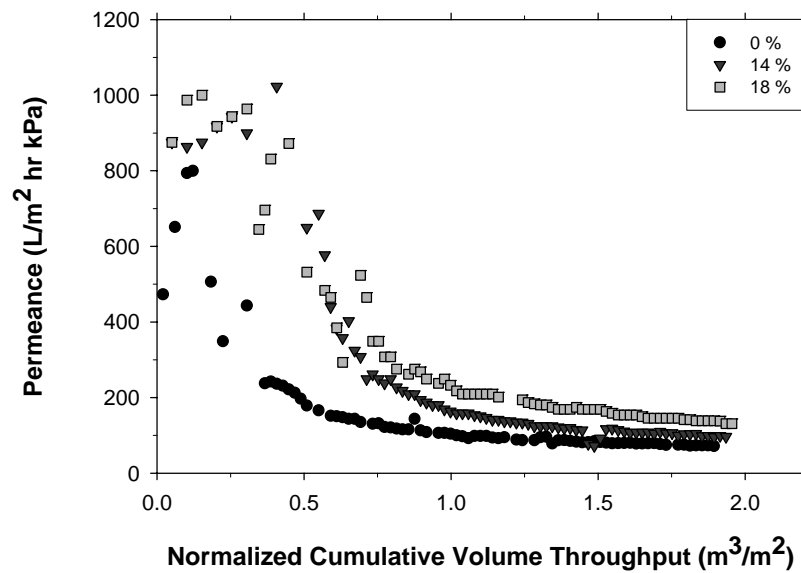


Figure 4.9 Effect of strain on permeance: Min-u-sil 30 on 10 μm PET membrane

In summary, the challenge studies with irregular shaped particle suspensions fed to track-etched PET membranes indicate that stretching has the potential to increase flux and reduce flux decline. Decreased flux decline could have positive financial impact on membrane applications by decreasing the frequency of stopping the process for back-flushing to clean the membranes. While further work is needed to quantify the effect of stretching on flux decline and to see if the frequency of back-flushing can be reduced, the results are encouraging.

4.1.3 Spherical Beads Challenge Studies

The studies with Min-u-sil, with its broad particle size distribution, provided a realistic assessment of the behavior of the membranes and the effects of uniaxial stretching for real suspensions, which are inevitably heterodisperse. However, from a fundamental point of view, it is more instructive to apply monodisperse suspensions to the membranes, using spheres with sizes that are close to those of the (non-stretched) pores of the PET membranes. Such tests should give the most sensitive and direct indication of the effects of stretching on particle and fluid behavior, because they eliminate the effects of shape irregularity in the particles.

The results for a few such experiments are shown in Figure 4.10. Both the 0.6 μm membranes with a feed suspension of 0.652 μm diameter spherical particles and the 2 μm membranes with 2.02 μm spherical particles exhibited a substantial improvement in the permeability by stretching. For the smaller pore size membrane shown in Figure 4.10 (A), the benefits diminished as the experiment proceeded, but some improvement remained throughout the experiment. Packing density on the surface of the membrane with spherical particles increases as pore size distribution decreases [76]. The particle size distribution of microspheres used in these experiments is very narrow, such that after a long period of time, regardless of the membrane underneath, the long term flux will be the same for both stretched and non-stretched membranes due to the dense packing on the surface. A similar trend can be seen for the larger pore size, shown in Figure 4.10 (B), but the improvement in permeability is still quite substantial, with the stretched

membranes having approximately three times the permeability of the non-stretched even at a cumulative throughput of $2 \text{ m}^3/\text{m}^2$, though the improvement is visibly diminishing. Such results, if realized in full-scale systems, could reduce the required membrane area substantially. Also, in real systems, back-flushing of the membranes could be done at much greater intervals for the stretched membranes than for the non-stretched membranes, thereby increasing the recovery of the system.

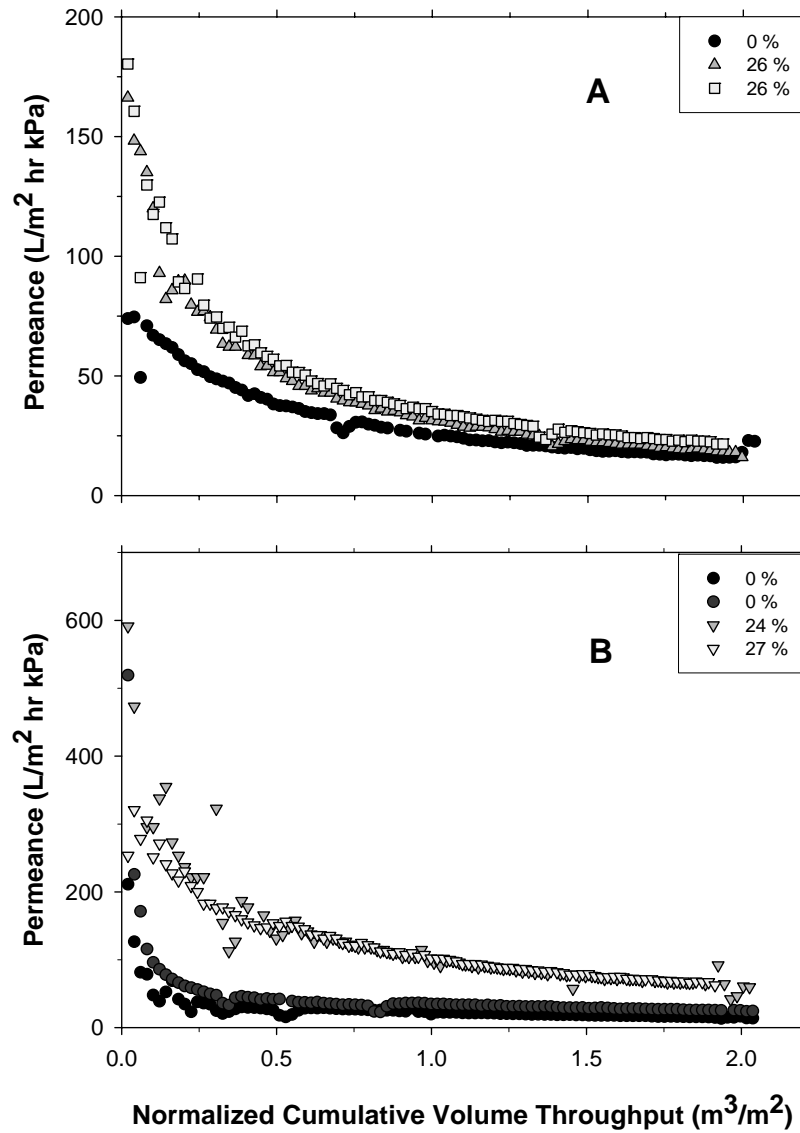


Figure 4.10 Effect of strain on permeance: A) $0.652 \text{ }\mu\text{m}$ microspheres on $0.6 \text{ }\mu\text{m}$ PET membrane. B) $2.02 \text{ }\mu\text{m}$ microspheres on $2 \text{ }\mu\text{m}$ PET membrane

4.2 PERMEATE ANALYSIS AND REJECTION RESULTS

4.2.1 Min-u-sil Particle Challenge Studies

Particle challenge experiments were performed using Min-u-sil 5 for 1 μm , 2 μm , and 3 μm track-etched membranes and using Min-u-sil 30 for 10 μm track-etched membranes. Samples were collected throughout each experiment so that the particle rejection capability of each membrane could be examined over time and compared for different volume throughputs. Samples were analyzed using the Coulter Counter by Leah Shimko [77], and the resulting data were used to plot the surface area distributions of the permeate.

Figure 4.11 demonstrates the removal of Min-u-sil 5 particles, starting at a feed concentration of 10 mg/L, for the 1, 2 and 3 μm PET membranes. As expected, the 1 μm PET membrane has the greatest removal, showing the fewest particles in the permeate. The 2 μm PET membrane removes less than the 1 μm PET membrane, but more than the 3 μm PET membrane, again as expected. These data indicate that the experimental techniques were executed carefully and results are trustworthy.

As the experiment progresses and a cake layer forms on the membrane surface, the amount of particles allowed through is expected to decrease. This is shown to be true in Figure 4.12, which shows the surface area distribution of particles in the permeate at several volume throughputs for an 18% stretched 3 μm PET membrane. As expected, fewer particles are present in the permeate as the experiment progresses, once again confirming the validity of the technique.

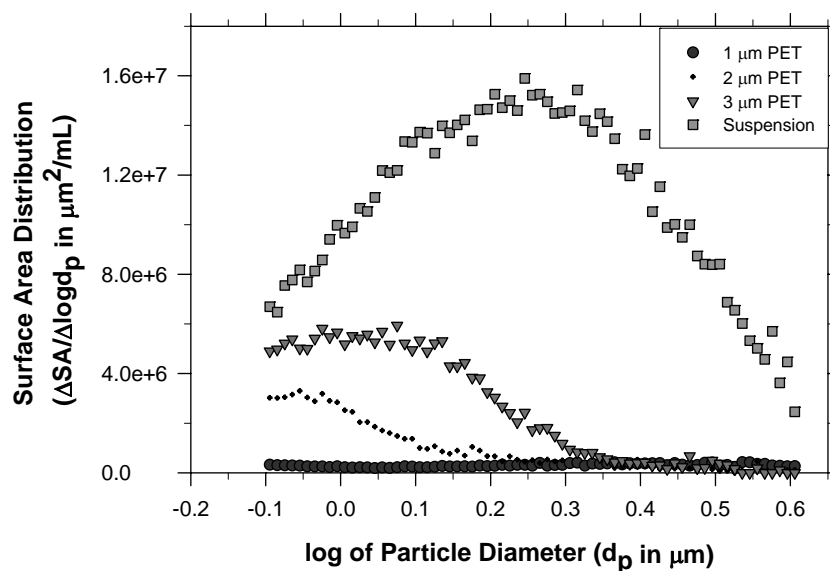


Figure 4.11 Surface Area distribution of min-u-sil particles in the permeate for stretched and non-stretched 1, 2, and 3 μm PET at $50 \text{ m}^3/\text{m}^2$ cumulative volume throughput

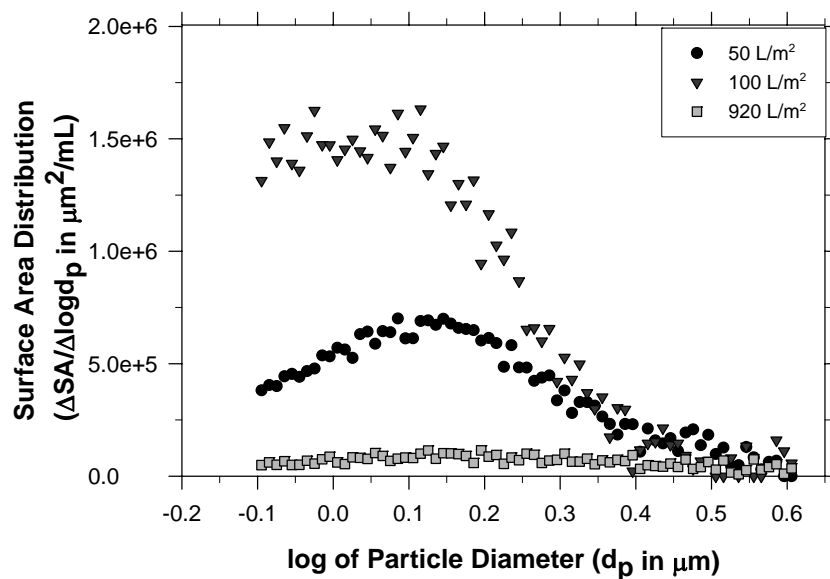


Figure 4.12 Surface area distribution of particles in the permeate at ascending normalized cumulative volume throughputs for non-stretched $3 \mu\text{m}$ PET

Experimental results for 1 μm PET membranes, presented in Figures 4.13, show that the membranes, stretched and non-stretched, achieve anywhere from 2 to 3 log removal of particles when compared with the feed suspension, and this removal generally improves over time. Figure 4.13 is a surface area distribution for both stretched and non-stretched 1 μm PET, and this graph indicates that stretching the membrane may (slightly) improve particle rejection. The results for different sets of samples for the non-stretched membranes do not compare well however, indicating the particle rejection data are not exactly repeatable. Therefore, the results should be regarded as preliminary and the experimental procedure may have to be improved to ensure the highest quality data; the Coulter Counter requires scrupulous care to ensure repeatability.

In addition to Coulter data, turbidity data was taken at each volume collected to determine the turbidity of the solution as a function of time over the course of the experiment. Permeate suspensions from stretched and non-stretched samples were compared to determine which membrane allowed more particles through and into the permeate. For the 1 μm PET membrane, turbidity is shown as a function of volume throughput in Figure 4.14. Turbidity is reported in Nephelometric Turbidity Units (NTU). The turbidimeter is not very sensitive to the low concentration of particles that were allowed through the 1 μm membrane. Only the first sample collected within the first 25 mL of the experiment shown any significant number of particles in the permeate. For this sample, it is clear that the non-stretched membrane allowed more particles through than the 12% stretched sample, the non-stretched sample having a higher turbidity reading. The minor axis of this sample decreased by 14%, indicating that a higher rejection would be expected. Readings throughout the rest of the experiment were near 0 and showed no difference between stretched and non-stretched samples.

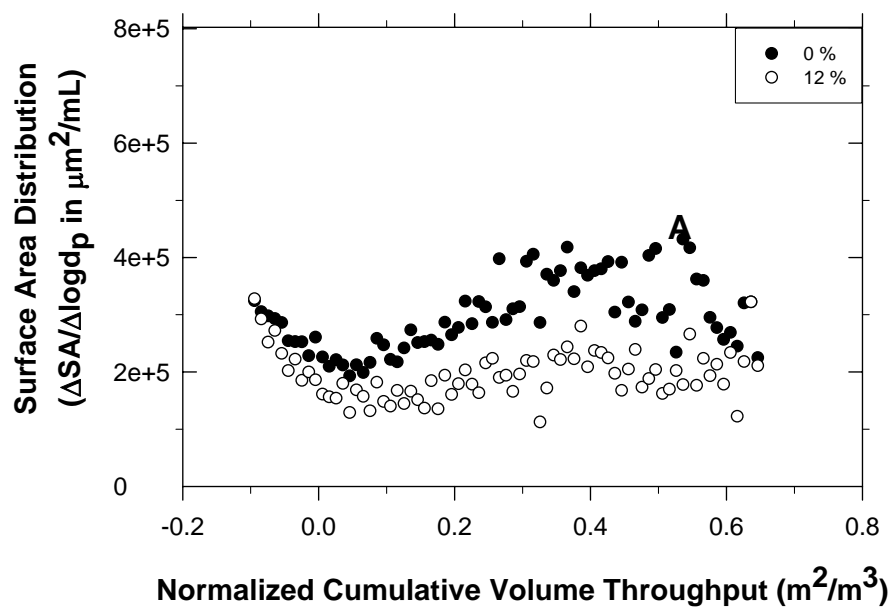


Figure 4.13: Surface area distribution of particles in the permeate for stretched and non-stretched 1 μm PET membrane

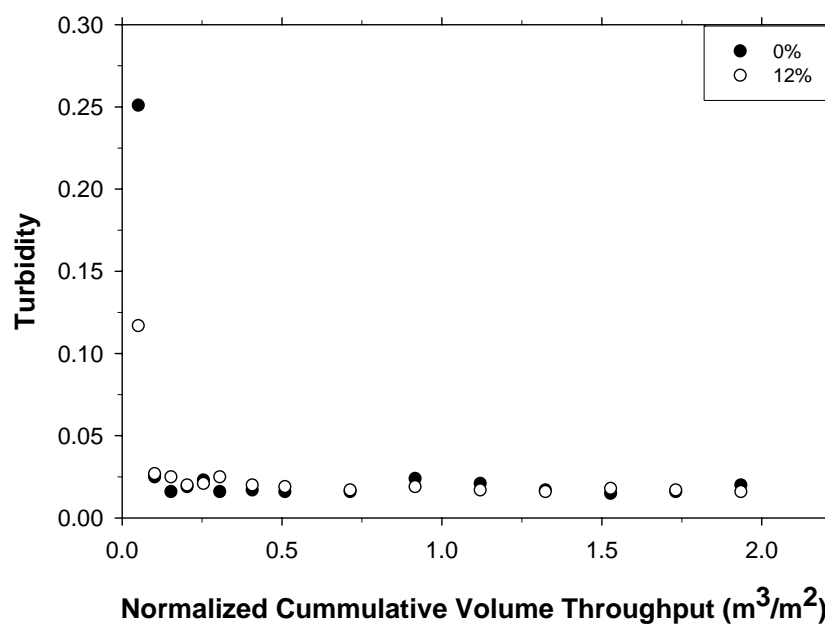


Figure 4.14 Turbidity results for permeate suspension concentration at various cumulative volume throughputs for 1 μm PET non-stretched and at 12% strain

Figure 4.15 shows some of the results for the Min-u-sil 5 particle challenges using 2 μm PET membranes. For particles smaller than 2 μm , the surface area distribution indicates that stretching the membranes does not result in significant improvements in particle rejection, although some difference between stretched and non-stretched is noticeable.

Coulter Counter analysis results for Min-u-sil 5 particle challenges using 3 μm PET membranes were encouraging. As shown in Figure 4.16, the 18% stretch improved rejection of particles smaller than the pore size, allowing fewer particle to pass into the permeate than their non-stretched counterparts. This shows that stretching can improve rejection.

These results were not repeatable at other volume throughputs. Table 4.2 presents some of these data; negative numbers in this table mean that the stretched membrane achieved better removal than the non-stretched membrane. The results from the membrane stretched 13% are virtually all positive, meaning that, after stretching, more particles passed through the membrane. The 18% stretch apparently is weak improved rejection of particles smaller than the pore size, while a 13% stretch appears to allow more small particles to pass through the membrane. According to these overall Min-u-sil 5 results, no vast improvement in particle rejection was achieved with the stretching of 3 μm membranes. As with the 2 μm membranes, counts of particles larger than the pore size were too small to be significant. Results were difficult to repeat, which is evident from the two sets of data for the 18% strain sample. Further study will be required to determine the effect of stretching on rejection of the 3 μm PET membrane.

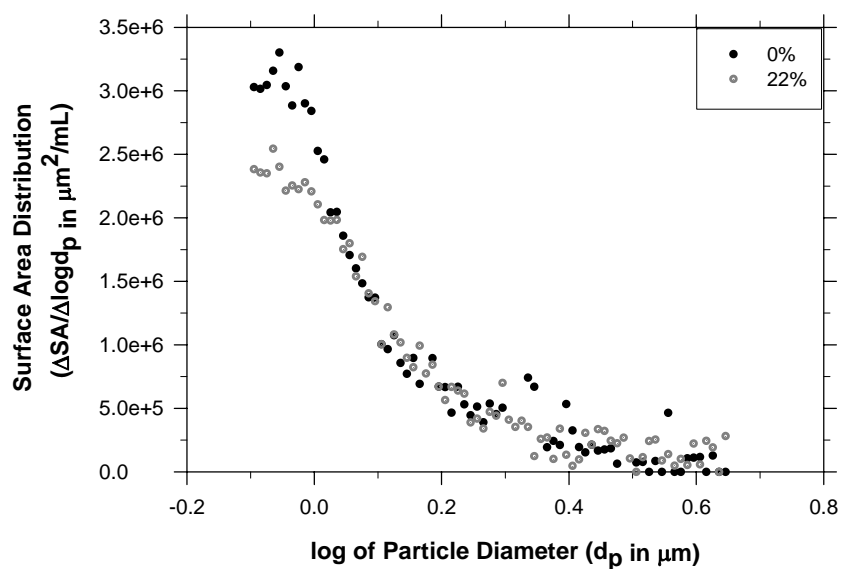


Figure 4.15 Surface area distribution of particles in the permeate for stretched and non-stretched 2 μm PET membrane

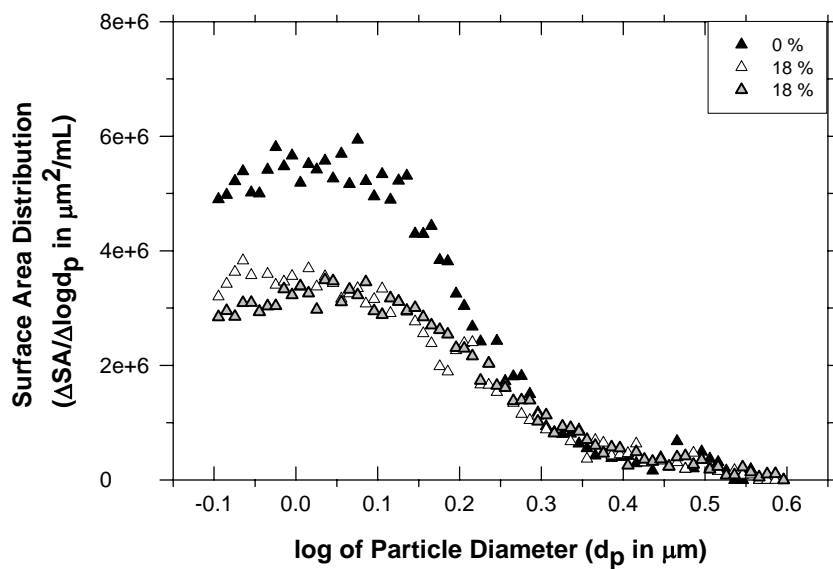


Figure 4.16 Surface area distribution of Min-u-sil 5 particles in the permeate for 3 μm PET membranes non-stretched and at 18% strain

Table 4.2
Change in number concentration of Min-u-sil 5 particles on 3 μm PET membrane
from non-stretched to membranes at 13 and 18% strain

Strain (%)	Normalized cumulative volume throughput (m^3/m^2)	20 channels 0.8 – 1.25 μm	20 channels 1.9 – 3 μm	20 channels 2.4 – 3.8 μm	20 channels 3.8 – 5.4 μm
13	50	-19%	193%	138%	70%
18	50	-63%	-40%	-90%	-100%
13	100	1063%	1459%	627%	20%
18	100	-75%	-66%	-84%	-100%
13	400	1030%	1064%	359%	-23%
18	400	85%	146%	101%	-100%

Turbidity results for the 3 μm PET membrane, shown in Figure 4.17, are similar to those of the 1 μm PET membrane in that they only show a discernable difference between membranes at the beginning of the experiment. For the first few readings, the permeate from the stretched samples have fewer particles than the permeate samples from the non-stretched experiment, demonstrating that the stretched membrane removed more particles. After the first few samples, the particle concentrations are too low for the turbidimeter to discern a difference between the samples, if a difference exists.

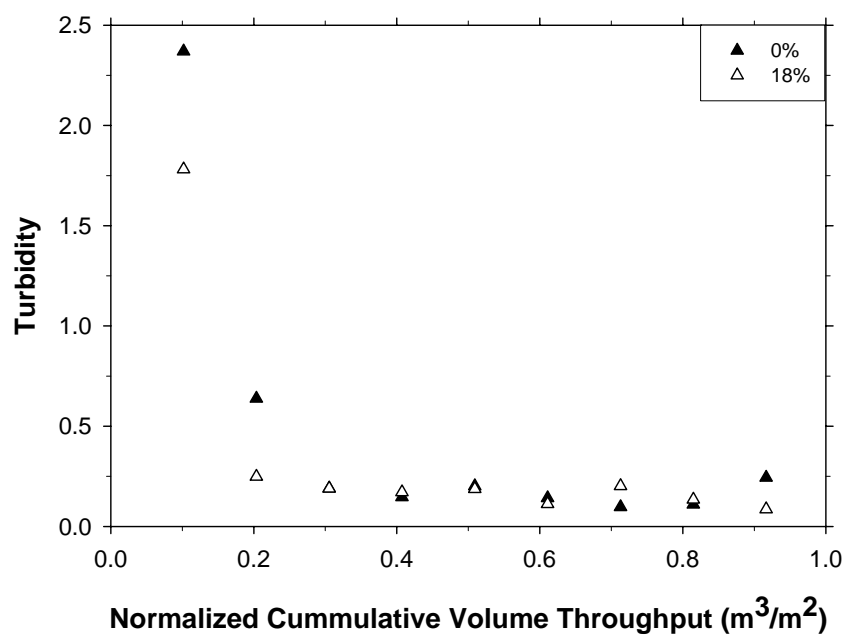


Figure 4.17 Turbidity results for permeate suspension concentration with 10 mg/L Min-u-sil 5 feed for 3 μm PET membrane, non-stretched and at 18% strain

For the 10 μm PET membranes, Min-u-sil 30 particle challenge samples were analyzed using two different size aperture tubes on the Coulter Counter and using the turbidimeter. As shown in Figure 4.18, data indicate that initially, for particles less than the pore size, rejection is similar for all membranes tested. As volume throughput increases, particle concentration is too low to be read by the turbidimeter. All membranes seem to show significant rejection of particles greater than the pore size. More interesting results may be obtained by choosing particle challenge more appropriate for this pore size.

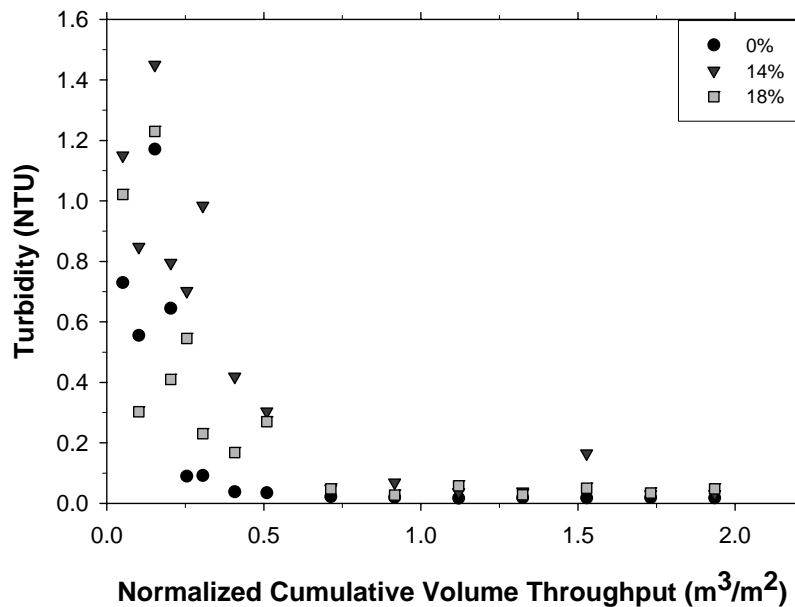


Figure 4.18 Turbidity results for permeate suspension concentration with 10 mg/L Min-u-sil 30 feed for 10 μm PET membrane, non-stretched and at 14 and 18% strain

The small improvement in rejection for the stretched membranes in comparison to the non-stretched membranes during the Min-u-sil experiments can cause a slightly different cake layer to build on the membrane surface in the two cases. The greater rejection of small particles means that the cake layer is built with a more heterodisperse size distribution, and Huang *et al.* [28] indicated that the structure of the cake is mildly impacted by the heterodispersity of the particles. However, our interpretation is that the greater permeance of the stretched membranes throughout the Min-u-sil experiments (shown in Figures 6 and 8) is due to the improved permeance of the filter itself (Table 1). The total resistance is the sum of resistances of the cake and the filter. The small differences in the cake itself (if any) are apparently outweighed by the difference in the filter resistance between the stretched and non-stretched membranes. This explanation is supported by the results of the experiments with the spherical particles, presented below.

4.2.2 Spherical Particle Challenge Permeate analysis

Turbidity results were also obtained for the 0.6 μm PET membranes, which were challenged with the 0.652 μm spherical beads. These beads were too small for the Coulter counter to read accurately, so turbidity results are the only ones available. They show in Figure 4.19 that almost no particles were able to get through the non-stretched samples at any stage of the experiment, but some particles were able to get through the stretched sample throughout the experiment. The fact that the turbidity increases towards the end of the experiment indicates that some contamination took place in those samples, and they should be disregarded. The first samples, however, look reasonable and must be considered in the analysis.

Particle challenges using spherical polystyrene beads of 2.02 μm diameter were completed for the 2 μm PET membranes. Table 4.3 summarizes the rejection results in terms of number concentration for 22, 24, and 27% stretches compared to non-stretched membranes; as before, negative values indicate that stretching improved particle removal. This presentation of the data represents the number concentration in particles per mL when data are averaged for six Coulter Counter size channels around 2 μm . Particle size distribution functions indicate some improvement in particle rejection with stretching.

Greater volume throughputs do not show any significant difference between membranes because particle counts become low for all membranes. These results indicate that for the spherical particle rejection experiments, rejection improves with stretching.

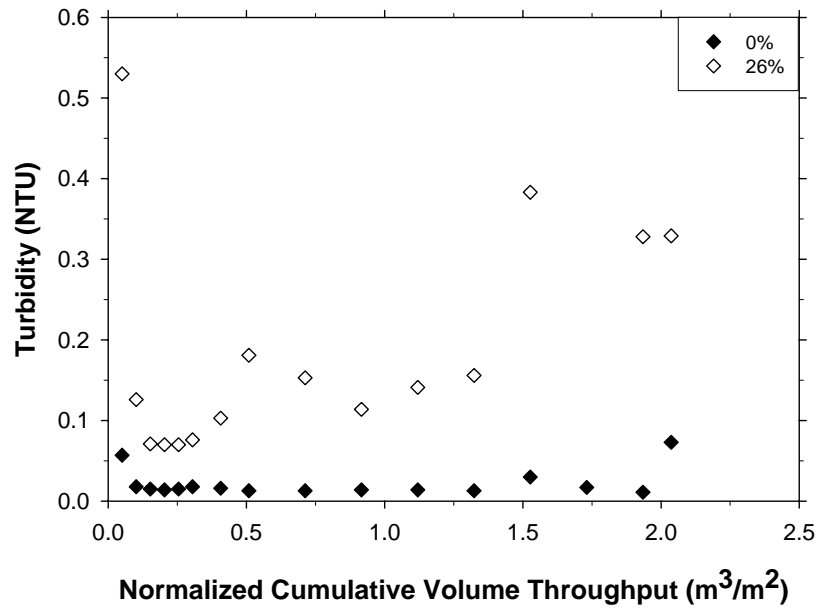


Figure 4.19 Turbidity results for permeated suspension concentration with 0.652 μm spherical particles on 0.6 μm PET membrane

Table 4.3
Change in number concentration of 2.02 μm spherical particles on 2 μm PET membrane

Strain (%)	Normalized cumulative volume throughput (m^3/m^2)	$\Delta 2.02 \mu\text{m}$ Particle number concentration (number concentration in # particles / mL)
22	50	-64.8%
24	50	-32.6%
27	50	-53.0%
22	100	-66.7%
24	100	-74.1%
27	100	-62.0%
22	400	-50.6%
27	400	-73.5%

CHAPTER 5: MODELING RESULTS

5.1 GEOMETRY STUDY

Perhaps the first question to ask when attempting to model the stretching of a porous material is how much the actual material is going to affect results. Could the changes in pore size and shape be attributed entirely to geometry such that the pore deforms, but the pore wall does not stretch? If the material does not deform, material properties are not important to the pore deformation. To answer these questions, a simple geometry study was performed. Simplifying assumptions were made for several cases and parameters were calculated and compared to experimental data from the “Materials Results” chapter to determine if the assumptions were reasonable. The first case assumed a constant pore perimeter, meaning that the wall of the pore could not stretch. The major axis was taken to increase with strain following the experimental data, and minor axis and area were calculated assuming the final pore shape to be perfectly elliptical. Table 5.1 shows the results of this study.

If the pore wall is not allowed to stretch, as major axis increases, minor axis must decrease and area must also decrease since the pore has the most area possible when major axis is equal to minor axis, meaning it is circular. Since area is seen in actual data to increase, as in Figure 3.5, the assumption that perimeter is constant must be false. The pore wall must stretch as the pore deforms. Major axis could also have been taken to increase directly with strain, or the behavior of the minor axis could have been taken from the data major axis calculated. Regardless, the same result is obtained.

Table 5.1
Geometry study results for the constant perimeter assumption

Strain (%)	Calculated Area (μm^2)	Calculated Minor Axis (μm)	Actual Area (μm^2)	Actual Minor Axis (μm)
3.9	2.2	1.2	3.1	1.6
8.7	1.8	0.9	3.5	1.7

5.2 MESH REFINEMENT AND ONE-HOLE STUDIES

Mesh dependent results are not useful. However, the less fine a mesh, the less computational time is required to perform the simulation of pore stretching. Also, meshes can be too fine, with elements that are distorted or have larger angles than are ideal for simulation. Therefore, some mesh refinement study was appropriate. The first meshes were drawn by the user in .inp files. The 2-dimensional meshes increase in complexity from 4 elements to 720 elements. The 4, 8, and 16-element meshes are shown in Figure 5.1. These meshes can already be disregarded as insufficient due to their inability to capture the circular shape of the pore. The next three meshes, shown in Figure 5.2, have 48, 200, and 720 elements each. These meshes, as are all discussed in the next few sections, are given arbitrary viscoelastic and hyperelastic properties and stretched 40% in order to determine their effectiveness at simulating the stretching of a single pore in that type of material. The hyperelastic model employed here is the Mooney-Rivlin, and a one-term Prony series is also used. In addition, the 200-element mesh was recreated, shown in Figure 5.3 (A), with a hole half the diameter of the hole in previous simulations, such that the diameter of the pore is 1 unit, to determine if the walls of the mesh were affecting the pore deformation; otherwise stated, the smaller hole could be compared to the larger ones to determine how isolated they were from edge effects. Also shown in Figure 5.3 (B) is a mesh generated in ABAQUS CAE with one hole, this hole 1 unit in radius like the meshes shown in Figure 5.2. This mesh was seeded such that there would be twice as many elements along the edges of the sample, but because there is no gradient in element size or number there are actually fewer elements surrounding the pore.

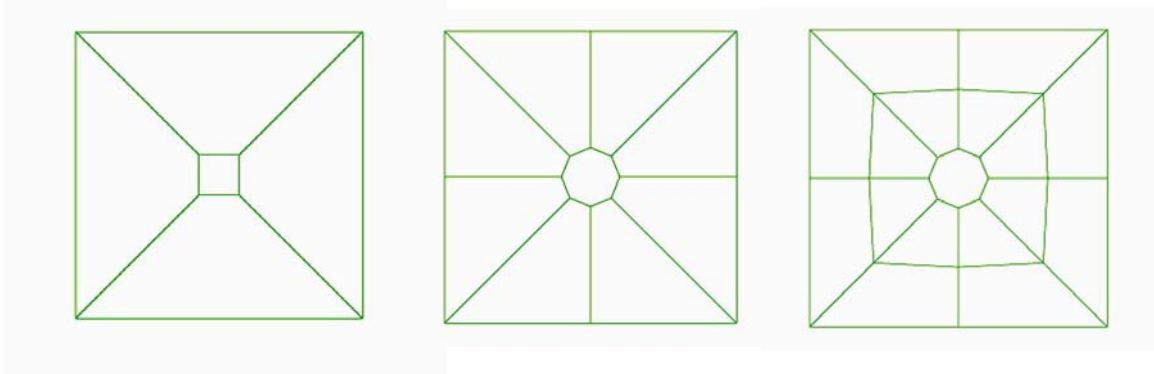


Figure 5.1 4, 8, and 16 element user-created meshes with a single pore of 1 unit radius

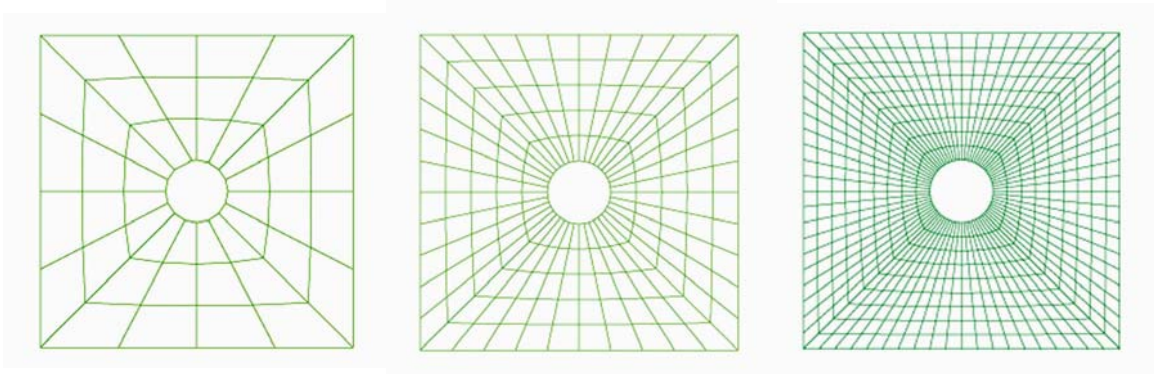


Figure 5.2 48, 200, and 720 element user-created meshes with a single pore of 1 unit radius

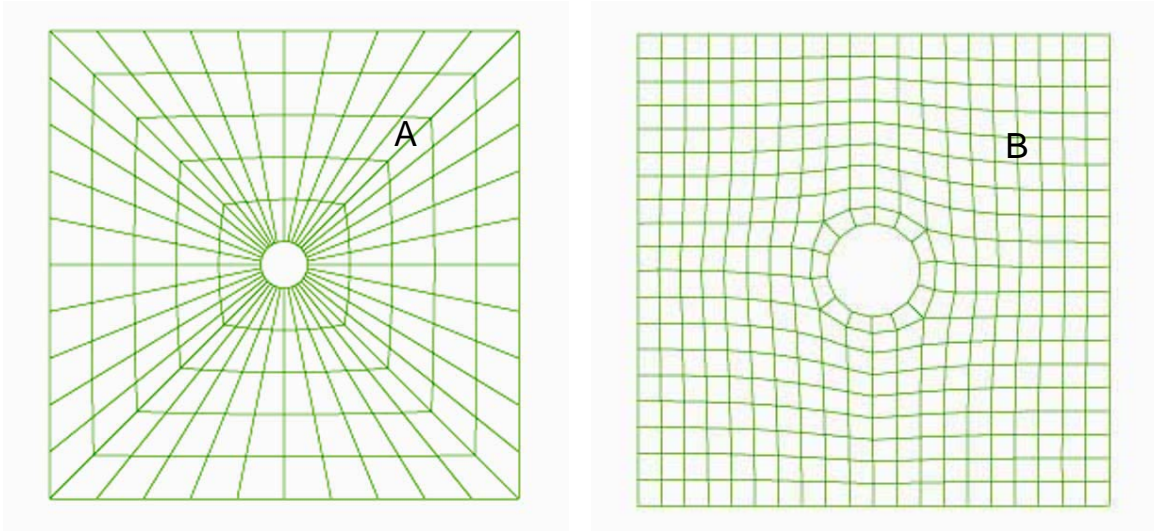


Figure 5.3 User-defined 200-element mesh with a single pore of 1 unit diameter (A). CAE generate single pore mesh (B)

Results are shown in Table 5.2. Aspect ratio is unaffected by mesh size or pore size, but area is significantly effected by the mesh and pore size, especially by the pore size. The small pore simulation is significantly different from the others in its results, but it is also significantly different from experimental results. This pore is obviously the most isolated, being the farthest away from any possible edge effects. Edge effects are significant to the prediction of pore area, which suggests that interaction effect may also be important. The 720 element mesh took three times as long to process as the 200 element mesh. Because simulations are increasing in complexity for this study and the results from these two meshes are similar, the 200 element mesh is considered the best of the user-defined meshes. The CAE defined mesh took significantly less time than any of the user-defined meshes, so it will also be used for comparison to experimental data.

One qualitative result to come out of all simulated single pores results is the resulting stress field around the stretched pore. Figure 5.4 shows the resulting von Mises stress distribution for the 200 and 720-element user defined meshes and the CAE mesh all displayed in ABAQUS VIEWER. In all cases, the area of highest stress occurs on either side of the pore along the pore wall, with the stress diminishing outward toward the edge of the sample. The area of lowest stress occurs just above and below the pore. It can be surmised that in the simulated stretch the pore wall along the sides must stretch more than the pore wall above and below the pore. The pore wall in these areas bends as necessary to accommodate the “necking” of the sample, or the sample getting less wide as stretched, which is evident both experimentally and in simulation. The high stress area is small, taking up about 1/3 of the pore wall on either side. These stresses are indicators for predicting pore interactions. Pores that are next to each other are likely to interact differently than those on top of one another. Also note that the CAE mesh is not symmetrical, so its solution is also slightly non-symmetrical.

Table 5.2
Mesh refinement results, comparing change in pore characteristics

Mesh	Area	Major Axis	Minor axis	Aspect ratio
Change (%)				
48-element	54.0	110.0	-20.0	166.0
200-element	47.0	102.0	-20.0	153.0
720-element	66.0	106.0	-20.0	156.0
Half-diameter pore	28.7	95.0	-28.0	171.0
CAE mesh	55.3	101.6	-22.3	161.8

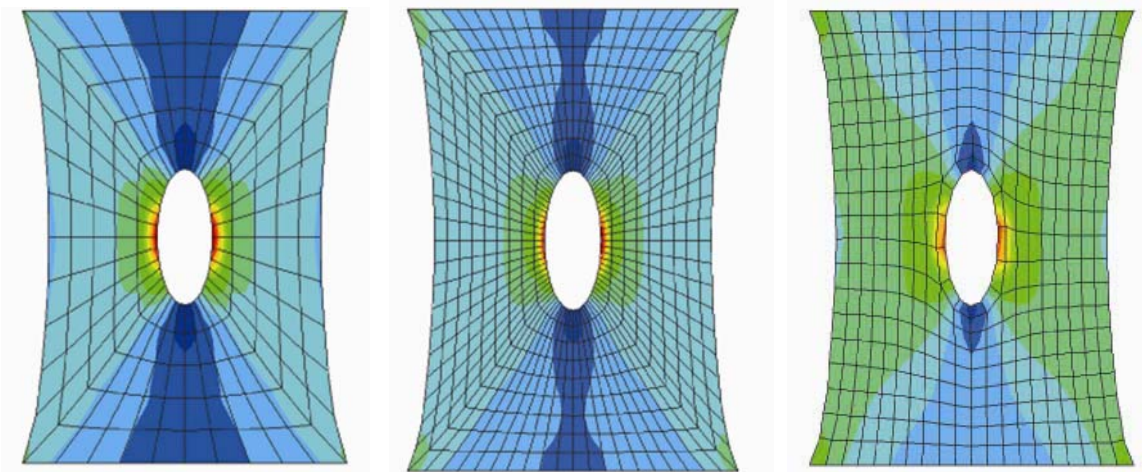


Figure 5.4 Resulting stress distribution from a 40% simulated stretch with the 200 and 720 element user-defined meshes, as well as the CAE generated mesh

5.3 TWO-HOLE STUDIES

To begin studying pore interactions, two-hole studies were conducted. The first meshes for these were done as .inp files created by the user. For these, the 200-element mesh was used twice, back to back over a smaller space, so that a 400-element mesh resulted. The two pores were drawn at varying distances from each other, such that their centers were 4, 3, and 2.5 units apart for circles of 2 unit diameters. The mesh with pores 4-units apart is shown in Figure 5.5. In addition, the orientation of these pores, or the angle formed by a line drawn between the two centers and the horizontal, was adjusted in a couple of formations, and one of these meshes is shown in Figure 5.6.

Running these meshes in ABAQUS generated warning messages due to the large angles in the elements located between the two pores. To determine if these warnings

would cause inaccuracies in the results, meshes were also generated in CAE, and an example of these is shown in Figure 5.7. These meshes were created with the some of the same unit distances and orientations as the above user defined meshes from Figure 5.6.

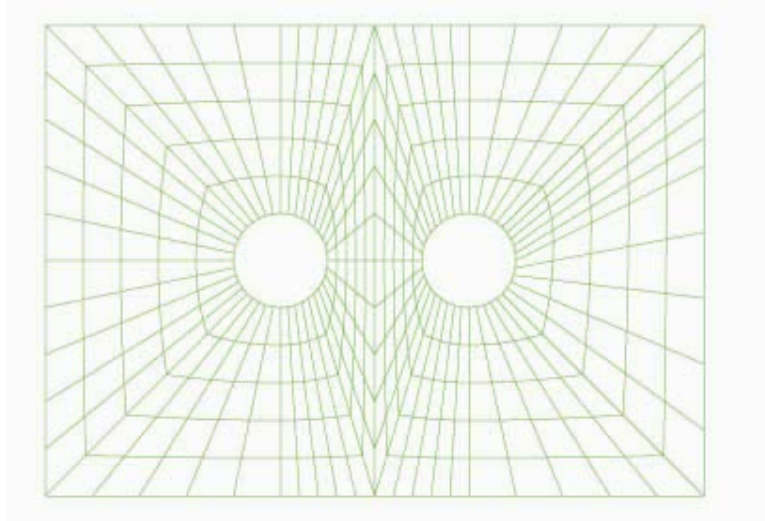


Figure 5.5: Two-hole user defined mesh based on the 200 element single pore mesh with pores 4 units apart at the center

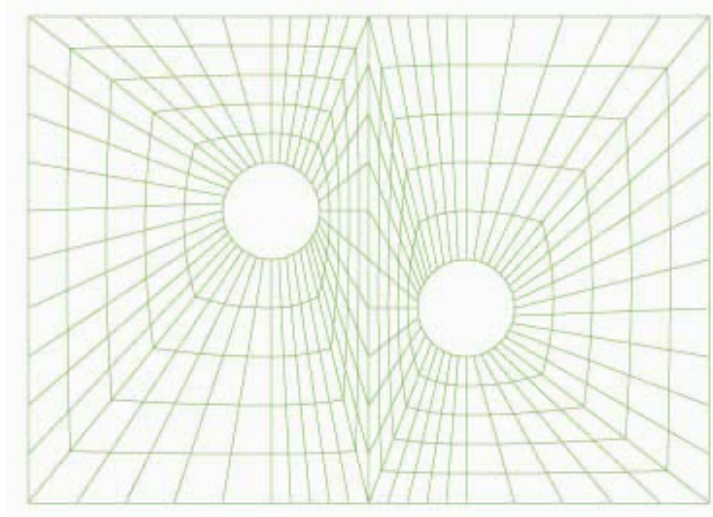


Figure 5.6: Two-hole user defined mesh based on the 200 element single pore mesh with pore 4 units apart at the center and aligned at an angle of 45° from the direction of stretching

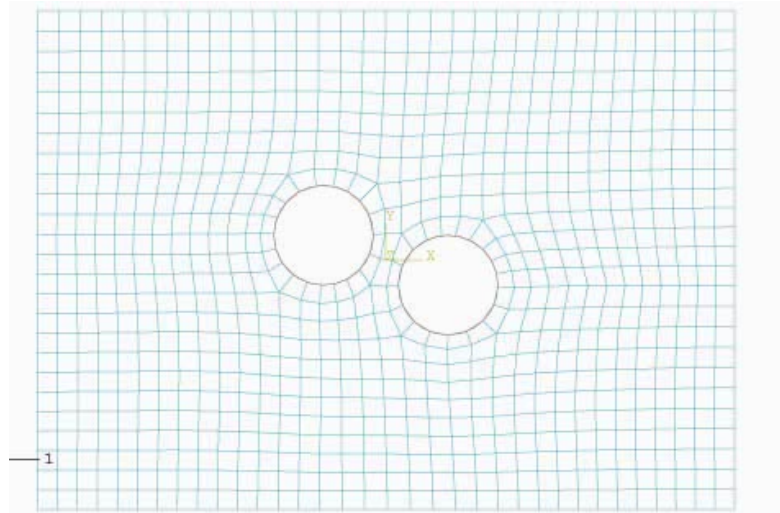


Figure 5.7 Two-hole CAE defined mesh with pores 2.5 units apart at the center and skewed from horizontal alignment

The results of stretching the user-defined two-hole meshes at varying pore proximity are shown in Table 5.3. A much greater increase in area is seen upon stretching for both pores over the single pore simulations, and a much smaller change in minor axis is seen upon stretching as compared to the one pore simulation, demonstrating the effect of closer pore interactions. The stress distribution around the pores, shown in Figure 5.8, is similar to that of the one-hole studies shown in Figure 5.4. The area of highest stress is greater in magnitude between the pores, as opposed to outside them, and covers a larger section of the pore wall. The overall effect of having two pores next to each other during stretching is to keep the minor axis from decreasing while still allowing the major axis to increase, which causes the area of the pore to increase at a greater rate as a function of strain, but not the aspect ratio. Moving the pores closer together increases the major axis, at least at first, but the minor axis behavior is unexpected, decreasing, then increasing, then decreasing again. The characteristics of each pore are measured, major and minor axis and area, so that there are two results reported for each simulation in Table 5.3.

Table 5.3
Results of two-hole user defined meshes stretched 40%

Mesh	Area	Major axis	Minor axis	Aspect ratio
Change (%)				
4 units apart	88.6	106.8	-8.7	126.5
	88.6	106.8	-8.6	126.7
3 units apart	107.0	118.3	-5.2	130.2
	105.2	117.1	-5.5	129.7
2.5 units apart	100.3	119.1	-8.6	139.6
	101.1	119.1	-8.2	138.7
One hole result	47.0	102.0	-20.0	153.0

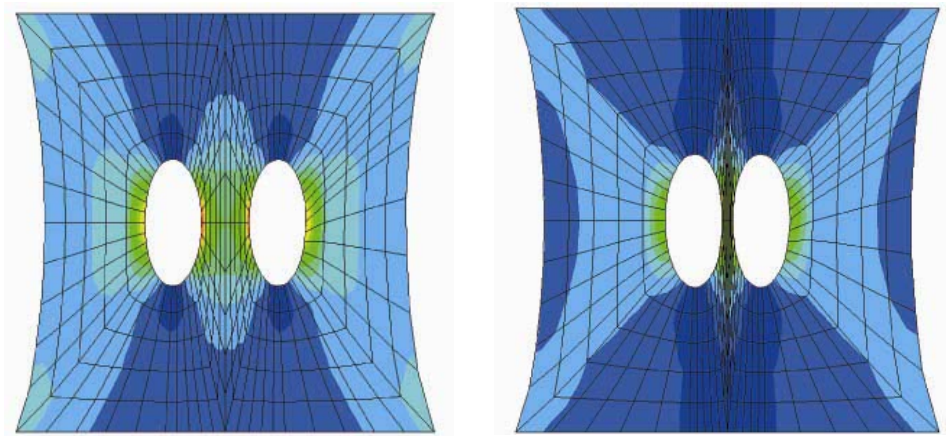


Figure 5.8 Results of two-hole studies for user-defined meshes stretched 40%

For the skewed results, major axis increases with proximity, or the distance between pores, and minor axis decreases with proximity. This increases aspect ratio, and although the change in area is still comparable to the two-pore studies discussed above, area does not change significantly with proximity.

The two-hole results from the CAE generated meshed are presented in Table 5.4. The CAE mesh for two-holes predicts a larger decrease in minor axis than its .inp counterpart at 4 units apart, causing smaller area and greater aspect ratio results. The stress distributions, shown in Figure 5.9, are similar to those of the use-defined meshes, showing areas of high stress at the sides of the pores. Moving the pores closer together causes a smaller decrease in minor axis and a larger increase in major axis, resulting in greater pore area. This suggests that a membrane with high porosity, or a higher

occurrence of pores that are close together, is likely to results in the largest increase in area as a function of strain and therefore the largest increase in overall porosity. As seen in the case of the .inp files, the area of highest stress is between the pores, with much less stress on the outside wall of the pore. Skewing the pores causes the minor axis to decrease again with similar, slightly lower major axis results. In this case again, the area of highest stress is between the pores.

Table 5.4
Results of CAE generated two-hole meshes stretched 40%

Mesh	Area	Major axis	Minor axis	Aspect ratio
	Change (%)			
4 units	77.4	102.9	-12.5	132.1
	77.0	103.1	-12.8	132.2
2.5 units apart	94.7	120.3	-10.2	145.3
	97.6	119.9	-10.1	144.7
2.5 units skewed	89.5	115.5	-12.0	145.0
	89.6	115.6	-12.3	146.0

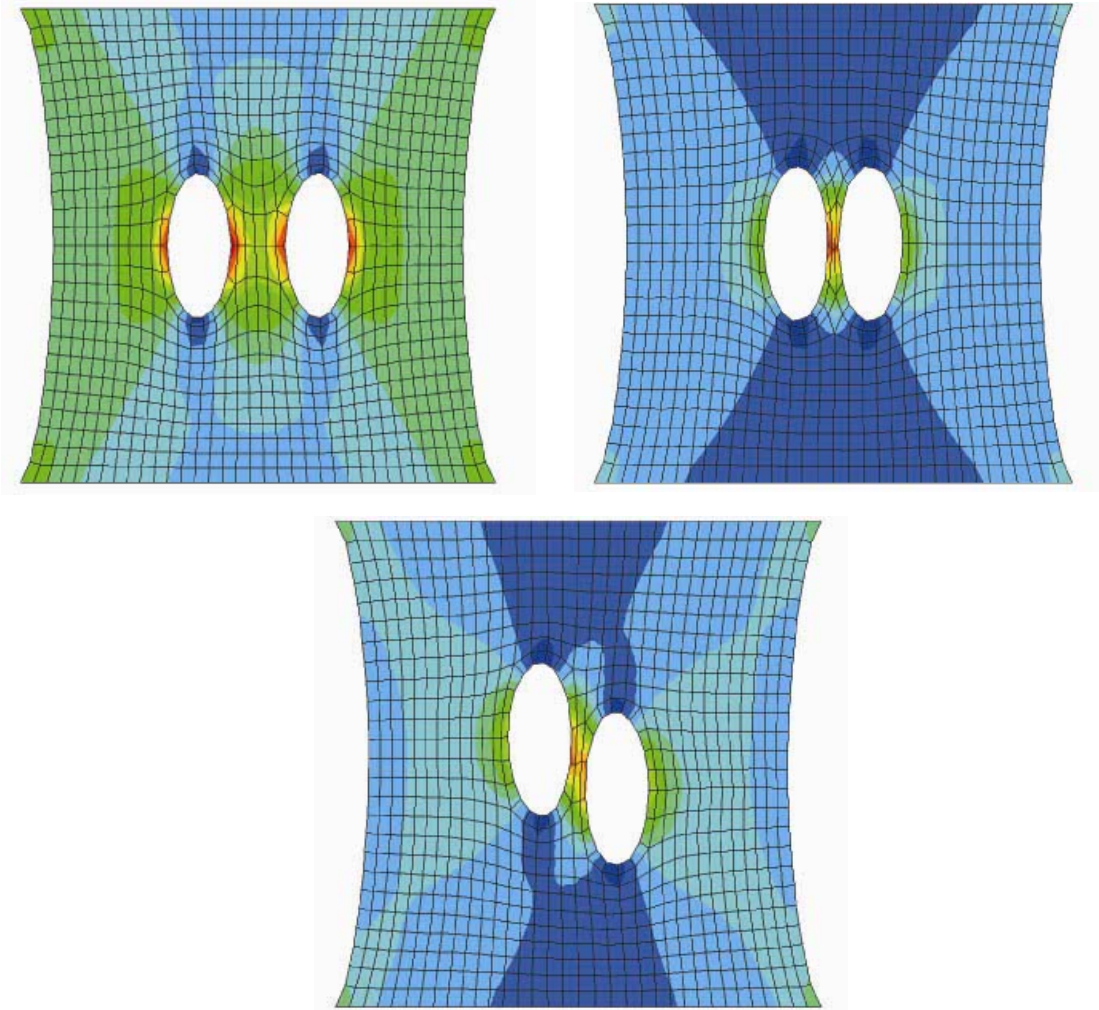


Figure 5.9 Two-hole results for CAE generated meshed stretched 40%

In general, interactions increase pore area upon stretch at a greater rate than without interactions and decrease the ability of the minor axis to change upon stretching. These effects are proximity and orientation dependent due to the stress distribution around stretched pores.

5.4 SINGLE PORE EXPERIMENTAL RESULTS

In order to compare results, single pores were chosen from micrographs of membranes with low, medium, and high porosity. The 1 μm PET membrane has a porosity of 1%, the 2 μm PET membrane has a porosity of 6 or 7%, depending on the batch from which the sample came, and the 3 μm PET membrane has a porosity of 15%.

The pore characteristics of these single pores were measured and averages were taken, so that any effects from overlapping pores, which were accounted for in the results reported previously in the “Materials Results” chapter, could be eliminated, and isolated pores would be taken into account. Pores were specifically chosen for measurement as “isolated” based on their distance from neighboring pores to try to eliminate interaction effects as much as possible. These experimental are shown in Table 5.5.

Table 5.5
Single pore experimental results

Membrane	Area	Major axis	Minor axis	Aspect ratio
		Change (%)		
1 μm PET 20%	51.3	50.5	2.2	46.8
2 μm PET 8%	30.1	28.2	1.2	26.3
2 μm PET 18%	32.5	58.0	-16.2	87.8
2 μm PET 28%	60.0	65.2	-11.0	84.9
2 μm PET 38%	77.2	107.7	-14.5	142.0
3 μm PET 21%	46.5	48.5	-1.6	51.4

5.5 SENSITIVITY OF SIMULATION TO ARBITRARY MATERIAL PROPERTIES

Before entering actual properties into the simulations, some sensitivity studies were conducted to determine the effect of material properties on pore size and shape. Hyperelastic and Prony parameters were varied to determine the sensitivity of the simulation to those properties. The coefficients of the Mooney-Rivlin model were varied first in three different cases, including the original arbitrary case. The results of these simulations are shown in Table 5.6 and Figure 5.10. Little difference is apparent in area, and almost no difference can be seen in aspect ratio as a function of these coefficients, demonstrating that pore characteristics are not sensitive to the parameters chosen for the hyperelastic model. An interesting result from the hyperelastic variation is the change in stress distribution around the pores. The red area of high stress around the pore gets smaller as the parameters for the hyperelastic model get smaller, and the surrounding stress distribution changes as well, suggesting that, although hyperelastic parameters do not affect single pore characteristics, they may have an affect on pore interactions.

Table 5.6
Results for hyperelastic sensitivity study with 200 element user defined mesh

Hyperelastic model	Area	Major axis	Minor axis	Aspect ratio
			Change (%)	
arbitrary	66.0	106.0	-20.0	156.0
1/2	75.5	108.8	-15.9	148.2
1/10	77.9	112.6	-16.3	154.1

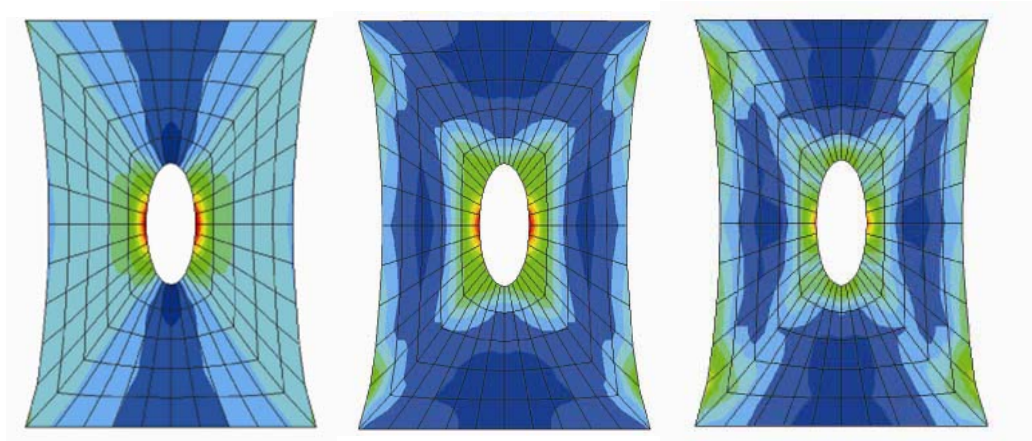


Figure 5.10: Results for hyperelastic sensitivity study with 200 element user defined mesh

The Prony series coefficients were also varied and the model tested for its sensitivity to them. The original arbitrary case was one of a one term Prony series for a compressible material, where the shear and bulk moduli were equal. The two other cases were for a nearly incompressible material, meaning the shear modulus was small compared to the bulk modulus, and a two term series where the moduli were again equal. Table 5.7 and Figure 5.11 show the results of these studies. Aspect ratio and area are not significantly affected by the parameters of the Prony series. The stress distribution along the pore wall is not affected by these parameters either, but the surrounding stress distribution again suggests possible interaction effects.

Table 5.7
Results for Prony sensitivity study with 200 element user defined mesh

Prony series	Area	Major axis	Minor axis	Aspect ratio
One term compressible	66.0	106.0	-20.0	156.0
One term incompressible	72.8	106.5	-16.4	146.9
Two term compressible	69.7	106.7	-17.9	151.8

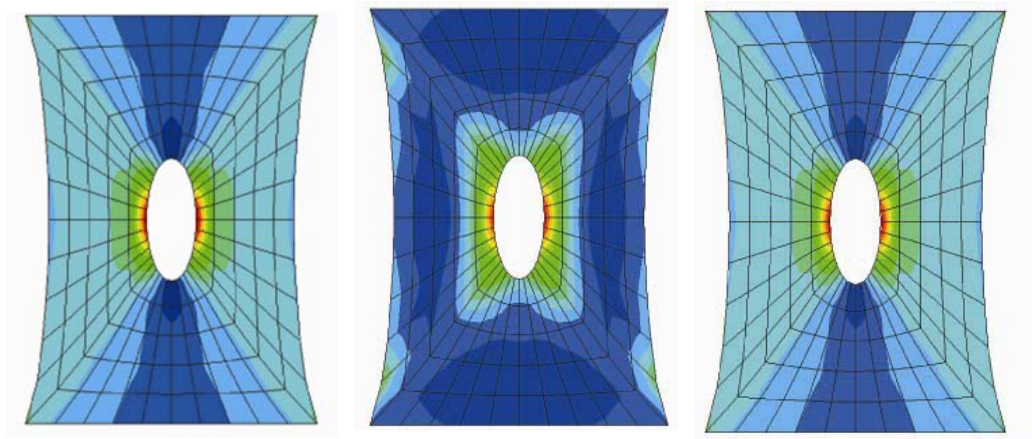


Figure 5.11 Results for Prony sensitivity study with the 200 element used defined mesh

5.6 OBTAINING MATERIAL PROPERTIES

5.6.1 Prony Series

A series of relaxation experiments were performed as discussed in the “Methods and Materials” chapter, and the results were shifted according to the WLF equation. The resulting master curve is shown in Figure 12. A curve was drawn through this data, and using the least squares method described in the Methods and Materials chapter, the Prony Series was fit. The results of this fit, and the normalization, are shown in Table 8. Comparison to literature data on PET shows good agreement with previously obtained results. The study by Murayama, et al. showed a relaxation curve over the same number of decades as that shown in Figure 8, but a reference temperature of 82°C was chosen for the plot in that paper, as opposed to a reference temperature of 125°C which was used for this study, so the time scale is shifted here from that reported by Murayama (Murayama et al. 1968). The relaxation of the PET studied by Murayama occurred about a decade in terms of the log of relaxation modulus, again matching the results shown in Figure 8. However, the value of the modulus reported in the Marayama paper is higher than that found in this study (Murayama et al. 1968). The study by Allison and Ward showing that crystallinity affects mechanical properties can explain this difference (Allison and Ward 1967), since the materials studied here are of different crystallinity.

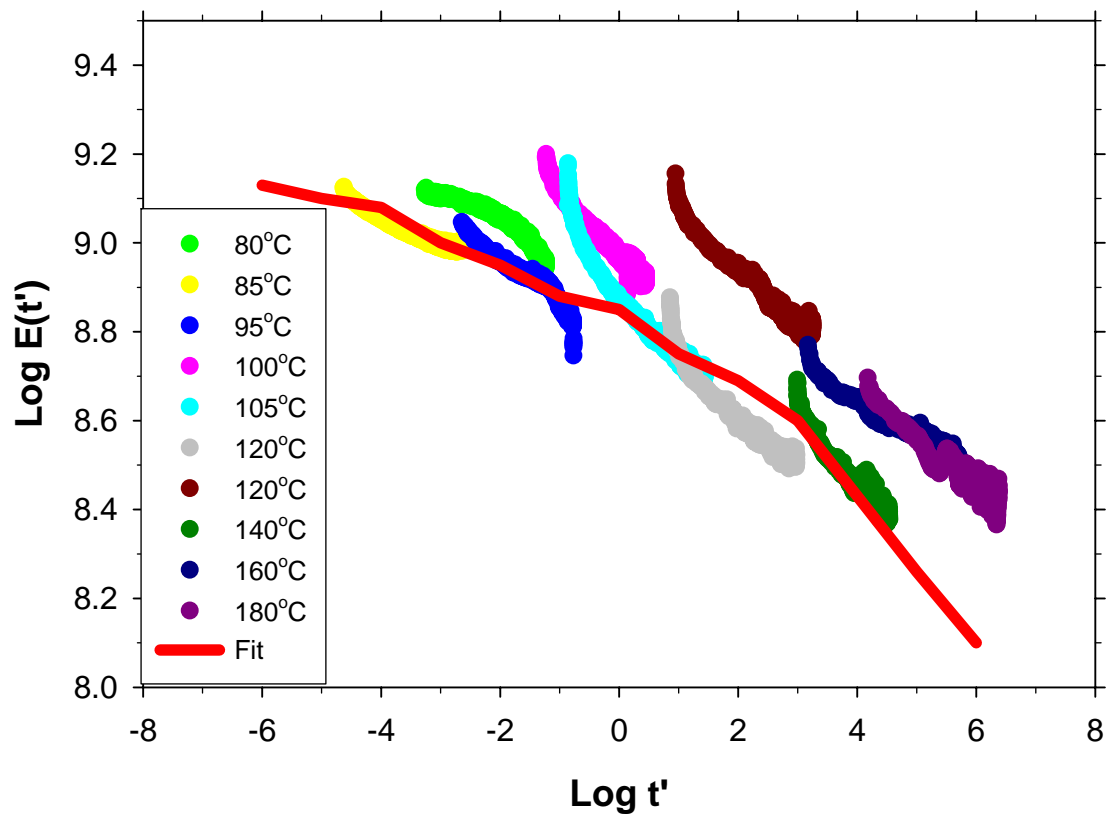


Figure 5.12 Relaxation experiments shifted and plotted as the log of the relaxation function versus log of shifted time to show the master curve

Table 5.8
Prony series coefficient obtained from the least squares
fit, and the normalized coefficients for ABAQUS
shown with time.

Coefficient	Normalized Coefficient	Time (s)
0.977	0.147	1.00×10^6
0.912	0.136	1.00×10^5
0.871	0.131	1.00×10^4
0.725	0.109	1.00×10^3
0.646	0.097	1.00×10^2
0.550	0.083	1.00×10^1
0.513	0.077	1.00×10^0
0.408	0.061	1.00×10^1
0.355	0.054	1.00×10^2
0.288	0.043	1.00×10^3
0.195	0.029	1.00×10^4
0.132	0.020	1.00×10^5
0.091	0.014	1.00×10^6

5.6.2 Hyperelasticity

In order to obtain the hyperelastic coefficients, constant strain rate experiments were performed as described in the Methods and Materials chapter at two temperatures, 100 and 160°C. These results are shown in Figure 5.13. Vigny, *et al.* performed a constant rate uniaxial test on amorphous PET at 90°C (Vigny 1999). With amorphous PET they were able to obtain a much greater strain, 160%, before failure, than that of the crystalline PET film used in this study. The value of stress recorded in the Vigny study is lower than shown in Figure 5.13 for the 100°C test by about one order of magnitude. The Vigny experiment was performed at a lower rate than that used in the experiment of Figure 5.13, such that the equilibrium modulus is obtained, instead of the instantaneous modulus which is shown in Figure 5.13. From the above relaxation curve, it is known that for PET these two moduli are about an order of magnitude apart. Comparison of

these results then shows that the data obtained in this study reasonably agrees with published data.

These data were fit in ABAQUS to several hyperelastic models, but few gave good results, and some did not converge on a solution at all. Figure 5.14 shows the results that were obtained. Because only uniaxial data was available, models using only the first invariant are the most appropriate. The Marlow model, which is such a model, gave the best agreement with the experimental data.

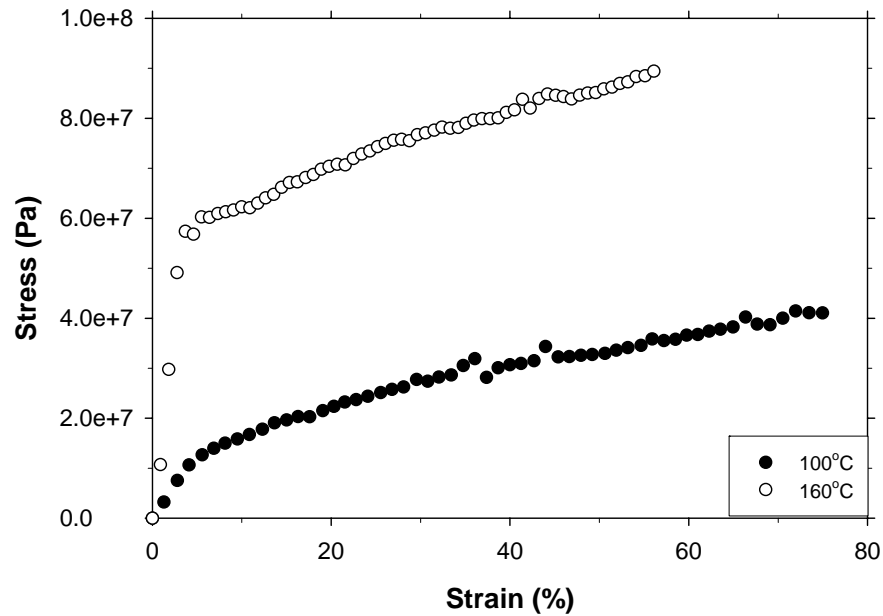


Figure 5.13 Stress-strain curves for PET dense film at 100 and 160°C

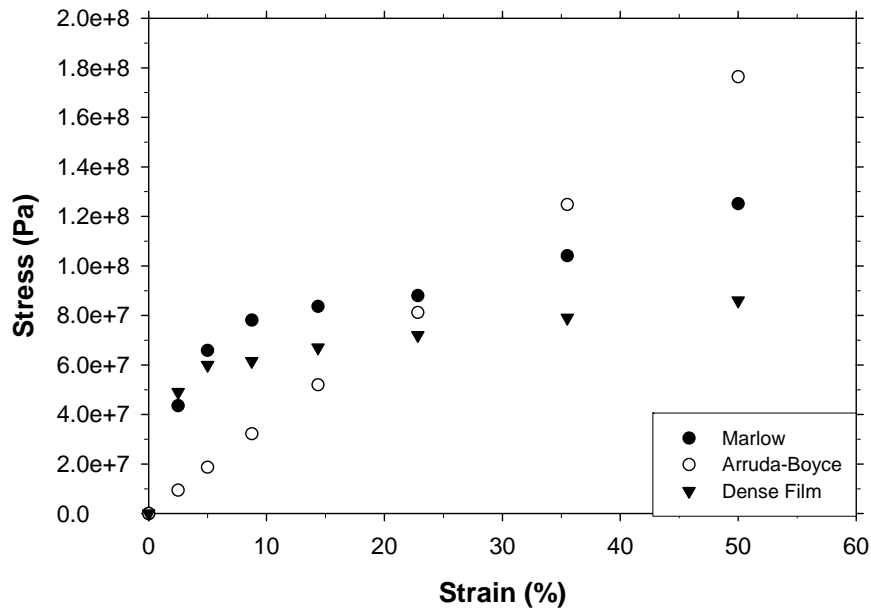


Figure 5.14 Stress-strain experimental data and the hyperelastic fit for the Arruda-Boyce and Marlow models

5.7 TWO-DIMENSIONAL SIMULATIONS WITH ACTUAL PROPERTIES

5.7.1 Sensitivity of Simulation to Hyperelastic Models with Actual Properties

The 200-element user-defined mesh was for simulations testing the sensitivity of the simulation to the hyperelastic model chosen. Stretches were simulated with all of the hyperelastic models that fit the data, and additionally with an elastic-viscoelastic model. The results are shown in Figure 5.15, as well as Table 5.9. The area and aspect ratio of pores are not sensitive to the model chosen with one obvious exception: the Marlow model is significantly different from all other models. This is apparent from the ABAQUS output pictures in Figure 5.15. The stress distribution around the Marlow pore is also significantly different. The wall of the pore has a greater amount in the red area, indicating more of it was under high stress, or more of the wall stretched, accounting for the greater change in major axis and therefore area and aspect ratio.

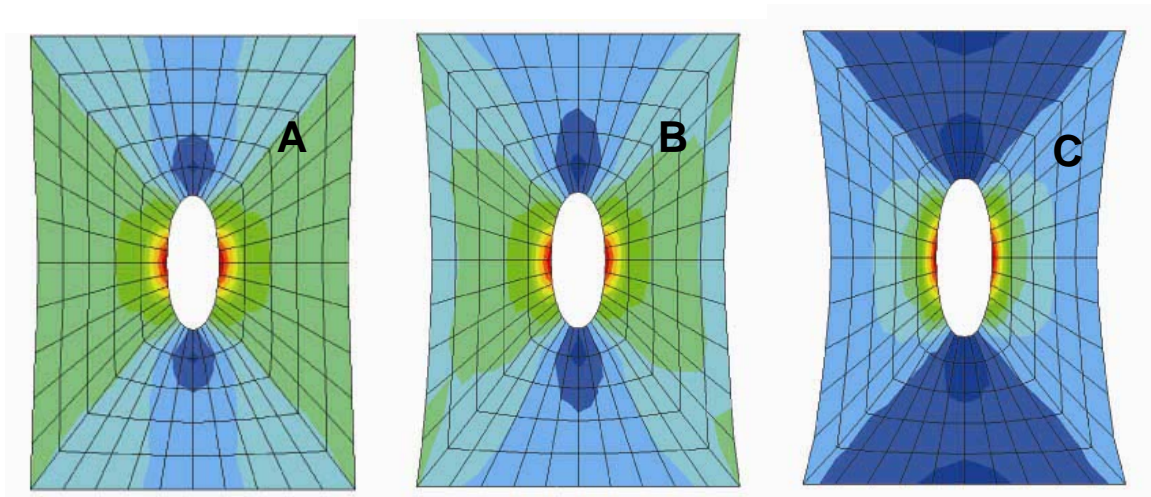


Figure 5.15 Sensitivity of pore characteristics to hyperelastic morel chosen

Table 5.9
Results of sensitivity study for hyperelastic model for 40% simulated stretches

Hyperelastic Model	Area	Major axis	Minor axis	Aspect ratio
	Change (%)			
Marlow	115.3	156.0	-15.9	204.4
Arruda-Boyce	72.8	110.3	-17.8	156.0
Viscoelastic	64.6	106.8	-20.4	159.9

5.7.2 Multiple Pore Study

5.7.2.1 Determination of number of pores and number of overlapping pores for simulation

To simulate the stretching of a representative membrane section, the appropriate number of pores for a given area must be determined, and also the appropriate number of overlapping pores. To simplify, only one configuration of overlapping pores will be considered. Each membrane has an individual pore size, pore density, and porosity. Instead of simulating all of the membranes, a representative of each available level of porosity was chosen for simulation. The 1 μm PET membrane has a porosity of 1%. For a membrane area of 100 square units and a pore diameter of 1 unit, this corresponds to a single pore study. Two batches of 2 μm PET membranes were used, one with 6.2% porosity and one with 7.1% porosity. The 3 μm PET membrane has a porosity of 15%. If the simulated membrane area is again 100 square units, and the radius of a pore is 1 unit, the 2 μm membrane has only 2 pores, and the 3 μm membrane has 5 pores. For the same membrane area but with a pore diameter of 1 unit, the 2 μm membrane has 8 pores corresponding to a porosity of 6.2%, 9 pores corresponding to a porosity of 7.1%, and the 3 μm membrane 19 pores. The number of overlaps is proportional to the pore density as described in the “Methods and Materials” chapter. The meshes with overlapping pores are summarized in Table 5.10.

Table 5.10
Multiple hole meshes defined in CAE based on membrane porosity and density

Membrane	Area (μm^2)	Number of Pores	Number of Overlapping Sets
2 μm PET	400	8 or 9	1
3 μm PET	225	5	1
3 μm PET	900	19	3

5.7.2.2 Multiple Hole Simulation Results

A mesh with 5 holes was created in ABAQUS having one overlapping set, as required by Table 5.10, which represented the 3 μm PET membrane. This mesh was stretched with both Marlow and Arruda-Boyce properties for comparison, and the results are shown in Figure 5.16, as well as in Table 5.11. Both hyperelastic models over predict the increase in area because both predict an increase in minor axis. The increase in major axis is similar for all three samples shown in Table 5.11.

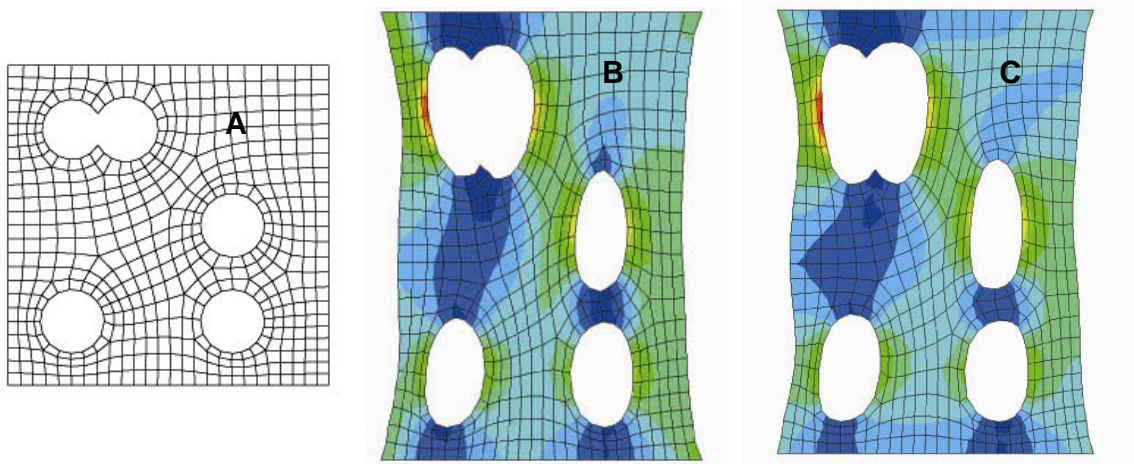


Figure 5.16 Results of stretching the 5-hole mesh (A) with Arruda-Boyce (B) and Marlow (C) hyperelastic models

Table 5.11
Results of stretching the 5-hole mesh with either Arruda-Boyce or Marlow hyperelastic models, compared to the experimental data for the 3 μm PET membrane

Model	Area (μm^2)	Major axis (μm)	Minor axis (μm)	Aspect ratio (--)
Arruda Boyce	31.2%	33.5%	1.7%	42.7%
Marlow	37.0%	31.8%	6.6%	33.3%
3 μm PET (21%)	23.3%	32.1%	-5.1%	43.8%

Next the 8-hole mesh was stretched with both Marlow and Arruda-Boyce properties. The results are shown in Figure 5.17 and Table 5.13. In this case, the mesh represents the 2 μm PET membrane, which has less than half the porosity of the 3 μm PET membrane. With less porosity, a decrease in minor axis is predicted, and area and major axis are under predicted by the Marlow model.

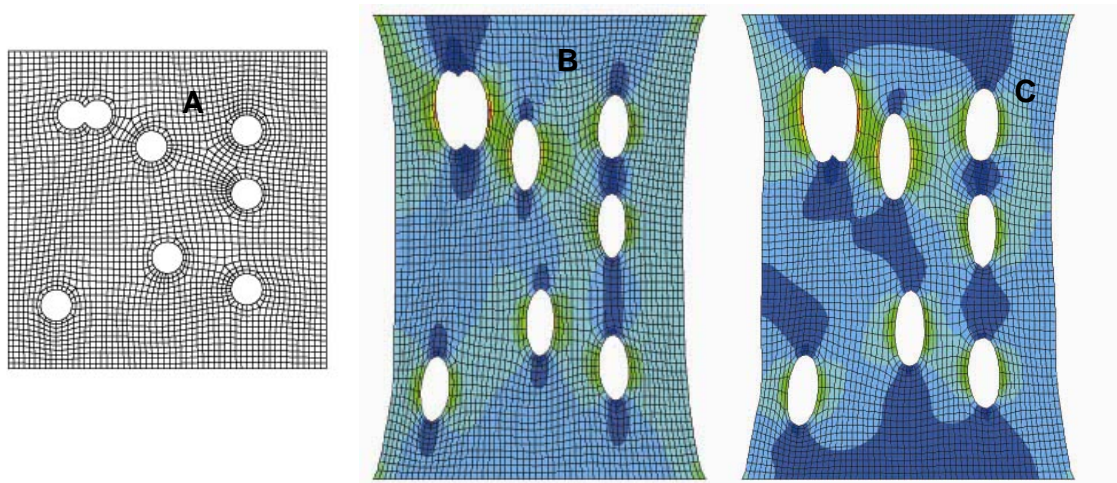


Figure 5.17 Results of stretching the 8-hole mesh (A) with Arruda-Boyce (B) and Marlow (C) hyperelastic models

Table 5.12
Results of stretching the 8-hole mesh with Arruda-Boyce and Marlow hyperelastic models

Model	Area	Major Axis	Minor Axis	Aspect Ratio
		Change (%)		
Arruda Boyce	51.4	59.0	-1.5	82.4
Marlow	75.6	83.7	-1.8	100.8
2 μm PET (32%)	77.0	89.0	-3.0	94.8

To study the evolution of pore shape, the 9-hole simulation, which corresponds to the 7.1% porosity 2 μm PET membrane, was stretched in simulation to 8, 18, 28 and 38%. The results of this are shown in Figure 5.18. The first picture shown is that of the mesh (A). The 8% is shown in (B), the 18% in (C), the 28% in (D), and the 38% in (E). Figure 5.19 gives a comparison of the change in pore shape for the simulation to that of the experimentally stretched membrane for area versus strain. The Marlow model predicts a linear increase in area with strain. The first datum point, at 8%, deviates from this line for the experimentally stretched membrane, but the others are in agreement with the Marlow prediction. Major axis is slightly under predicted consistently, as shown in Figure 5.20, and minor axis, shown in Figure 5.21, is predicted by the Marlow to increase instead of decrease. Aspect ratio, shown Figure 5.22, is scattered because of the minor axis data, but it follows closely the Marlow prediction.

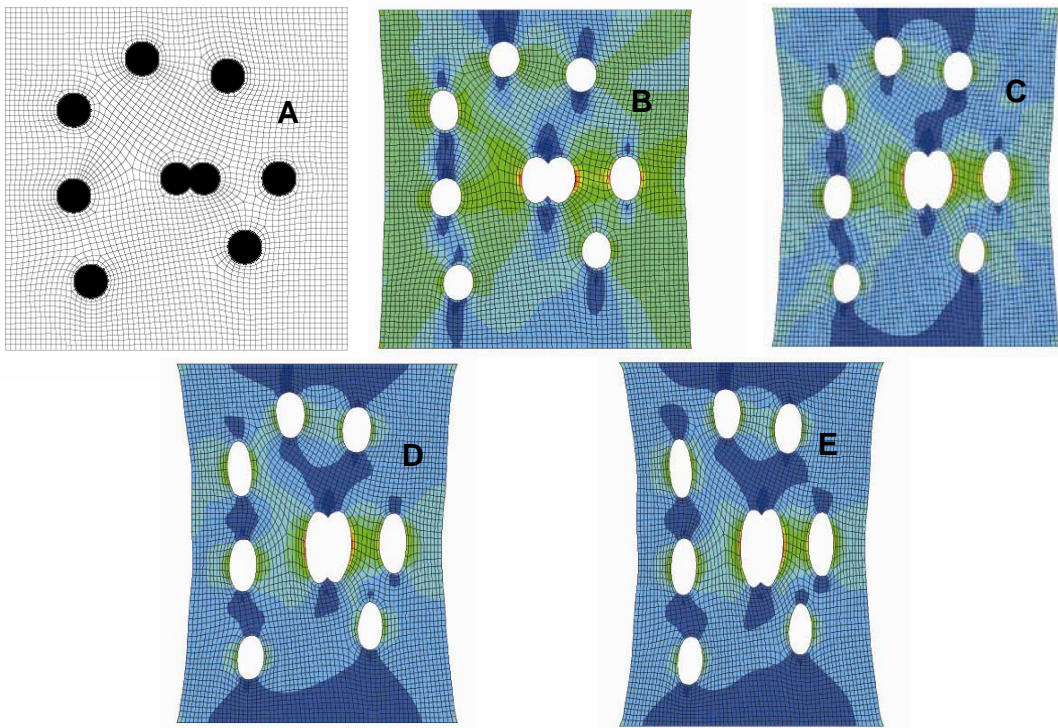


Figure 5.18 Results of stretching the 9-hole mesh (A) to 8% strain (B), 18% strain (C), 28% strain (D), and 38% strain (E) with the Marlow hyperelastic model

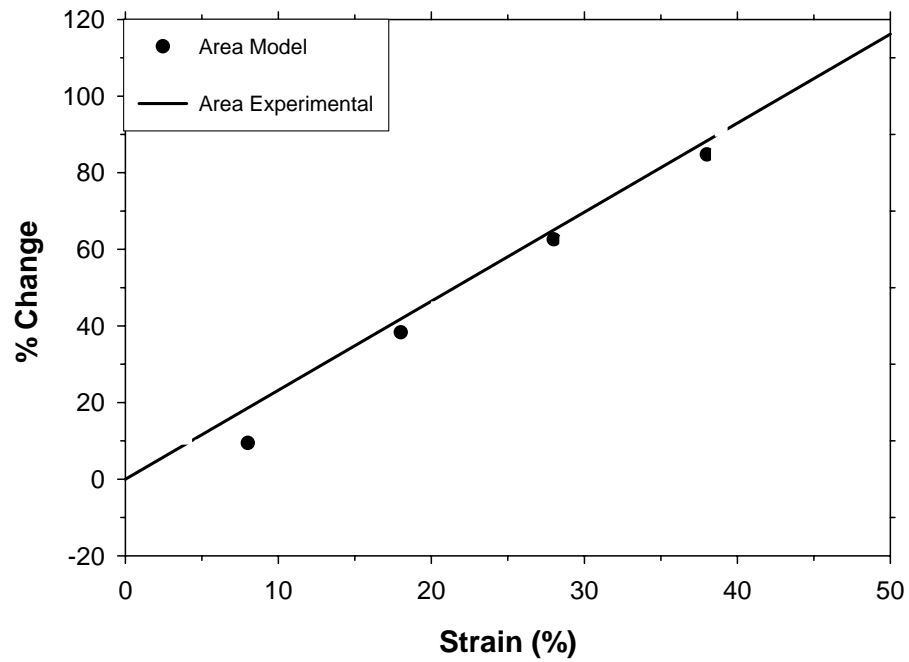


Figure 5.19 Area versus strain for the 9-hole simulation with Marlow properties and experimental data from the 2 μ m PET membrane

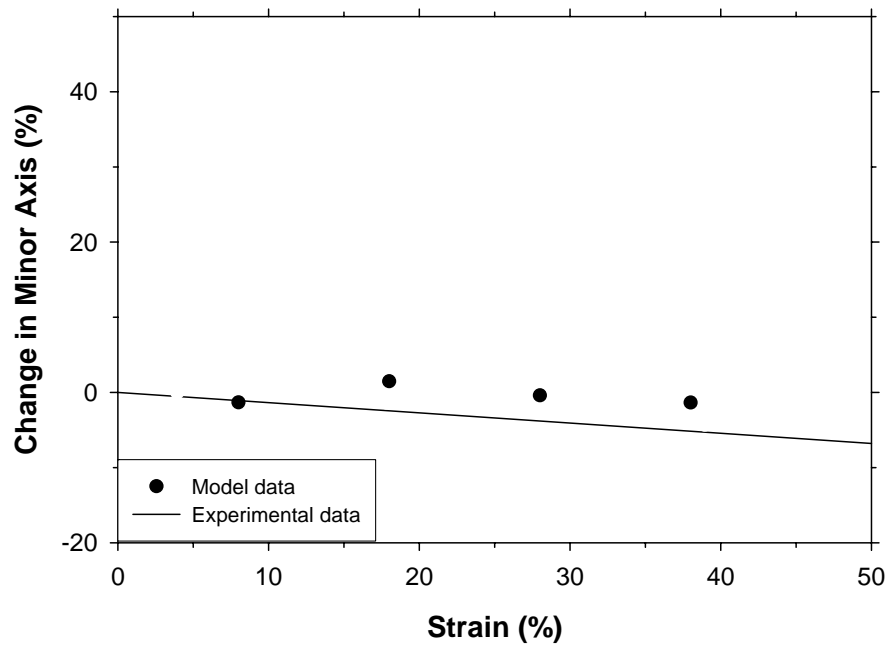


Figure 5.20 Major Axis versus strain for the 9-hole simulation with Marlow properties and experimental data from the PET 2 μ m membrane

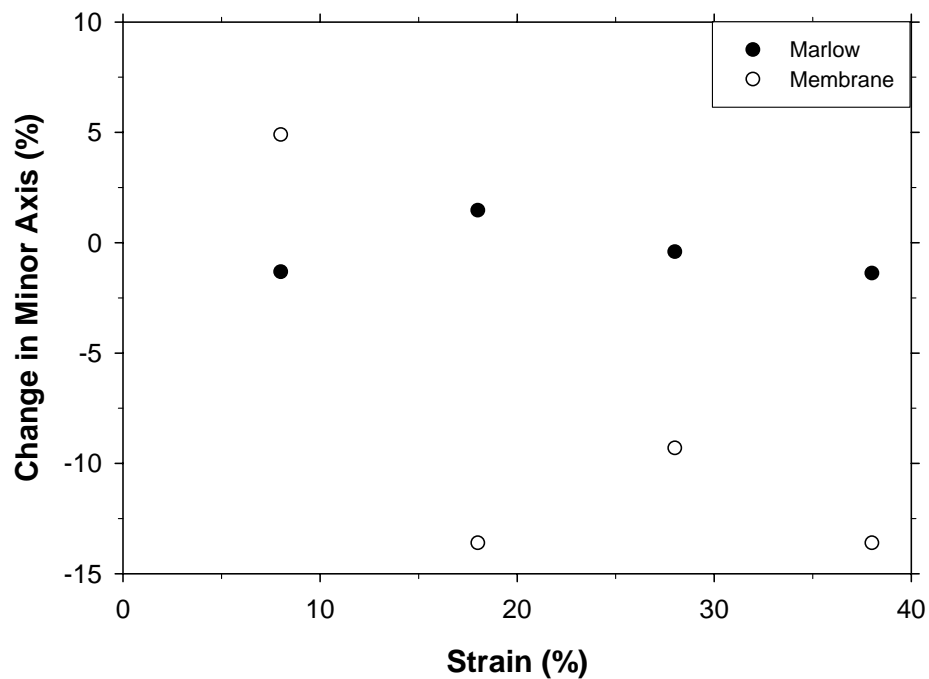


Figure 5.21 Minor axis versus strain for the 9-hole simulation with Marlow hyperelastic properties and experimental data from the PET 2 μm membrane

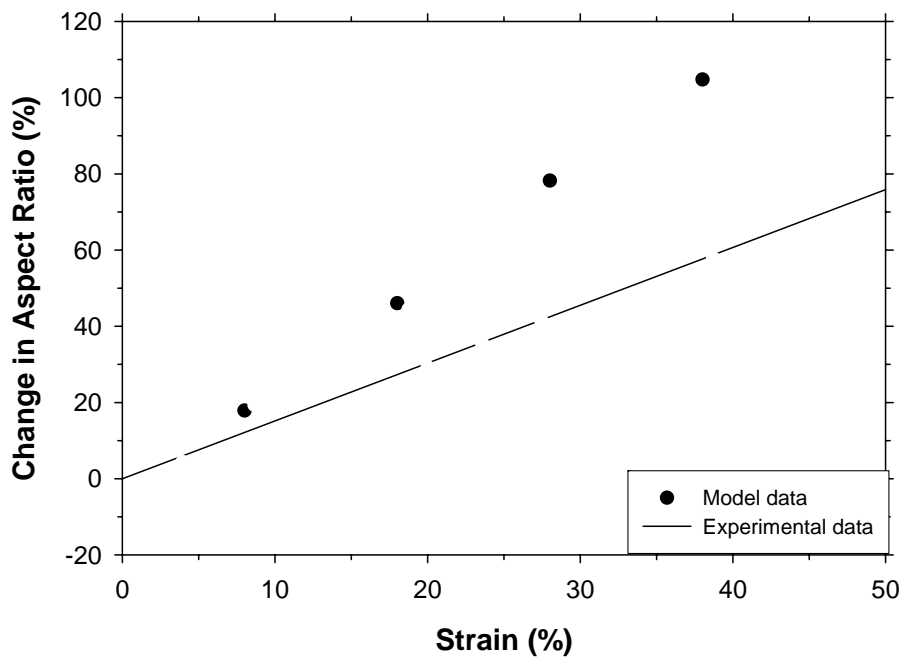


Figure 5.22 Aspect ratio versus strain for the 9-hole simulation with Marlow properties and experimental data from the PET 2 μm membrane

The last multiple hole study was a 19-hole mesh, which represents the 3 mm membrane. This mesh is shown in Figure 5.23 (A). The mesh was stretched with both Arruda-Boyce and Marlow hyperelastic models, and the results are shown in Table 5.13 and Figure 5.23. Like the 5-hole simulation, the change in area is over predicted, and the change in minor axis is predicted to be positive or very small.

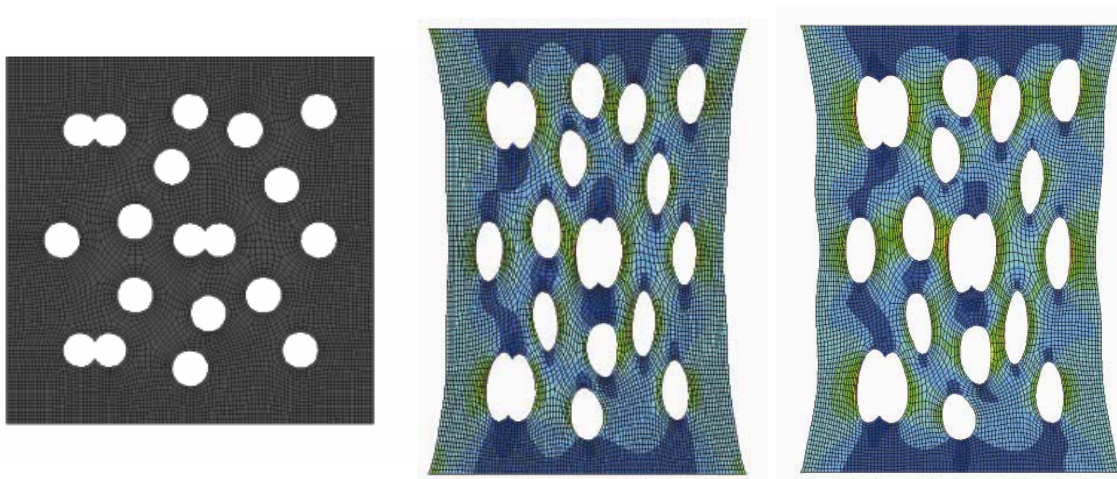


Figure 5.23 Results of stretching the 19-hole mesh (A) with Arruda-Boyce (B) and Marlow (C) hyperelastic models

Table 5.13
Results of stretching the 19-hole mesh with Arruda-Boyce and Marlow hyperelastic models, compared with the experimental results from the 3 μ m PET membrane stretched 21%

Model	Area	Major Axis	Minor Axis	Aspect Ratio
Change (%)				
Marlow	32.8	38.3	-0.7	51.9
Arruda-Boyce	35.1	37.9	0.2	56.1
3 μ m PET 21%	23.3	32.1	-5.1	43.8

The Marlow hyperelastic predicts linear increases in area, major axis, and aspect ratio with strain, but this is not always experimentally observed, although as mentioned in the “Materials Results” chapter, a linear fit is the best for the experimental data. The ability of the simulation to predict a decrease in minor axis is diminished by high porosities. The interaction effect observed in the two-hole studies holds true for the multiple hole studies: The presence of another pore lessens the ability of the minor axis to decrease. This, however, is not observed experimentally. The fact that only uniaxial test data could be obtained may be hindering the model. The minor axis is a reflection of the strain in the direction perpendicular to that of stretching. Without having some prediction of stress in this direction along with uniaxial stress, this model is incomplete.

5.8 REBOUND STUDY

Using the one-hole mesh with actual hyperelastic viscoelastic properties, a simulation was created with a heating, stretching, annealing, cooling, and “letting go” step to most closely mimic experimental steps measure the predicted rebound of the membrane. Rate of stretching did not have a significant effect on the rebound of the sample. Stretching temperature and annealing temperature were also varied, and the results are shown in Table 5.14 and Figure 5.24. Rebound is significantly over predicted as compared to that measured experimentally, but the simulation is capable of predicting seemingly permanent deformations. Annealing temperature has a more significant effect on the amount of rebound than stretching temperature, and the trend is the same as that seen experimentally, meaning that a higher annealing temperature leads to lower rebound. Another simulation was performed with actual elastic viscoelastic properties, which was stretched 40% like all the simulations discussed here, but this sample retained only 4.4% of its original strain, which is significantly less than any of the hyperelastic viscoelastic simulations. This constitutive model is capable of predicting the permanent deformations observed, but not accurately.

Table 5.14
Rebound results for stretching one-hole meshes 40%
at various temperatures and annealing at various temperatures

Stretch Temperature (°C)	Annealing Temperature (°C)	Rebound (%)
150	150	72.7
150	180	64.4
180	180	64.2
120	150	73.0
120	180	64.5
120	165	68.5
165	180	64.3

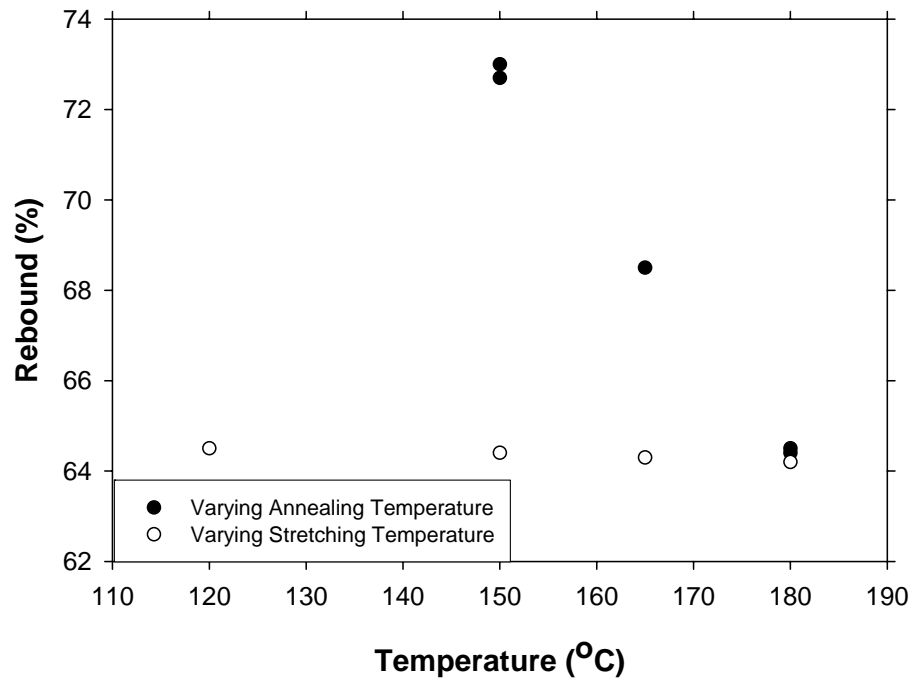


Figure 5.24 Rebound as a function of temperature for the cases of varying only annealing temperature and varying only stretching temperature

5.9 THREE-DIMENSIONAL SIMULATIONS WITH ACTUAL PROPERTIES

A simple 3-dimensional mesh was created to start, but without enough elements, the circular pore at the center was not accurately represented, so this mesh, shown in Figure 5.25, was disregarded. The next mesh was based on the 200-element 2-dimensional mesh used above with one layer of elements, and then the next was the same but with 5 layers of elements. These are shown in Figure 5.26.

These meshed were stretched 40%, and the results are shown in Table 5.15 and Figure 5.27. The one layer mesh over predicts the increase in area and major axis, but the 5 layer gets closer to both experimental and 2D results. The stress distributions in the 3D simulations do not reveal anything new or surprising about the pore deformation over the 2D simulation, but take hours to process, as compared to seconds or minutes with the 2D simulations. The 2D simulations are sufficient for getting the results required for this study.

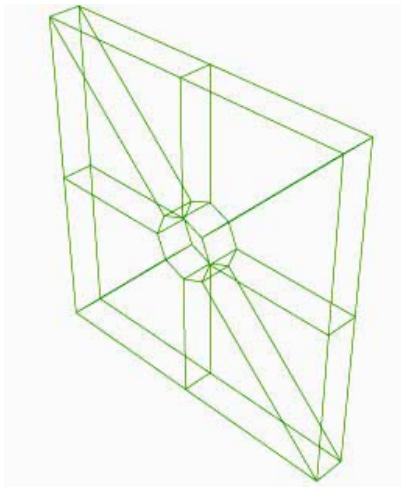


Figure 5.25 8 element 3D mesh

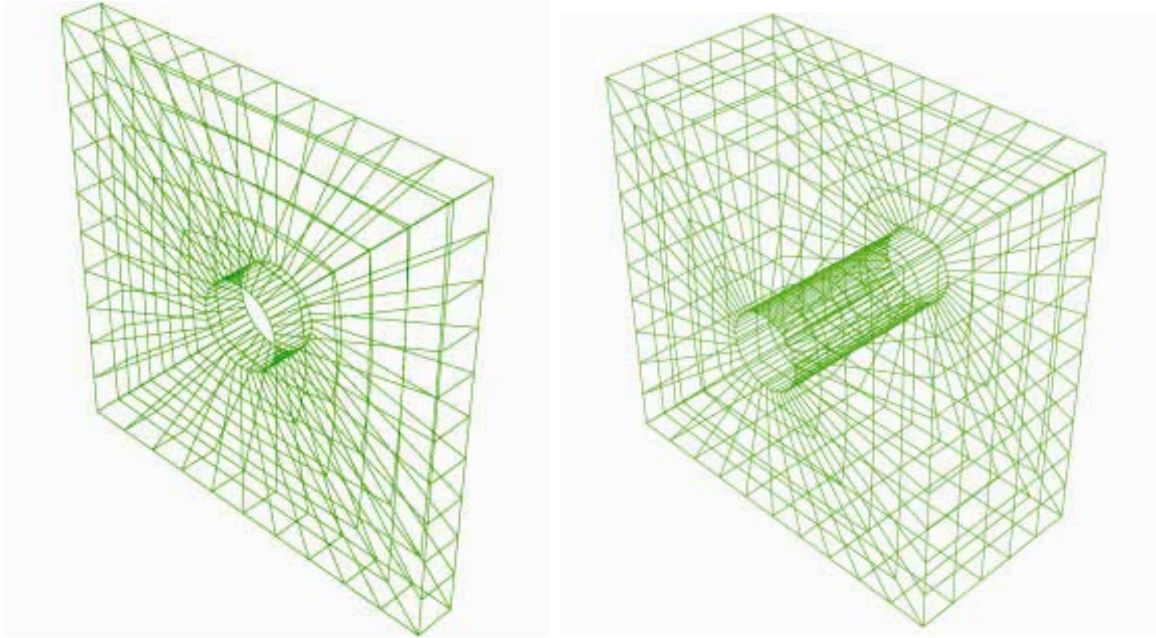


Figure 5.26 3-dimensional meshes with a single pore based on the 200 element 2-dimensional user defined mesh

Table 5.15
Results for stretching 3-dimensional meshes with actual properties

Mesh	Area	Major Axis	Minor Axis	Aspect Ratio
		Change (%)		
1 layer	112.0	143.9	-13.2	181.0
5 layer	62.2	110.0	-22.0	169.2

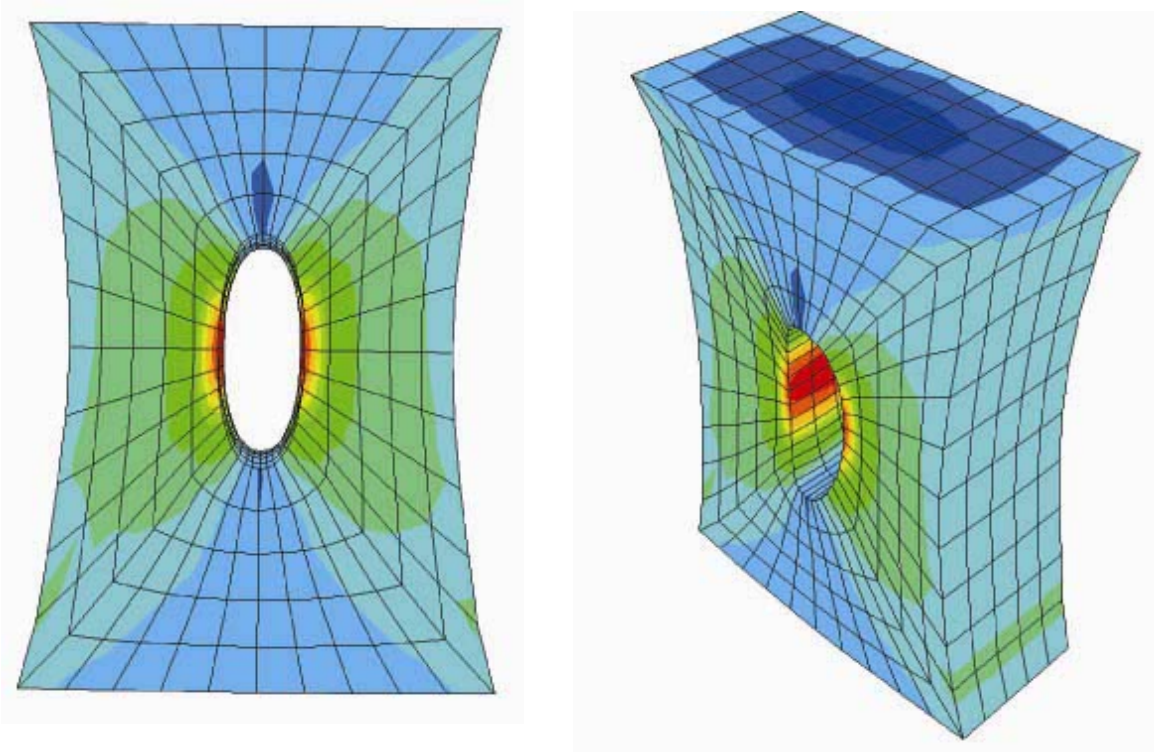


Figure 5.27 Results of stretching 3-dimensional meshes with actual properties

CHAPTER 6: CONCLUSIONS AND RECOMMENDATIONS

6.1 CONCLUSIONS

The purpose of this study was twofold: 1) The first objective was to improve membrane performance, meaning flux and rejection, by uniaxially stretching the membrane and thereby altering its physical characteristics. 2) The second objective was to model the stretching process through finite element simulation such that membrane physical characteristics after stretching can be predicted based on stretching parameters and material properties. To achieve these objectives, several tasks had to be accomplished. Track-etched membranes had to be stretched and characterized to determine the change in physical characteristics, then characterized to determine their performance capabilities in terms of flux and rejections. An appropriate constitutive model had to be chosen and implemented to simulate stretching, and those results characterized for comparison to experimental results to determine the effectiveness of the simulation. All of these tasks were completed successfully.

Membranes were stretched and retained permanent deformations up to 40%. This resulted in increases in pore area, major axis, aspect ratio, and membrane porosity, and decreases in minor axis. The change in minor axis was of much less magnitude than that of other parameters. All parameters increased or decreased linearly with strain and showed little or no dependence on temperature on strain rate. The ability of the membrane to retain its deformed state showed dependence on both of these parameters, but showed the strongest dependence on the temperature to which it was allowed to cool before it was released. Rebound varied from a few percent to up to 44%.

Pure water flux was shown to improve upon stretching for the 0.6 μm PET sample, but the improvement in flux for other samples was more difficult to see. Flux with particulate challenge improved in every case with stretching with both Min-u-sil irregularly shaped particles and microspheres. The increase in flux varied depending on the pore size and the magnitude of stretch being tested. This increase did not correlate with the increase in pore area. Particle rejection was shown to improve in some cases,

but the ability of a membrane to reject more particles did not correlate to the decrease in minor axis.

The constitutive model and method chosen for simulating the stretching process is capable of predicting increases in major axis, area, and aspect ratio, and decreases in minor axis. It is also capable of predicting permanent deformations and pore interactions. The magnitude of the change in parameters like area and aspect ratio did not always correlate well with experimental results, especially for moderate porosity samples. The correlation between the rebound of the simulation and that of the experiment was not good.

6.2 RECOMMENDATIONS

6.2.1 Stretching Membranes

Although track-etched membranes are useful for fundamental studies and small-scale separations, other types of membrane such as phase separation / phase inversion membranes are in wider use. Jason Morehouse has done work with stretching poly(ether sulfone) and poly(vinylidene fluoride) (Morehouse 2006), but there are other membrane materials of interest, including Nylon and polyethylene. Other track-etched membranes are also of interest, such as those made from polypropylene, PVDF, polyimides, and polysulfones. Some production of each of these has been attempted, but limited market or process complexity has kept these material from being widely distributed (Apel 2001).

Of particular interest to the fundamental studies is a new membrane being made at the University of Houston. This membrane is much like a track-etched membrane, but is made using a pattern, so pores are circular and arrayed. These membranes are made using array lithography from polyimide material (Han et al. 2005). Current production is lab-scale only and samples are thin. The most promising possibility for stretching is a 5 μm pore size that is 10 μm thick, comparable to the 10 μm PET membrane that is 13 μm thick which was stretched in this study. Array lithography membranes also bring about the possibility of creating shapes other than circles at the surface of the membrane, such

that pores with aspect ratios much greater than one could be created without the stretching process.

6.2.2 Performance Characterization

Both monodisperse and broad distribution particle challenges were used to characterize the performance of stretched and non-stretched membranes in this research. Recently some surrogate natural organic matter (NOM) was used in the laboratories of Professor Lawler to challenge the 2 μm PET membrane, but the molecular weight available in the lab did not foul the membrane significantly. More appropriate molecular weights are being chosen to test membranes of this and other pore sizes, and other types of NOM are being considered. Oily-water emulsions and protein solutions are also under consideration for performance characterization studies in the laboratories of Professor Freeman. Another, more fundamental idea for characterization would be mixing several monodisperse particles in suspension to use as challenge.

6.2.3 Modeling

Two-dimensional simulations proved to be useful in predicting pore behavior and pore interactions during stretching, but only one configuration of overlapping pores was used in simulation, and no other non-circular pores were modeled. From SEM pictures it is obvious that not all pores are perpendicular to the membrane surface, resulting in pores that are elliptical on the surface before stretching. Some modeling could be done to better approximate the initial state of the membrane, taking into account the initial pore size distribution. Other three-dimensional simulations could also be performed. Thicker samples to better correlate to the smaller pore sizes would be appropriate, and slanted pores would also be a closer approximation to commercial T-E membranes.

The constitutive models used in this study fell short of accurately predicting the permanent deformations achieved by experimental stretching. The hyperelastic data in particular was difficult to fit to experimental data. Recent publications show that hyperelastic viscoelastic models are being used to model thermoforming processes

(Erchiqui et al. 2005). A better fit to the hyperelastic data could be found or developed so that this constitutive model could be used to more effectively model this material.

APPENDIX A: TEMPERATURE EQUILIBRIUM PRELIMINARY EXPERIMENT

In order to determine how long it took for the membrane to reach the desired temperature, a thermocouple was placed on the membrane, and the heating box was closed. The desired temperature was set, in this case 120°C. The temperature of both the plates and the membrane was recorded every 5 minutes for an hour. The results are shown here in Figure A1. Less than 30 minutes after the plates reached the desired temperature, the membrane did the same. Based on this result, this procedure was adopted as standard for all subsequent experiments.

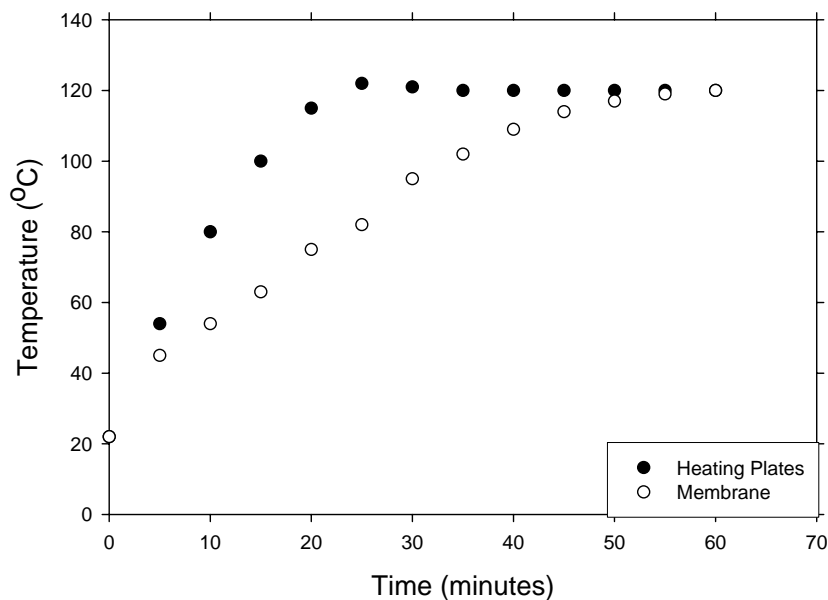


Figure A1: Temperature for heating plates and membrane as sample heats up inside the stretching apparatus.

APPENDIX B: DETERMINATION OF ANNEALING TIME

Annealing time and annealing temperature were two variables that were not chosen for this study, but which had to be standardized in the experimental procedure in order to ensure that they would have no effect on experimental results. It was determined from the literature (reference here) that annealing at or above the stretching temperature was appropriate to avoid rebounding, or returning the membrane to its original configuration. It was also determined that annealing for 10 to 15 minutes was an appropriate approximation for annealing time. These facts from literature were tested in the lab by stretching a sample of PET membrane at approximately 120°C and A) letting it go immediately, B) annealing it at its stretched position at the same temperature for 15 minutes, and C) annealing at a temperature 20°C higher than the stretching temperature. The total strain on the membrane after the experiment was determined by measuring the length of the sample before and after the experiment, and the applied strain was determined by measuring the distance the grips traveled. These experiments were done before the new stepper motor and linear potentiometer had been added to the machine. Both annealing techniques were found to be effective, showing little or no rebound, whereas the experiment in which there was no annealing showed significant rebounding upon release from the grips. It was then decided that all samples would be annealed for 15 minutes at or above the stretching temperature.

APPENDIX C: SUPPLEMENTAL RELAXATION EXPERIMENTS

Relaxation experiments were performed using a mechanical testing machine in a lab in the Aerospace and Engineering Mechanics department run by Dr. K. M. Liechti. These experiments were performed at room temperature using PET Mylar film of 23 μm thickness. The samples were prepared in a similar manner to that described in Section 2.3.2. Samples were cut in thin strips approximately 15 cm in length and 1 cm in width. A horizontal mark was made on the film using a pen or marker, and a magnified video camera was set up to record the movement of this mark as strain was applied to the sample, and force was read as a function of time for a period of approximately 30 to 45 minutes. Digital image analysis software was then used to determine the strain that had been applied, and stress was determined. The readings obtained by the mechanical testing apparatus in Dr. Liechti's laboratory and the results obtained by the T.M. Long stretcher were very similar, as shown in Figure C.1.

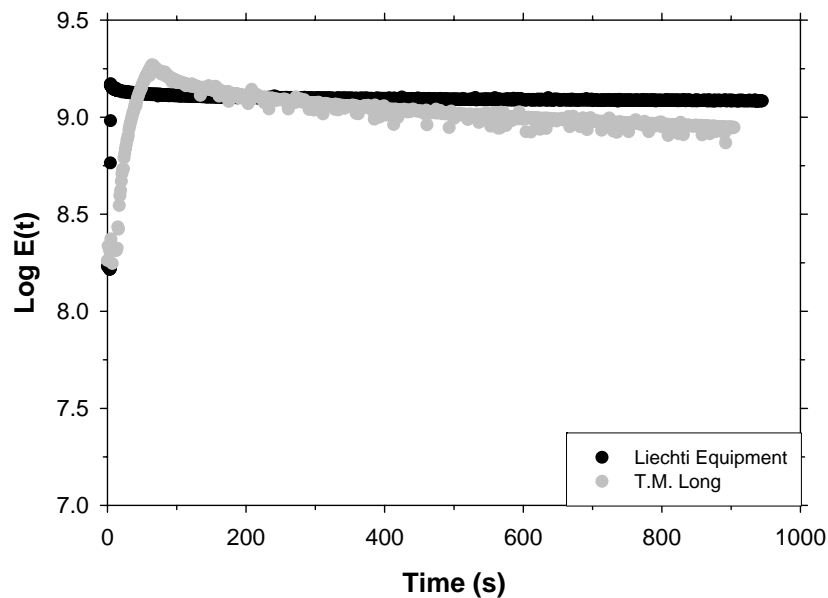


Figure C.1 Relaxation of PET Mylar film on two different testing apparatuses to test the reasonability of results

GLOSSARY

A_m	Area of membrane
A_{pore}	Area of pore
a_T	WLF shift factor
B	Deformation Tensor
C_1	WLF constant in ABAQUS
C_2	WLF constant in ABAQUS
C_1^g	Universal WLF Constant
C_2^g	Universal WLF Constant
D	Aperture size
d_p	Particle size
ε	Strain
ε_o	Instantaneous Strain
E_e	Equilibrium relaxation modulus
E_o	Instantaneous relaxation modulus
$E(t)$	Relaxation modulus as a function of time
F	Deformation gradient
$F(t)$	Force as a function of time
ϕ_{cake}	Volume fraction of particles in the cake
ϕ_b	Volume fraction of particles in the suspension
$G(t)$	Shear relaxation modulus
γ	Constant strain
γ_m	Parameter of the Arruda-Boyce model
h	Membrane thickness
$H(t)$	Heaviside step function
i	Constant current
J	Flux
J_{el}	Elastic volumetric strain
k	Intrinsic permeability
$K(t)$	Bulk relaxation modulus

μ	Viscosity
μ_e	Equilibrium shear modulus
$\mu(t)$	Shear relaxation modulus
η	Creep Compliance
ΔN	Number of particles
r_{pore}	Radius of pore
ΔR_2	Change in resistance
R_{cake}	Resistance of the cake
R_m	Resistance of the membrane
ρ_2	Specific resistivity
σ	Stress
θ	Temperature
θ_o	Reference Temperature
t	Time
t'	Shifted time
T	Temperature
T_r	Reference Temperature
τ	Time constant
U	Strain energy function
ΔU	Voltage pulse height
U_o	Strain energy density
U_D	Deviatoric strain energy
U_V	Volumetric strain energy
V	Volume
V_{cum}	Cumulative volume
ΔV	Particle volume
w	Width
ξ	Tortuosity
x	Location in a material in the deformed state
X	Location in a material in the un-deformed state

REFERENCES

- Allison, S. W. and I. M. Ward 1967. The cold drawing of polyethylene terephthalate. *British Journal of Applied Physics* 18: 1151-1164.
- Alwattari, A. A. and D. R. Lloyd 1991. Microporous membrane formation via thermally-induced phase separation. VI. Effect of diluent morphology and relative crystallization kinetics on polypropylene membrane structure. *J. Membr. Sci.* 64: 55-68.
- Andersson, H. 1977. Analysis of a model for void growth and coalescence ahead of a moving crack tip. *J. Mech. Phys. Solids* 25: 217-233.
- Apel, P. 2001. Track etching technique in membrane technology. *Radiation Measurements* 34: 559-566.
- Beck, R. E. and J. S. Schultz 1972. Hindrance of Solute diffusion within membranes as measured with microporous membranes of known pore geometry. *Biochimica et biophysica acta.* 16: 211-213.
- Bergstrom, J. S., and M. C. Boyce 1998. Constitutive Modeling of the Large Strain Time-Dependent Behavior of Elastomers. *Journal of the Mechanics and Physics of Science* 46(5): 931-954.
- Bierenbaum, H. S., R. B. Isaacson, et al. 1974. Microporous polymeric films. *Industrial Engineering Product Research Development* 13: 2-9.
- Brostow, W., N. A. D'Souza, et al. 1999. Creep and stress relaxation in a longitudinal polymer crystal: Prediction of the temperature shift factor. *Journal of Chemical Physics* 110(19): 9706-9712.
- Budiansky, B., J.W. Hutchinson, S. Slutsky 1982. Void Growth and Collapse in Viscous Solids in. *Mechanics of Solids*. Oxford, Pergamon Press: 13-45.
- Chandavas, C., M. Xanthos, et al. 2001. *Preparation of microporous films from immiscible blends via melt processing and stretching*. USA, New Jersey Institute of Technology.
- Chowdhury, Z. K., A. VanGelder, et al. 2000. *Particle Count Method Development for Concentration Standards and Sample Stabilization*. Denver, CO, AWWA Research Foundation and American Water Works Association.
- Christensen, R. M. 1982. *Theory of Viscoelasticity*. Mineola, New York, Dover Publications.
- Clements, B. E. 1999. Damage Evolution in Viscoelastic Polymers. *AIP Conference Proceedings* 505(1): 527-530.
- Clinnton, P. W. 1997. *Microporous materials of ethylene-vinyl alcohol copolymer and method of making same*. US, 3M.
- Cook, R. D. 1998. *Advanced Mechanics of Materials*. Upper Saddle River, Prentice-Hall Inc.
- Deen, W. M. 1987. Hindered transport of large molecules in liquid-filled pores. *AIChE Journal* 33: 1409-1425.
- Druin, M. L., L. T., et al. 1972. *Novel Open-Celled Microporous Film*. USA, Celanese Corporation.
- Erchiqui, F., A. Gakwaya, et al. 2005. Dynamic finite element analysis of nonlinear isotropic hyperelastic and viscoelastic materials for thermoforming applications. *Polymer Engineering and Science* 45: 125-134.

- Eshelby, J. D. 1957. The determination of the elastic field of an ellipsoidal inclusion, and related problems. *Proceedings of the Royal Society (London)* A241: 376-396.
- Espinoza-Gomez, H. and S. Wai 2001. Development of ultrafiltration membranes from acrylonitrile co-polymers. *Polymer Bulletin* 47(3-4): 297-304.
- Fisher, H. M., D. E. Leone, et al. 1989. *Microporous membranes having increased pore densities and process for making the same*. USA, Hoechst Celanese Corporation.
- Flemming, H. C. and G. Schaule 1988. Biofouling on membranes - a microbiological approach. *Desalination* 70: 95-119.
- Flemming, H. C., G. Schaule, et al. 1993. How do performance parameters respond to initial microfilm formation on separation membranes? *Vom Vasser* 80: 177-186.
- Flemming, H. C., G. Schaule, et al. 1994. Effects and extent of biofilm accumulation in membrane systems. in. *Biofouling and Biocorrosion in Industrial Water Systems*. G. G. Geesey, Z. Lewandowski and H.-C. Flemming. Boca Raton, CRC Press: 63-89.
- Gere, J. M. 2004. *Mechanics of Materials*. Belmont, Brooks/Cole.
- Glandt, E. D. 1980. Density Distribution of Hard-Spherical Molecules Inside Small Pores of Various Shapes. *J. Colloid Interface Sci.* 77(2): 512-524.
- Glandt, E. D. 1981. Noncircular pores in model membranes: a calculation of the effect of pore geometry on the partition of a solution. *J. Membr. Sci.* 8: 331-336.
- Gurson, A. L. 1977. Continuum theory of ductile rupture by void nucleation and growth : Part 1. Yield criteria and flow rules for porous media. *Journal of Engineering Materials and Technology, Transactions of the ASME* 99: 2-15.
- Han, K., W. Xu, et al. 2005. Fabrication and characterization of polymeric microfiltration membranes using aperture array lithography. *Proceedings of AWWA National Meeting (Phoenix, AZ)*.
- Hashin, Z. 1965. Viscoelastic Behavior of Heterogeneous Media. *J. Appl. Mechanics* 32(3): 630-636.
- Hermia, J. 1982. Constant pressure blocking filtration laws - application to power-law non-Newtonian fluids. *Trans. Inst. Chem. Eng* 60: 183-187.
- Hibbitt, K., and Sorensen 1998. ABAQUS Theory Manual in: 4.6.1-1 - 4.7.2-10.
- Ho, C.-C. and A. Zydney 1999. Effect of membrane morphology on the initial rate of protein fouling during microfiltration. *J. Membr. Sci.* 155: 261-275.
- Ho, C.-C. and A. Zydney 2000. A Combined Pore Blockage and Cake Filtration Model for Protein Fouling during Microfiltration. *J. Colloid Interface Sci.* 232: 389-399.
- Ho, W. S. W. and K. K. Sirkar, Eds. 1992. *Membrane Handbook*. New York, van Nostrand Reinhold.
- Hoeve, C. A. J. and M. K. O'Brien 1963. Specific diluent effects on polymer chain dimensions. *Journal of Polymer Science; Part A* 1: 1947-1954.
- Hong, S. K. and M. Elimelech 1997. Chemical and Physical Aspects of Natural Organic Matter (NOM) Fouling of Nanofiltration. *J. Membr. Sci.* 132: 159-181.
- Hwang, K.-J., Y.-S. Wu, et al. 1997. Effect of the size distribution of spheroidal particles on the surface structure of a filter cake. *Powder Technology* 91(2): 105-113.
- Jacoby, P., C. W. Bauer, et al. 1992. *Oriented polymeric microporous films*. USA, Amoco Corporation.
- Jolliffe, C. N. 1995. *Method of making biaxially oriented thermoplastic films*. US, E. I. Du Pont de Nemours and Company.

- Kesting, R. E. 1985. Synthetic polymeric membranes: a structural perspective in. New York, John Wiley & Sons: 287-310.
- Kim, K. J. and P. V. Stevens 1997. Hydraulic and surface characteristics of membranes with parallel cylindrical pores. *J. Membr. Sci.* 123(2): 303-314.
- Kim, K.-J., P. V. Stevens, et al. 1994. Porosity dependence of pore entry shape in track-etched membranes by image analysis. *J. Membr. Sci.* 93(1): 79-90.
- Kim, S. S., G. B. A. Lim, et al. 1991. Microporous membrane formation via thermally induced phase separation. V. Effect of diluent mobility and crystallization on the structure of isotactic polypropylene membranes. *J. Membr. Sci.* 64(41-53).
- Kim, S. S. and D. R. Lloyd 1991. Microporous membrane formation via thermally-induced phase separation. III. Effect of thermodynamic interactions on the structure of isotactic polypropylene membranes. *Journal of Membrane Science* 64: 13-29.
- Kinzer, K. E. 1989. *Oriented microporous films*. US, 3M.
- Kinzer, K. E. 1993. *Method for preparing oriented microporous film*. US, 3M.
- Knoell, T., J. Safarik, T. Cormack, R. Riley, S.W. Lin, H. Ridgeway 1999. Biofouling potentials of microporous polysulfone membranes containing a sulfonated polyether-ethersulfone/polysulfone block copolymer: correlation of membrane surface properties with bacterial attachment. *Journal of Membrane Science* 157: 117-138.
- Lawler, D. F. and J. Kweon 2003. *Integrated water treatment: softening and ultrafiltration*. Denver, Awwa: 172.
- Leslie, G. L., R. P. Schneider, et al. 1993. Fouling of a microfiltration membrane by two gram-negative bacteria. *Colloids and Surfaces A* 73: 165-178.
- Li, J. a. G. J. W. 1995. Void growth in viscoelastic polymeric materials. *Mechanics of Plastics and Plastic Composites, ASME* 1995 68: 409-421.
- Li, J. a. G. J. W. 1998. A unified approach from elasticity to viscoelasticity to viscoplasticity of particle reinforced solids. *International Journal of Plasticity* 14(1-3): 293-208.
- Liechti, K. M. and W. Adamjee 1992. Mixed-mode cathodic delamination of rubber from steel. *Journal of Adhesion* 40: 27-45.
- Lim, G. B. A., S. S. Kim, et al. 1991. Microporous membrane formation via thermally-induced phase separation. IV. Effect os isotactic polypropylene crystallization kinetics on membrane structure. *J. Membr. Sci.* 64(31-40).
- Lloyd, D. R., S. S. Kim, et al. 1991. Microporous membrane formation via thermally-induced phase separation. II. Liquid-liquid phase separation. *J. Membr. Sci.* 64: 1-11.
- Lloyd, D. R., K. E. Kinzer, et al. 1990. Microporous membrane formation via thermally induced phase separation I. Solid-liquid phase separation. *J. Membr. Sci.* 52: 239-261.
- Lueck, H. B. 1982. *Kinetik und Mechanismus der Bildung and Qetzung von Teilchenspuren in Polyethyleneterephthalat*. Germany.
- McClintock, F. A. 1968. A Criterion for Ductile Fracture by the Growth of Holes. *J. Appl. Mechanics*: 363-371.
- McCray, S. B., D. T. Friesen, et al. 2001. *Ethylene-vinyl alcohol hollow fiber membranes*. USA, Ebara Corporation.

- McCrum, N. G., C.P. Buckley, C.B. Bucknall 1997. *Principles of Polymer Engineering*. Oxford, Oxford University Press.
- Meares, P. and K. R. Page 1972. Rapid force-flux transitions in highly porous membranes. *Philosophical transactions of the Royal Society of London. Series A, Mathematical and physical sciences* 272: 1-47.
- Mohan, R. and F. W. Brust 2000. On Void Growth in Elastic-Nonlinear Viscous Solids Under Creep and cyclic creep conditions. *Journal of Engineering Materials and Technology* 122(July): 283-293.
- Morehouse, J. 2006. *The effect of uni-axial stretching on microporous phase-separation membrane structure and performance*. Chemical Engineering. Austin, TX, University of Texas at Austin.
- Mrozinski, J. S. 1988. *Microporous materials incorporating a nucleating agent and methods for making same*. US, 3M.
- Mrozinski, J. S. 1989. *Multi-layer laminates of microporous film*. US, 3M.
- Mrozinski, J. S. 1993. *Method for preparing microporous polyolefin shaped articles*. US.
- Murayama, T., J. H. Dumbleton, et al. 1968. Viscoelasticity of Oriented Poly(ethylene Terephthalate). *Journal of Polymer Science: Part A-2* 6: 787-793.
- Nash, G. B. 1990. Filterability of blood cell: methods and clinical applications. *Clinical hemorheology and microcirculation* 10: 353-362.
- Needleman, A. 1972. Void growth in an elastic-plastic medium. *Transaction of Journal of Applied Mechanics*: 964-970.
- Pasternak, C. A., G. M. Adler, et al. 1995. Model pores for biological membranes: the properties of track-etched membranes. *Nuclear Instruments and Methods in Physics Research: Section B* 105(1-4): 332-334.
- Quinn, J. A., J. L. Anderson, W. S. Ho, and W. J. Petzny 1972. Model Pores of Molecular Dimensions: The Preparation and Characterization of Track-Etched Membranes. *Biophysical Journal* 12: 990-1007.
- Rice, J. R., D.M. Tracey 1969. On the ductile enlargement of voids in triaxial stress fields. *Journal of the Mechanics and Physics of Science* 17: 201-217.
- Ridgway, H. F. and H. C. Flemming 1996. Membrane biofouling in. *Water Treatment Membrane Processes*. J. Mallevialle, P. E. Odendaal and M. R. Wiesner. New York, McGraw-Hill: 6.1.
- Ridgway, H. F. and J. Safarik 1991. Biofouling on reverse osmosis membranes. in. *Biofouling and Biocorrosion in Industrial Water Systems*. H.-C. Flemming and G. G. Geesey. Berlin, Springer: 81-111.
- Sall, J., A. Lehman, et al. 2001. *JMP Start Statistics: A Guide to Statistics and Data Analysis Using JMP and JMP IN Software*. Pacific Grove, CA, Duxbury.
- Sarada, T. and L. C. Sawyer 1983. Three dimensional structure of Celgard microporous membranes. *J. Membr. Sci.* 15: 97-113.
- Shimko, L. 2005. *Impact of Uni-axial Stretching on Microfiltration Membrane Performance*. Civil, Architectural, and Environmental Engineering. Austin, TX, University of Texas at Austin: 79.
- Shipman, G. H. 1985. *Microporous sheet material method of making and articles made therewith*. US, 3M.
- Smit, R. J. M., W.A.M. Brekelmans, H.E.H. Meijer 2000. Predictive Modelling of the properties and toughness of polymeric materials: Part III: Macrostructural

- Deformation of rubber modified polymers. *Journal of Materials Science* 35: 2881-2892.
- Steenbrink, A. C., E. Van Der Giessen, P.D. Wu 1998. Studies of the Growth of voids in amorphous glassy polymers. *Journal of Materials Science* 33(12): 3163-3175.
- Sweeney, J., P. Caton-Rose, P.D. Coates 2001. The modelling of large deformations of pre-oriented polyethylene. *Polymer* 43: 899-907.
- Takita, K., K. Kono, et al. 1991. *Microporous polyolefin membrane and method of producing same*. US, Tonen Corporation.
- Takita, K., K. Kono, et al. 1991. *The preparation method for microporous polyolefin membrane*. Japan, Tonen.
- Tracey 1971. Strain-Hardening and Interaction Effects on the Growth of Voids in Ductile Fracture. *Engineering Fracture Mechanics* 3: 301-315.
- Tsou, D. 2003. *Personal Communication*. L. Worrel.
- Tvergaard, V. 1981. Influence of voids on shear band instabilities under plane strain conditions. *International Journal of Fracture* 17(4): 389-407.
- Tvergaard, V. 1982. On localization in ductile materials containing spherical voids. *International Journal of Fracture* 18(4): 237-252.
- Van Gelder, A. M., Z. K. Chowdhury, et al. 1999. Conscientious Particle Counting. *Journal, American Water Works Association* 91(12): 64-76.
- van Hinsbergh, V. W. M., M. A. Scheffer, et al. 1990. Macro- and microvascular endothelial cells from human tissues in. *Cell Culture Techniques in Heart and Vessel Research*. H. M. Piper. Berlin, Germany, Springer-Verlag: 179-204.
- Vigny, M., A. Aubert, J.M. Hiver, M. Aboulfaraj, C. G'Sell 1999. Constitutive Viscoplastic Behavior of Amorphous PET During Plant-Strain Tensile Stretching. *Polymer Engineering and Science* 39(12): 2366-2376.
- Vrijenhoek, E., S. Hong, et al. 2001. Influence of membrane surface properties on initial rate of colloidal fouling of reverse osmosis and nanofiltration membranes. *J. Membr. Sci.* 188: 115-128.
- Wang, Y. M., G.J. Weng 1993. Self-Similar and transient void growth in viscoelastic media at low concentrations. *International Journal of Fracture* 61: 1-16.
- Wiesner, M. R. and P. Aptel 1996. Mass Transport and Permeate Flux and Fouling in Pressure-Driven Processes In Water Treatment Membrane Processes. in. *Water Treatment Membrane Processes*. J. Mallevalle, P. E. Odendaal and M. R. Weisner. New York, NY, McGraw-Hill: 4.1-4.30.
- Williams, M. L., R. F. Landel, et al. 1955. The temperature dependence of relaxation mechanisms in amorphous polymers and other glass-forming liquids. *Journal of the American Chemical Society* 77: 3701-07.
- Worrel, L. S., J. A. Morehouse, D. R. Lloyd, B. D. Freeman, D. F. Lawler 2005. Track-Etched Membrane Modification via Stretching. *Journal of Membrane Science*. In Preparation.
- Wu, J. D., and Kenneth M. Liechti 2000. Multiaxial and Time Dependent Behavior of a Filled Rubber. *Mechanics of Time-Dependent Materials*(4): 293-331.
- Yoshida, M., K. Tsunashima, et al. 1999. *Biaxially oriented polyester film and process for production thereof*. Japan, Toray Industries, Inc.

Yukio, S. and S. Fumiyuki 2001. *Biaxial oriented polyester film and method of manufacturing same, photographic substrate, and photographic light-sensitive material*. Japan, Fuji Photo Film Co., Ltd.

VITA

Leah Salathe Worrel was born in Gulfport, MS on July 16, 1979 to Steve and Connie Worrel. She graduated with special honors from Hattiesburg High School in 1997. Leah attended the University of Mississippi from 1997 until May 2001, at which time she graduated Summa Cum Laude with a B.S. in Chemical Engineering. Leah began her graduate studies at the University of Texas at Austin in August 2001. Upon graduation she will begin work for Sandia National Laboratory in Albuquerque, NM.

Permanent Address: 915 Adeline Street, Hattiesburg, MS 39401

This dissertation was typed by the author.